NUCLEAR SPIN POLARIZATION OF ^{12}B PRODUCED IN ^{14}N INDUCED REACTIONS

KAZUHIRO TANAKA

DISSERTATION IN PHYSICS

GRADUATE SCHOOL OF SCIENCE

THE OSAKA UNIVERSITY

TOYONAKA, OSAKA

560 JAPAN

1983

Abstract

Nuclear spin polarization of projectile-like-fragments ^{12}B produced in the (^{14}N,^{12}B) reactions on ^{232}Th, ^{100}Mo, ^{nat}Cu, ^{nat}Fe, ^{45}Sc and ^{27}Al was measured as functions of reaction Q-value and scattering angle with incident energies of about 120 MeV and 200 MeV. The principles employed were asymmetric β decay for polarization determination, NMR detection for rejection of instrumental asymmetry and range-energy relation for determination of kinetic energy of ^{12}B.

Systematic dependence of ^{12}B polarization on the reaction Q-value was found for heavy targets from ^{232}Th to ^{nat}Fe. Polarization was large and negative in the region of small kinetic energy loss, becoming positive or zero with increase of kinetic energy loss and became again negative in the region of large kinetic energy loss. The mechanism relevant in the region of small energy loss was the direct transfer of two protons from the projectile to the target, while in the other region of energy loss the dominant mechanism was the frictional process at the touching surface of both nuclei.

Another trend of polarization was found for light targets in a region of small energy loss. Positive polarization was observed in the region of small energy loss for ^{27}Al target. This polarization gradually decreased with increase of mass number of target, i.e., the polarization in this region was nearly equal to zero for ^{45}Sc target. This fact indicates the two reaction mechanisms, the direct transfer and the frictional process, are competing for

the predominance over the polarization. The frictional process tends to decrease relative to the direct process in this region with increase of the mass number of target. This change of the dominant mechanism is understood in terms of the interaction time and the energy loss in the frictional process. These quantities are smaller for lighter target than for heavier target, resulting in a positive polarization in the region of small energy loss rather than the negative polarization due to the direct process.

The friction constant deduced from the present experimental data within the framework of frictional model was (2.4 $\pm$ 0.5) x 10^{-22} MeV·s/fm^2. This value agrees with what was obtained from the recent study on the reaction Xe + Bi.

CONTENTS

Abstract ii

List of tables vii

List of figures vii

Chapter 1 Introduction 1

Chapter 2 Heavy-ion collision and polarization of reaction products 5

2-1 General aspects and classification of heavy-ion collisions 6

2-2 Macroscopic frictional process of heavy-ion collisions 14

2-3 Microscopic treatments of heavy-ion collisions 25

Chapter 3 Experimental methods 32

3-1 Basis of the polarization measurement ...35

a Production and implantation of ^{12}B 35

b Hyperfine interactions of implanted ^{12}B and preservation of the polarization of ^{12}B 40

c Determination of the polarization 43

d Spin control 49

e Polarization brought in γ-ray cascade and particle decay 54

3-2 Details of experiment 57

a Reaction chamber and production of ^{12}B 57

b β-ray detection 62

c NMR 65

d Timing control 70

3-3 Check experiment by use of the (d,p) reaction 73

3-4 Time and energy spectra of β rays 78

3-4 Summary of the polarization measurement 81

Chapter 4 Results and discussion 82

4-1 Experimental results 83

a Target mass dependence 86

b Scattering angle dependence 92

c Incident energy dependence 97

d Summary of the experimental results 100

4-2 Discussion 106

a Analysis by use of frictional model 106

b Coexistence of the different reaction mechanisms 130

c Comparison with other experimental results 133

Chapter 5 Conclusion 136

Chapter 6 Proposals for continuing research 138

Acknowledgement 142

Appendix

A-1 Introduction to Quasi-Linear Response Theory (QLRT) Apx-1

A-2 Modification of QLRT for heavy-ion reactions with light projectiles Apx-9

References

List of tables

Table 1 Estimated cross section of ^{13}B. 36

Table 2 Reduction rate of ^{12}B polarization by a γ ray cascade. 56

Table 3 Conditions of the check experiment. 74

Table 4 Summary of the experimental conditions, targets, scattering angles and incident energies. 85

Table 5 Q-values of the first zero crossing and the second zero crossing 101

Table 6 Theoretical value of matching Q-value of direct two proton transfer. 103

List of figures

Fig. 1 Formation and decay of di-nuclear system. 10

Fig. 2 Energy spectrum of projectile-like-fragments produced in the reaction $^{232}Th(^{40}Ar,K)$. 11

Fig. 3 Classification of a heavy-ion reaction mechanism according to the quantum number of the incident orbital angular momentum, $l\hbar$ 13

Fig. 4 Deflection of a projectile nucleus as a function of the incident orbital angular momentum. 15

Fig. 5 Contour plot of double differential cross section (Wilczynski plot) of K isotopes

produced for the reaction $^{232}Th(^{40}Ar,K)$. 16

Fig. 6 A schematic illustration of a Wilczynski plot and its interpretation in the deflection process of reaction trajectories. 16

Fig. 7 Calculated mean orbit in the contour plane superimposed on the experimental data. 18

Fig. 8 Expected spin polarization and energy spectrum of projectile-like-fragment produced in various orbits of heavy-ion reactions within the framework of the frictional model. 18

Fig. 9-(a) The atomic number distribution of projectile-like-fragments produced in Bi+Xe reaction. 21

Fig. 9-(b) The variance of the atomic number distribution of projectile-like-fragments produced in Bi+Xe reaction. 21

Fig.10 Isotope production cross section as a function of Q_{gg}. 24

Fig.11 The spin polarization of ^{12}B produced in the reaction $^{100}Mo(^{14}N,^{12}B)$ at an incident energy of 90 MeV. 26

Fig.12 Schematic illustration of the direct cluster transfer process under the kinematical matching model proposed by Brink. 27

Fig.13 Experimental data of circular-polarization in the inelastic heavy-ion reaction $^{58}Ni(^{16}O,^{16}O')$ and compared with the result of

a calculation by use of the three step DWBA developed by Tamura et al. 31

Fig.14 Schematic illustration of the polarization measurement system. 34

Fig.15 Range of ^{12}B in various materials as a function of kinetic energy. 37

Fig.16 An example of range-energy method employed for the kinetic energy determination of ^{12}B. 39

Fig.17 Equilibrated charge states distribution of boron-ion indicated as a function of its velocity. 41

Fig.18 Decay scheme of ^{12}B. 45

Fig.19 Arrangement of counters for the β ray measurement. 46

Fig.20 Schematic illustration of the relation of H_1, H_o, H_o' and H_{eff}. 51

Fig.21 Sinusoidal modulation of the amplitude and the frequency of H_1 as a function of time. 53

Fig.22 Level scheme of ^{12}B. 56

Fig.23 Reaction chamber used for the present study. 58

Fig.24 A pair of rf coils mounted outside the stopper chamber. 60

Fig.25 The beam lines of course-D and course-K at RCNP. 61

Fig.26 Electronics circuit for the β ray measurement. 63

Fig.27 Circuit of rf amplifier with 400W output. 66

Fig.28 Synthesizing modulated rf in both amplitude and frequency for AFP. 67

Fig.29 Block diagram of rf control system. 69

Fig.30 The time flow chart of the experiment. 71

Fig.31 Parallel 4 bit patterns for controlling the measurement system. 72

Fig.32-(a) β ray asymmetry as a function of strength of H_0. 76

Fig.32-(b) β ray asymmetry as a function of strength of H_1. 76

Fig.32-(c) β ray asymmetry as a function of the frequency of H_1. 77

Fig.33 Typical energy spectrum and time spectrum of β rays. 79

Fig.34 χ^2 distribution of a two component fit of the time spectrum of the β rays indicated as a function of half life of the β rays. 80

Fig.35 Experimental results of our previous study. Spin polarization of ^{12}B produced in $^{100}Mo(^{14}N,^{12}B)$ at incident energies of 90, 120 and 200 MeV. 84

Fig.36 Experimental results of ^{12}B polarization and energy spectrum measured near the grazing angle for various targets. 87

Fig.37 Diagram indicating the first and the second zero crossings of the polarization. 88

Fig.38-(a-b) Superposed illustration of the

experimental results measured near the grazing angle for various targets. 90

Fig.39 The polarization in the region of small energy loss plotted as a function of the mass number of target. 91

Fig.40-(a-g) Experimental results of ^{12}B polarization and energy spectrum measured on various scattering angles. 93

Fig.41-(a-d) Experimental polarization at various scattering angles. 95

Fig.42-(a-c) Experimental results of ^{12}B polarization and energy spectrum measured at an incident energy of 200 MeV. 98

Fig.43 Experimental results for various targets at an incident energy of 200MeV. 99

Fig.44 Q-values of the second zero crossing as a function of A, the mass number of target. 107

Fig.45 Schematic illustration of a frictional scattering process used to reproduce the change of the second zero crossing with A. 110

Fig.46 Q-values of the second zero crossing plotted as a function of A, the mass number of target and a calculation by use of a frictional model of heavy-ion reaction. 112

Fig.47 Schematic illustration of a frictional scattering process used for the calculation of the friction constant. 114

Fig.48 Q-values of the second zero crossing and of the Coulomb energy at the final state of the collision. 116

Fig.49-a Experimental results of the friction constant. The values used for E_{loss} are $-(Q(Vcf)+Q(szc))/2$. 118

Fig.49-b Experimental results of the friction constant. The values used for E_{loss} are $-Q(szc)$. 118

Fig.49-c Experimental results of the friction constant. The values used for E_{loss} are -Q for the largest negative polarization. 119

Fig.50 A comparison of an ^{14}N induced reaction to a ^{132}Xe induced reaction with respect to the overlapping area of di-nuclear system. 121

Fig.51 Comparison of experimental results with the QLRT calculation. 123

Fig.52 Calculation by use of QLRT.

-(a) Calculated Q-values of the second zero crossing as a function of A. 124

-(b-p) The spin polarization and the energy spectrum of ^{12}B as a function of the reaction Q-value. 125

Fig.53 Experimental Q-values of the first zero crossing as a function of the scattering angle for ^{100}Mo and a curve calculated under the assumption of coexistence of frictional and

direct processes. 132

Fig.54 Experimental results of circular-polarization of γ rays emitted from the projectile-like and the target-like fragments in heavy-ion reactions. 134

Fig.55 Schematic illustration of heavy-ion collision at relativistic energy. 139

CHAPTER 1

Introduction

The system consisting of two colliding nuclei in heavy-ion reaction usually sustains a large amount of orbital angular momentum of relative motion. Part of this angular momentum can be transformed into the intrinsic spins of the reaction products. Gamma-ray multiplicity and particle and γ-ray anisotropy are good measures of the angular momenta of nuclear states which decay by successive emission of such radiations. The experimental results on multiplicity (Gl 77) and anisotropy (Dy 77, Bi77) indicate the existence of large spin angular momenta in product nuclei of heavy-ion reactions and transferred angular momentum agrees with the prediction of the classical model of heavy-ion collision (Is 76). We can then raise questions how the orbital angular momentum is transformed into the intrinsic one or what the features of the reactions are, when a transfer of large angular momentum concerns. These fundamental questions have to be answered for the full understanding of heavy-ion reactions.

The direction of transformed angular momentum is important information for understanding the angular momentum transfer process. The spin polarization of reaction products is an unambiguous reference to the direction of transfer but difficult to determine by the measurement of the multiplicity and the anisotropy, which can indicate only the spin and the

spin alignment of reaction products. It is thus indispensable to measure the spin polarization by other methods in order to understand the heavy-ion reaction mechanism including the angular momentum transfer.

The spin polarization of reaction products is then useful in verifying the models of heavy-ion reactions. As an example, let us consider the macroscopic frictional model. This model has been first proposed to explain the large kinetic energy dissipation observed in the heavy-ion collisions. In the model the projectile is assumed to move along a classical orbit under the influence of repulsive Coulomb and attractive inter-nuclear forces. The orbit of the incident particle is deflected forward from the Coulomb orbit by the attractive inter-nuclear forces and the kinetic energy of relative motion is dissipated into the internal nuclear excitation by the frictional forces, which operates at the overlapping area of both projectile and target nuclei (Be 73, Bo 74). The angular momentum transfer is caused by the tangential component of the frictional forces. The reaction products are polarized perpendicular to the reaction plane. The sign of the polarization depends on the sign of the deflection angle.

In our previous work the nuclear spin polarization of ^{12}B produced in the reaction $^{100}Mo(^{14}N,^{12}B)$ was measured as a function of reaction Q-value (Su 77, Ta 78). The polarization of ^{12}B qualitatively agreed with the prediction from the frictional model in a wide range of kinetic energy loss, while the polarization observed in the region of small energy loss was not understood in the framework of the frictional model but was successfully interpreted in terms of the direct transfer of two protons from the projectile to the target (Su 77, Is 78). The importance of the direct process in the heavy-ion reaction was first indicated by the polarization of the reaction product. Thus polarization phenomena can be used as a powerful

probe to disclose heavy-ion reaction mechanisms involving angular momentum transfer.

The measurement of polarization is not an easy experiment. Recent developments of experimental technique enable us to study the polarization phenomena in the heavy-ion reaction process. In fact only two methods were applied in measuring polarization of reaction products in heavy-ion reactions: One is to utilize asymmetric β decay of the product β emitter (Su 77); The other is to measure the circular polarization of the γ-rays emitted from the excited levels of the product nuclei (Tr 77). The analyzing power in the former method can be as large as 100 %. The analyzing power in the latter method is up to 2 %. Polarization of both projectile-like and target-like fragments was however successfully observed by use of circular polarization (Tr 80). In the present study, a β ray detection method was applied on reaction product ^{12}B by taking advantage of the large analyzing power, high β-decay maximum energy $E_{\beta max}$ = 13.37 MeV and short β-decay half life $T_{1/2}$ = 20.3 ms. Its application was facilitated thanks to the study of the hyperfine interactions of ^{12}B during the recent twenty years by the Van de Graff group at Osaka university. The technique for the preservation of the polarization of ^{12}B and control of its nuclear spin by use of NMR was well worked out.

The aim of the present study was to find a systematic dependence of the polarization on various parameters of heavy-ion reactions and to clarify the heavy-ion reaction mechanisms through the polarization. Typical aspects of heavy-ion collisions are described in Chap. 2. The polarization phenomena of the reaction products are described in this chapter within the framework of the frictional model and direct nucleon transfer. The basis and details of the techniques used in the measurements are given in Chap. 3. Experimental

results on polarization as a function of reaction Q-value, target mass number A, scattering angle and incident energy are given in Chap. 4. Analysis within the framework of the frictional model, i.e., a trial to extract the averaged friction constant, is described also in this chapter and the result is compared with those obtained in a recent study of the Xe + Bi reaction. A summary is given in Chap. 5. An application of the technique developed in the present study to relativistic heavy-ion reactions is proposed in Chap. 6.

CHAPTER 2

Heavy-ion collision and polarization of reaction products

2-1 General aspects and classification of heavy-ion collisions

2-2 Macroscopic frictional process of heavy-ion collisions

2-3 Microscopic treatments of heavy-ion collisions

2-1 General aspects and classification of heavy-ion collisions

Before describing the typical aspects of heavy-ion collisions, it seems worthwhile to discuss the basis of the treatment of collision processes.

The de-Broglie wavelength associated with the relative motion between colliding nuclei is small in heavy-ion reactions, because of the large mass of the projectile and the target. One can then apply classical concepts for a quantitative discussion of the collision process, i.e., a classical trajectory can be used for describing the phenomena which occur during the collision. Let us compare the wavelength of relative motion to the interaction length of the collision process in order to clarify the applicability of the classical concepts. The de-Broglie wavelength λ is written as

$$\frac{\lambda}{2\pi} \equiv \frac{\hbar}{p} = \frac{\hbar}{\sqrt{2\mu(E_{cm}-V_C)}} \quad , \tag{2-1}$$

here μ is the reduced mass, E_{cm} is the center-of-mass energy and V_C is the Coulomb energy between two colliding nuclei. The interaction length in heavy ion collision can be taken typically about 1 fm, over which the inter-nuclear potential changes drastically. The condition that the wavelength is sufficiently shorter than the interaction length is written as

$$20.8 \cdot \frac{(A_1+A_2)}{A_1 \cdot A_2 (E_{cm}-V_c)} < 1 \quad , \tag{2-2}$$

here A_1 and A_2 are the mass numbers of the projectile and the target nuclei, respectively, and E_{cm} and V_C are taken in units of MeV. The reduced mass number $A_1 \cdot A_2/(A_1+A_2)$ varies typically from 10 to 100 in heavy ion collisions. The condition is satisfied, if the center-of-mass energy is

several tens of MeV higher than the Coulomb energy. Such an energy is several MeV/u in the laboratory system.

The de-Broglie wavelength of an individual nucleon in a nuclei also gives a limit to the highest incident energy at which a classical treatment is a good approximation. If the de-Broglie wavelength of individual nucleon is the same order as the size of a nucleon, the collision process must be treated as the superposition of nucleon-nucleon collisions. This is at the energy region of about several hundred MeV/u (He 72). Meson degrees of freedom begin to play an important role in the collision process at an incident energy of several tens of MeV/u and classical concepts may not be applied without modifications. An upper limit of incident energy at which a classical treatment is valid may be about 20 MeV/u (Ge 78).

We focus our discussion on heavy-ion collision with the incident energy from several MeV/u to 20 MeV/u. Typical characteristics of the heavy-ion collision in this energy region are as follows:

(1) Classical concepts are good approximations for a description of the collision process.

(2) The Coulomb interaction between the target and the projectile nuclei is strong and the Coulomb orbit can be considered a zero-th-order approximation for the reaction trajectory.

(3) The orbital angular momentum sustained by the collision system is large and the centrifugal potential plays an important role. The collision process changes with the value of the distance of the closest approach, which may be larger or smaller than the sum of radii of the two nuclei. One can classify the collision process in this energy region according to the distance between the center of the target and the projectile nuclei, d,

(1) Distant collision for $d > R_1+R_2$,

(2) Grazing collision for $d = R_1+R_2$,

(3) Close collision for $d < R_1+R_2$,

where R_1 and R_2 are radii of the target and the projectile nuclei, respectively.

In the distant collision (1), Coulomb excitation and Coulomb scattering occur. No nucleons are exchanged or transferred. In the grazing collision (2), the nuclear surfaces of interacting nuclei are slightly overlapped and a few nucleons are exchanged or transferred almost directly. The velocity of reaction products is essentially the same as that of the incident ion, which proceeds approximately along the Coulomb orbit. The scattering angle to which the collision process occurs is defined as θ_{gr}, the grazing angle. One can calculate θ_{gr} by using the atomic number of the projectile Z_1 and the target Z_2 as,

$$\theta_{gr} = 2\sin^{-1}\left(\frac{D}{2R-D}\right), \qquad (2\text{-}3)$$

where $D = Z_1 \cdot Z_2\, e^2 / E_{cm}$ and $R = R_1 + R_2$. In the close collision (3), the interacting nuclei overlap deeply and many nucleons participate in the collision. A large amount of kinetic energy of relative motion is dissipated into internal excitation of the colliding nuclei. The orbit of the incident ion deviates considerably from the Coulomb orbit. When the impact parameter becomes small the projectile and the target nuclei fuse together.

Such a classification as described above has already been discussed in 1961 by Kaufmann and Wolfgang (Ka 61). However, a new class of reaction processes, namely, deep inelastic collision was found in 1970 (Gr 70, Ga 70, Mo 74). This collision process has an intermediate character between the compound and the direct nuclear reaction processes, i.e., it is characterized by:

(1) A large amount of relative kinetic energy is dissipated into the internal excitation of both nuclei,

(2) The reaction products preserve their approximate identities as the projectile and the target nuclei with respect to their mass and atomic numbers,

(3) The angular distribution of reaction products is forward peaking, suggesting a shorter interaction time than that of the compound process where the angular distribution of the reaction products is more or less isotropic.

The facts (1) and (2) suggest the existence of attractive nuclear forces between the interacting nuclei and at the same time large repulsive force which hinders two nuclei from fusing together. The collision process for the deep inelastic collision is described as follows. The projectile and the target nuclei touch together at the nuclear surface and form a di-nuclear system (DNS) which may look like a dumbbell as shown in Fig. 1. The system does not result in fusion, because the system is rotating fast with the large orbital angular momentum carried by the interacting system and the centrifugal potential is too large for the two nuclei to fuse together. At the last stage of the collision process, the system is disrupted into the projectile-like and the target-like fragments by the Coulomb repulsion (Vo 78).

A typical energy spectrum of the projectile-like-fragment produced in a heavy-ion reaction is shown in Fig. 2 (Ar 73). Two peaks are clearly seen in the spectrum. One peak displayed at a small energy loss is sharp and the reaction products have almost the same energy per nucleon (velocity) as that of projectile, while the other at a large energy loss is broad and extends down to the Coulomb energy. These two peaks are considered to be produced by

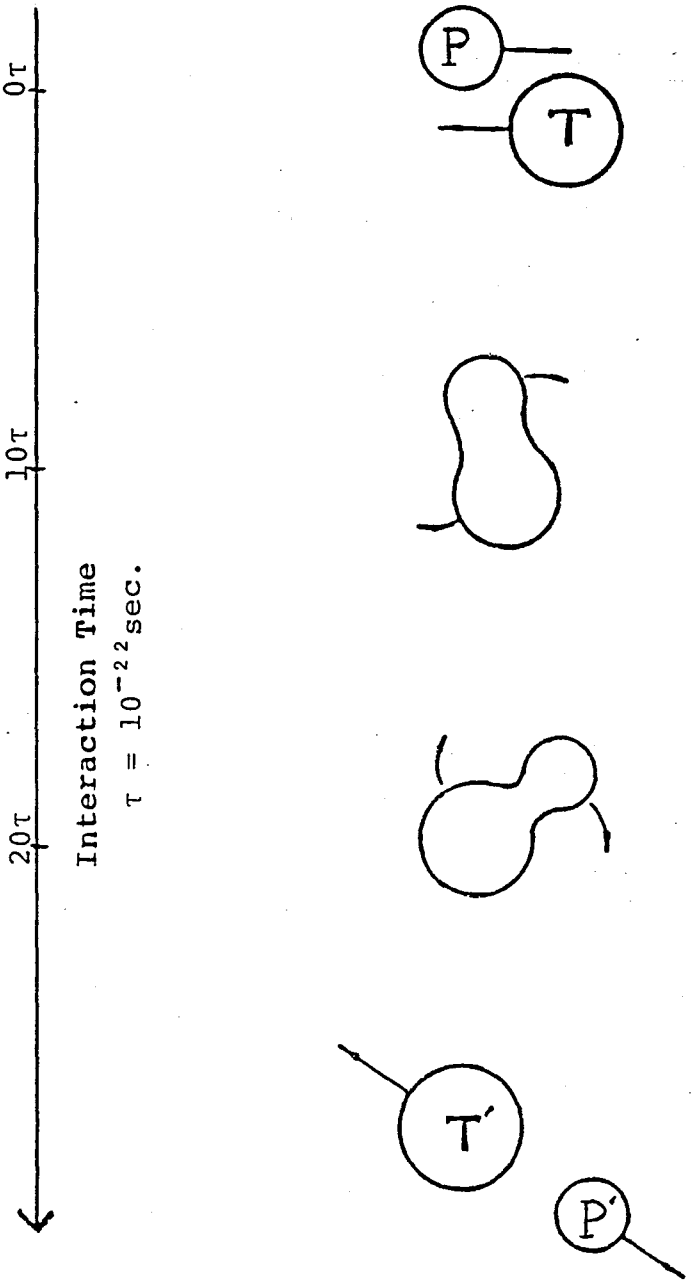

Fig. 1 Formation and decay of di-nuclear system (DNS) with approximate time scale of interaction. Letters in the figure are, P; Projectile nucleus, T; Target nucleus, P'; Projectile-like product, T'; Target-like product.

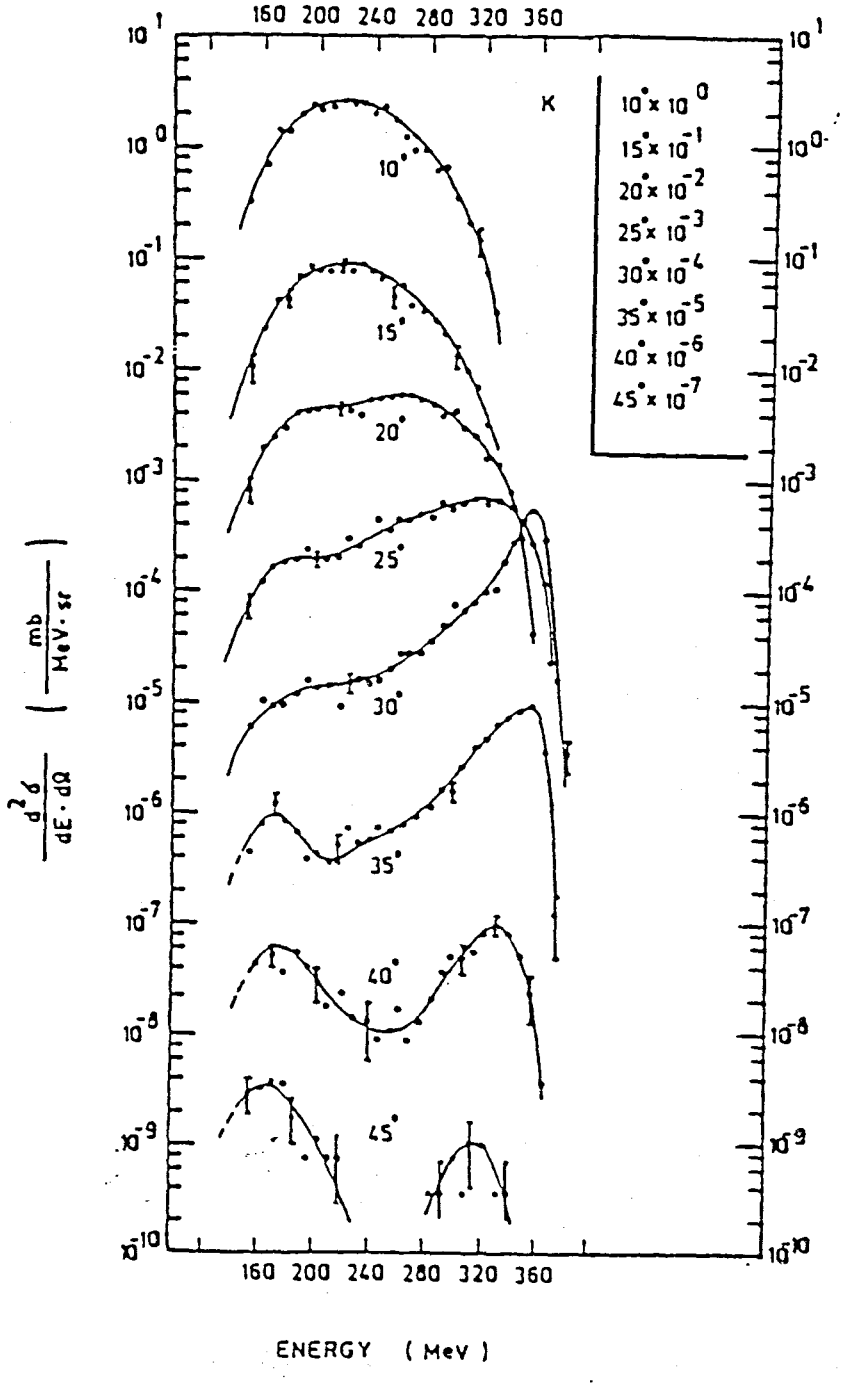

Fig. 2 Energy spectrum of projectile-like-fragments produced in the reaction $^{232}Th(^{40}Ar,K)$ at a bombarding energy of 388 MeV and different scattering angles. The multiplication factor is indicated in the upper right-hand corner (Ar 73).

different reaction mechanisms. The peak with a small energy loss comes from the grazing collision process. This is also called a quasi-elastic collision because the collision proceeds through a direct process and the trajectory of the incident particle does not strongly deviate from the Coulomb orbit. The peak at a large energy loss is not understood in the usual framework of a direct reaction. The large peak width and large energy loss suggest that a large number of nuclear excited levels participate in the collision process. This is the deep inelastic collision.

In an alternative description the heavy-ion collision processes are classified by a relative orbital angular momentum $l\hbar$. In further discussion, $\hbar$ will be dropped. The largest l-value with which the target and the projectile can touch together is defined as the maximum l-value l_{max}. The largest l-value with which the interacting nuclei fuse together is defined as the critical l-value l_{cr}. In other words interacting nuclei fuse together when the l-value is smaller than l_{cr} and the reaction is essentially a binary process when the l-value ranges from l_{cr} to l_{max} (Sc 77). For $l = l_{max}$, the collision occurs almost directly along the Coulomb orbit and for l slightly above l_{cr}; the collision process is deep inelastic. The classification of the collision process as a function of l is shown in Fig. 3.

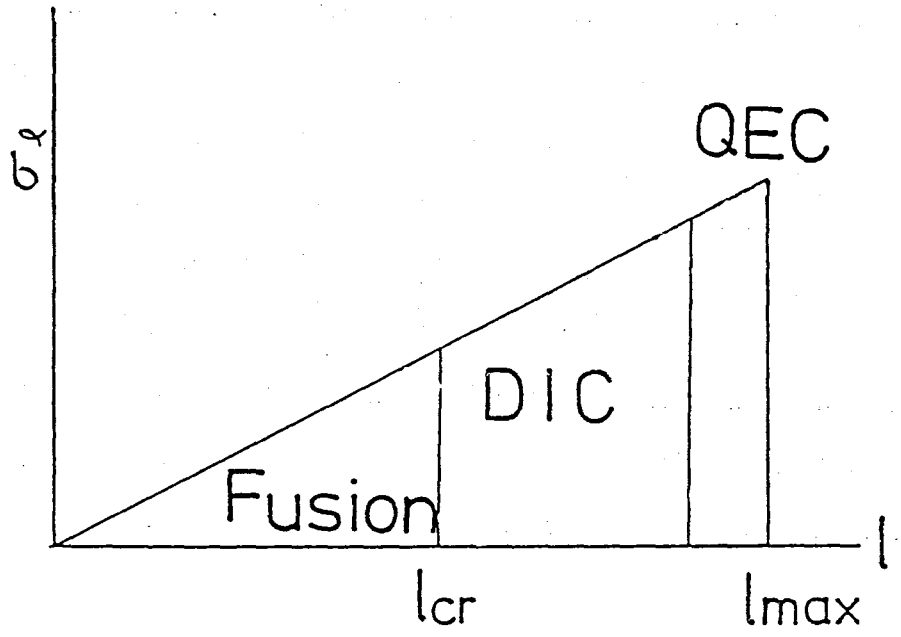

Fig. 3 Classification of heavy-ion reaction mechanism according to the incident orbital angular momentum quantum number l. DIC and QEC mean the deep inelastic collision and the quasi elastic collision, respectively.

2-2 Macroscopic frictional process of heavy-ion collisions

Incident nucleus with orbital angular momentum between l_{max} and l_{cr} is deflected forward from the Coulomb trajectory by the attractive nuclear force. The deflection becomes larger as l decreases due to the larger overlap of the two nuclei. The incident nucleus may thus be deflected to the opposite side of target nucleus for an l small but slightly larger than l_{cr}. This situation is shown in Fig. 4. Contour map representation of reaction cross sections helps understand the reaction mechanisms schematically (Wi 73). Fig. 5 shows such a contour map for K isotopes produced in the reaction ^{232}Th(^{40}Ar,K) at an incident energy of 388 MeV (Ar 73). A large sharp peak is clearly seen for the quasi elastic collision at the grazing angle. A ridge can be traced to forward angle and to smaller kinetic energies. Another ridge is seen at lower energy and forms the deep inelastic peak at backward angles. The low energy ridge can be regarded as a continuation of the high energy ridge coming from the opposite side. Schematic illustrations of a cross section contour and of deflection in the reaction process are shown in Fig. 6. Energy loss and deflection of orbit can be explained by a classical model incorporating nuclear frictional forces. Classical Newton equations of motion, which include the dissipative term are (Gr 74, Si 76)

$$\mu\ddot{r} = -\frac{d}{dr}(V_n(r)+V_C(r)+V_l(r))-C_rF(r)\dot{r} \quad , \tag{2-4}$$

$$\frac{d}{dt}(\mu r^2\dot{\theta}) = -C_\theta r^2F(r)\dot{\theta} \quad , \tag{2-5}$$

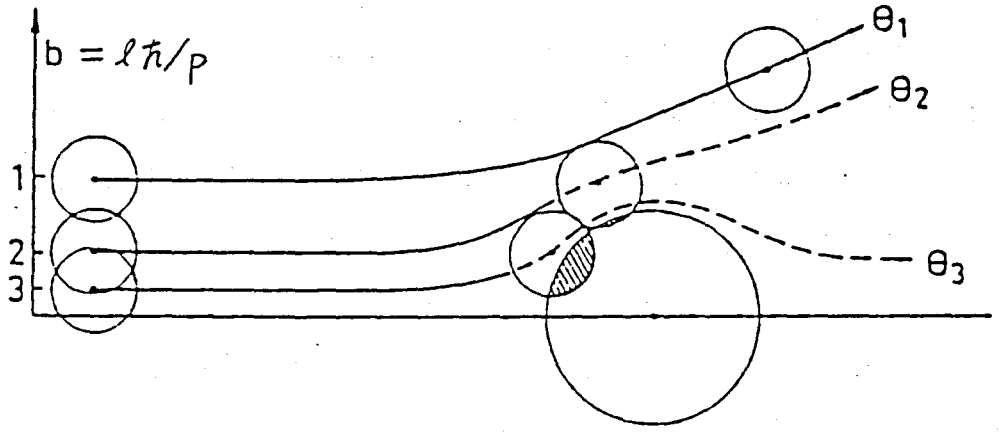

Fig. 4 Deflection of a projectile orbits with various values of the incident orbital angular momentum quantum number l.

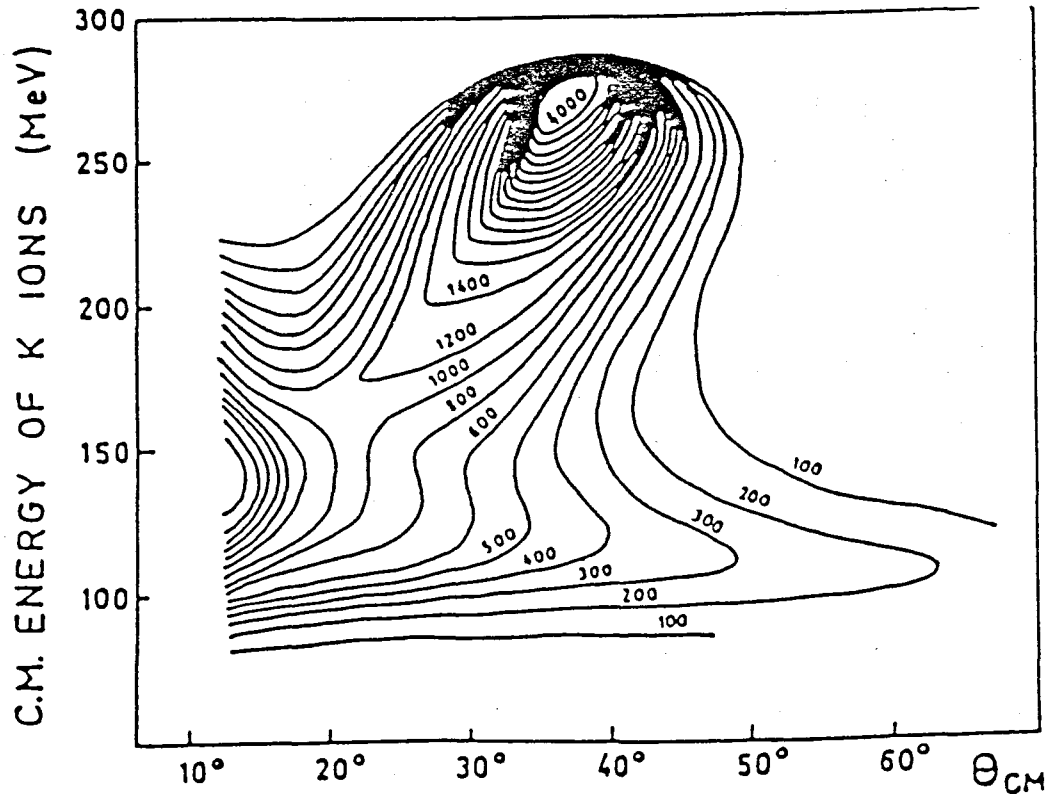

Fig. 5 Contour plot of double differential cross section $d^2\sigma$ / dE·dθ (Wilczynski plot) for the transfer reaction $^{232}Th(^{40}Ar,K)$ at a bombarding energy of 388 MeV (Wi 73). The center-of-mass scattering angle θ_{cm} of the projectile-like-fragment is plotted along the abscissa. The ordinate shows the c.m. kinetic energy of K isotopes. The differential cross sections are in units of μb/MeV·rad.

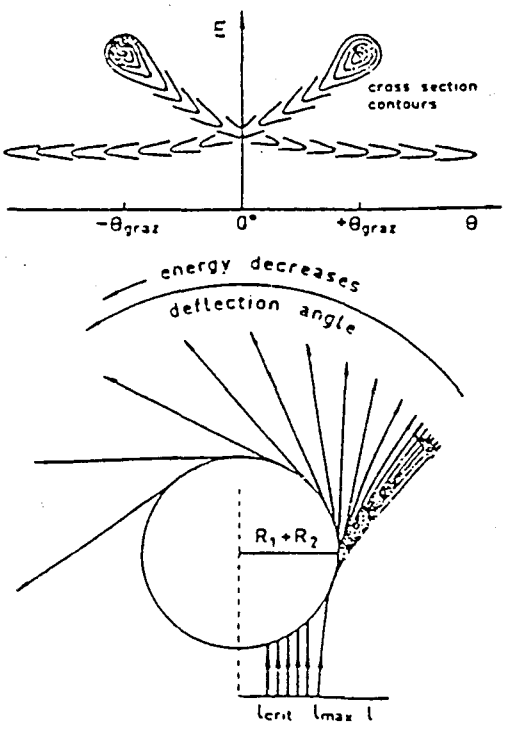

Fig. 6

A schematic illustration of a Wilczynski plot and its interpretation in the deflection process of trajectories.

where r and θ are relative radial and angular coordinates between the target and the projectile nuclei, $V_c(r)$, $V_n(r)$ and $V_l(r)$ are Coulomb, nuclear and centrifugal potentials, respectively. Here C_r and C_θ are the radial and the tangential parts of the frictional coefficient and F(r) is the form factor of the frictional forces and is defined as the square of the nuclear force (Gr 74) ;

$$F(r) = \left(\frac{dV_n(r)}{dr}\right)^2 \quad . \tag{2-6}$$

Alternatively it can be expressed as a volume integral of the overlapped region of the two nuclei (Si 76) ;

$$F(r) = \int \rho_1 \rho_2 d\tau \quad , \tag{2-7}$$

where ρ_1 and ρ_2 are the density distribution of the two colliding nuclei. Scattering angle and kinetic energy of the reaction products can be obtained by integrating the equations. Wilczynska et al. employed the latter form factor and reproduced the mean orbit in the scattering-angle and kinetic-energy plane. The result of their calculation is shown in Fig. 7 superimposed upon the experimental results (Si 76). Here both C_r and C_θ are 2×10^{-20} MeV·s·fm.

An angular momentum transfer process is caused by the tangential component of the frictional force $C_\theta F(r)$. The projectile-like-fragment is polarized by the transfer of a part of the incoming orbital angular momentum. The sign of the polarization is different for the products coming from both sides of the target nucleus, as shown in Fig. 8. Note that positive polarization is taken to be parallel to $\vec{k_f} \times \vec{k_i}$. Here $\vec{k_f}$ and $\vec{k_i}$ are the outgoing and incoming wave vectors, respectively. This definition is

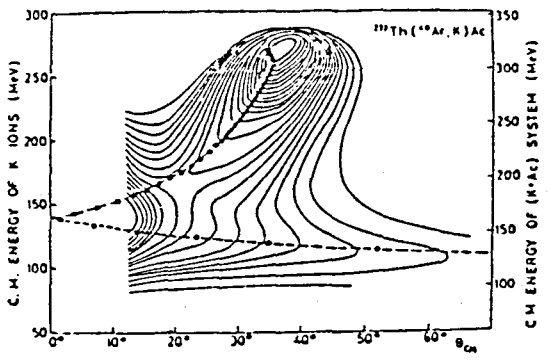

Fig. 7 Calculated mean orbit in the contour plane superimposed on the experimental data. The circles indicate the predicted correlation between the scattering angle and the final energy for different values of the incident orbital angular momentum ranging from l = 180 $\hbar$ to 250 $\hbar$ (Si 76).

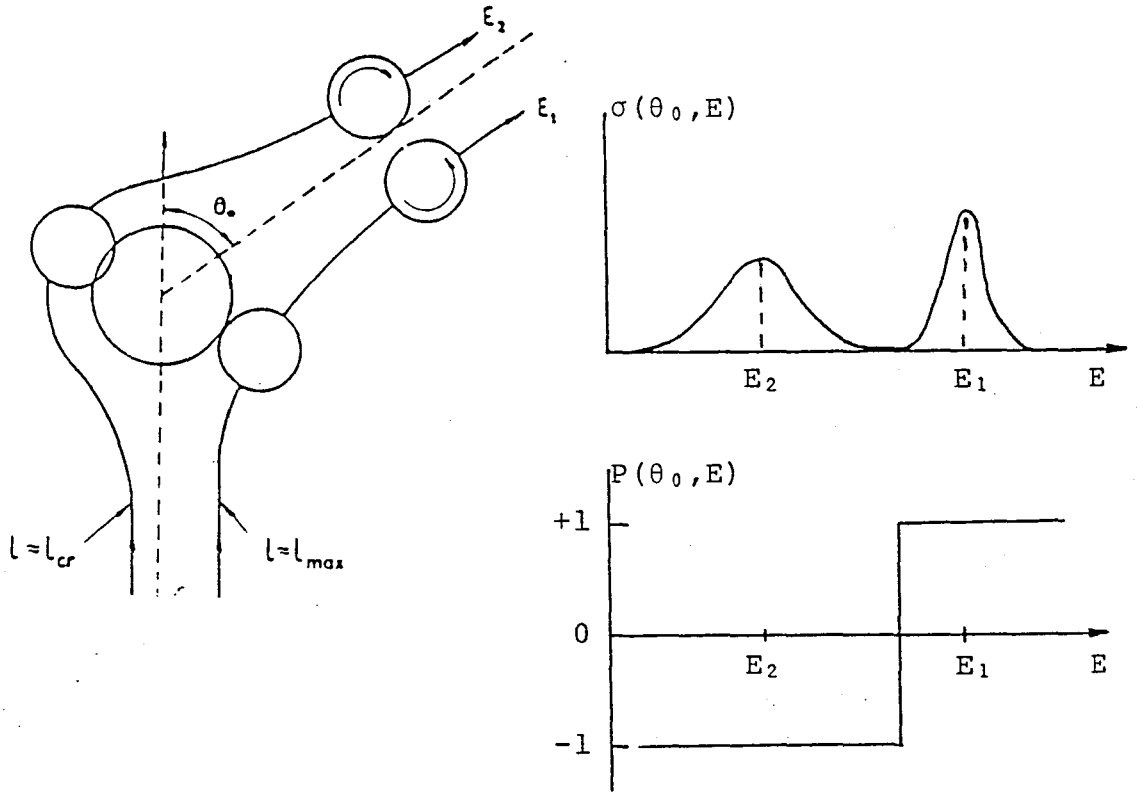

Fig. 8 Expected polarization and energy spectrum of projectile-like-fragment produced along various orbits in heavy-ion reactions within the framework of the frictional model.

opposite to the Basel convention. The relation of the energy spectrum and sign of polarization is also shown in Fig. 8. The sign is expected to be positive for quasi elastic collision and can be negative for deep inelastic collision, if the latter process involves a reaction trajectory which is deflected to the other side of the target nucleus (negative angle deflection). Such dependence of the polarization on the kinetic energy loss have been observed in our previous work (Ta 78).

The frictional force is considered to originate from nucleon exchange processes between the target and the projectile nuclei (Bl 77). The relative kinetic energy loss E_{loss} arising from the exchange of a nucleon between the two nuclei is calculated under the assumption that the linear momentum of the transferred nucleon is conserved in the exchange process and is expressed as

$$E_{loss} = E_{rel}\,\frac{2}{A_1+A_2}\left(\frac{A_2}{A_1}+\frac{A_1}{A_2}+1\right)\left(1-\frac{1}{2A_1}-\frac{1}{2A_2}\right) \equiv E_{rel}\cdot K \ , \qquad (2\text{-}8)$$

where the relative kinetic energy E_{rel} is defined as $E_{rel}=E_{cm}-V_c$ and K is the replacement for the simplification of further discussion.

Since A_1 and A_2 are larger than unity and the mean free path of nucleon in nuclei is larger than the size of nucleus, the nucleon exchange can be replaced by the continuous transport of nuclear matter at the touching surface of nuclei. Thus Eq. (2-8) can be rewritten as a differential equation;

$$-\frac{dE_{rel}}{dn} = E_{rel}\cdot K \ . \qquad (2\text{-}9)$$

The solution to this differential equation is given by the exponential function

$$E_{rel} = E_i exp(-Kn) \ , \qquad (2\text{-}10)$$

where E_i is the initial relative kinetic energy and n is the nucleon exchange number. This energy dissipation process caused by nucleon exchange can be interpreted in terms of phenomeological frictional force, $F_{fric.}$, which is proportional to the relative inter-nuclear velocity, v_{rel}, as $F_{fric.} = -kv_{rel}$, where k is the averaged friction constant. The higher-order terms of $F_{fric.}$ for v_{rel} is neglected in an first approximation where the speed of nucleon in nuclei is much higher than the inter-nuclear translational speed (Co 80). The rate of energy dissipation caused by the frictional force is expressed by the same differential equation as Eq. (2-9) and reads

$$-\frac{dE_{rel}}{dt} = \frac{2k}{\mu}E_{rel} \quad . \tag{2-11}$$

where μ is the reduced mass. The solution to the differential equation is

$$E_{rel} = E_i exp\left(-\frac{2k}{\mu}t\right). \tag{2-12}$$

By comparing Eq.(2-10) with Eq.(2-12), the correspondence between the nucleon exchange number and the friction constant is obtained as

$$\frac{2k}{\mu}t = Kn \quad . \tag{2-13}$$

The nucleon exchange rate N is defined as

$$N = \frac{n}{t} \quad . \tag{2-14}$$

The frictional constant k becomes

$$k = \frac{\mu KN}{2} \quad . \tag{2-15}$$

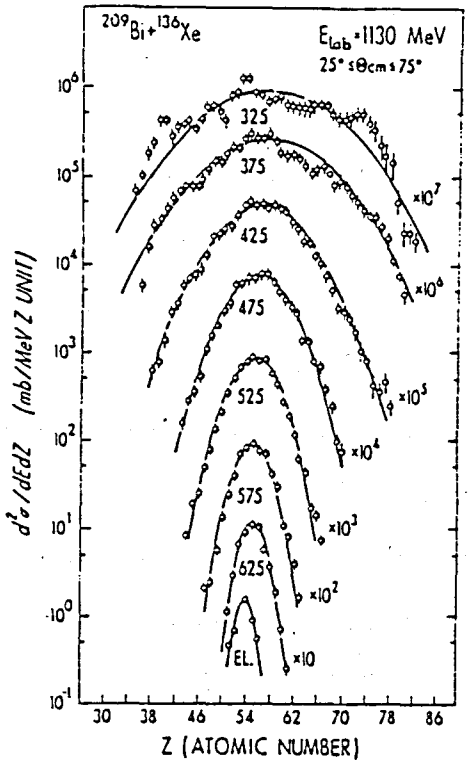

- a -

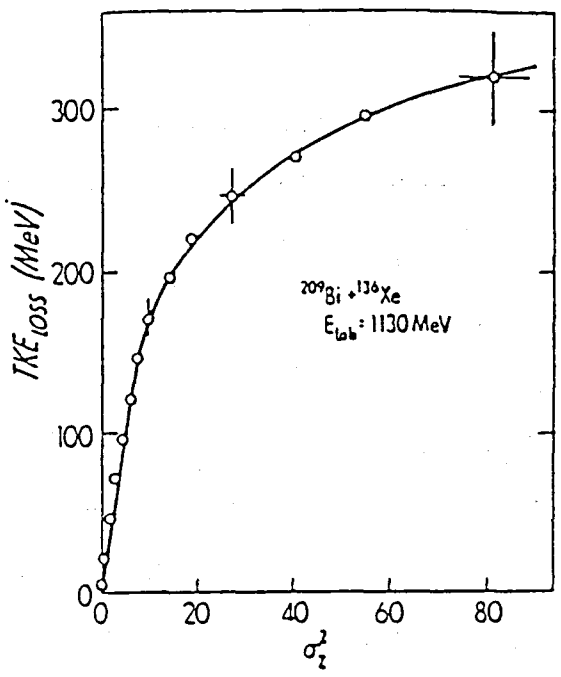

- b -

Fig. 9-a The distribution of projectile-like-fragments produced in Bi+Xe reaction for atomic number Z and total kinetic energy TKE (top of curve). The TKE bins are 50 MeV wide. The curves represent Gaussian fits. The distribution at the bottom corresponds to elastically scattered Xe ions and illustrates the experimental Z resolution (Sc 76).

Fig. 9-b The experimental kinetic energy loss TKE loss, as a function of σ_Z the variance of the distribution of projectile-like-fragments at atomic number z. The result calculated from the nucleon transport model is superimposed on the experimental data (Sc 76).

Nucleon transport phenomena between target and projectile has been observed experimentally(Sc 76). The atomic number distribution of the projectile-like-fragments produced in the reaction Xe + Bi is shown in Fig. 9-a as a function of total kinetic energy and the variance of the atomic number distribution is shown in Fig. 9-b as a function of the total kinetic energy loss. The variance becomes larger with increase of kinetic energy loss. The increase of the variance of the atomic-number distribution was considered to originate from statistical fluctuation in the nucleon exchange process. After n time exchange of nucleon the statistical fluctuation is $\sigma = \sqrt{n}$.

By using the relation $\sigma^2 = n$, the kinetic energy after n time exchange of nucleon is rewritten as a function of σ^2;

$$E_{rel} = E_i exp(-K\sigma^2). \tag{2-16}$$

The relation between the variance σ and the kinetic energy loss is

$$E_{loss} = E_i (1 - exp(-K\sigma^2)). \tag{2-17}$$

By fitting the theoretical curve described by Eq. (2-17) to the experimental result in Fig. 9-b, the energy loss per nucleon exchange was found to be about 8 MeV (Hu 76) at the early stage of the nuclear reactions. Kinetic energy of relative motion is thus transferred into internal nuclear excitation.

The angular momentum transfer from the orbital motion to the internal degree of freedom is also understood as a result of nucleon exchanges. If one nucleon was transferred from one of the colliding nuclei to the other at the nuclear surface, the transformed angular momentum J from the relative orbital motion into the intrinsic spin of the residual nucleus is written as

$J = Rmv_{rel}/\hbar$, where R is radius of accepter nucleus, m is the mass of the transferred nucleon and v_{rel} is relative velocity between the colliding nuclei. If the nucleon transfer would occur in the reaction plane, the transferred angular momentum parallel to the reaction normal would be $n \cdot J$ after n time transfer of nucleon. However angular momentum generated due to the vector sum of the randomly oriented Fermi motion of transferred nucleons $J_f = 2n^{1/2}R(2mE_f/3)^{1/2}$, where E_f, the Fermi energy of the transferred nucleon, (Va 79), has to be included in the total transferred angular momentum. The total angular momentum transferred J_t is thus given by $J_t = (J^2 + J_f{}^2)^{1/2}$. The spin polarization P is determined to be $P = (J / J_t)$ and increases in proportion to the number of transferred nucleon (Va 79).

One of the most interesting and useful properties of deep inelastic collisions was observed from the isotope production cross section(Ar 71). A logarithmic relation, $\log(d\sigma/d\Omega) = \text{Constant} \cdot Q_{gg}$, was found. The quantity Q_{gg} is a reaction Q-value with which the projectile-like and target-like-fragments are produced in their ground states. Fig. 10 shows the Q_{gg} relationship with isotope production cross section. The proportionality constant, i.e., the slope of the logarithmic cross section as a function of Q_{gg}, is almost the same for all isotopes produced. This fact suggests the existence of partial equilibration in an isotope production process, which has the same nuclear temperature corresponding to the constant of the inclination. The existence of an equilibration means a longer interaction time than that of a direct process. C.K.Gelbke et al. report that the Q_{gg} relationship is realized better when liquid drop values are used for the target mass and for the target-like-fragment mass (Ge 77). This fact means that the nucleus behaves like a liquid drop of nuclear matter and effects of the nuclear shell structure becomes small in these collision process. This systematic relationship can be used to estimate the production cross section for various isotopes.

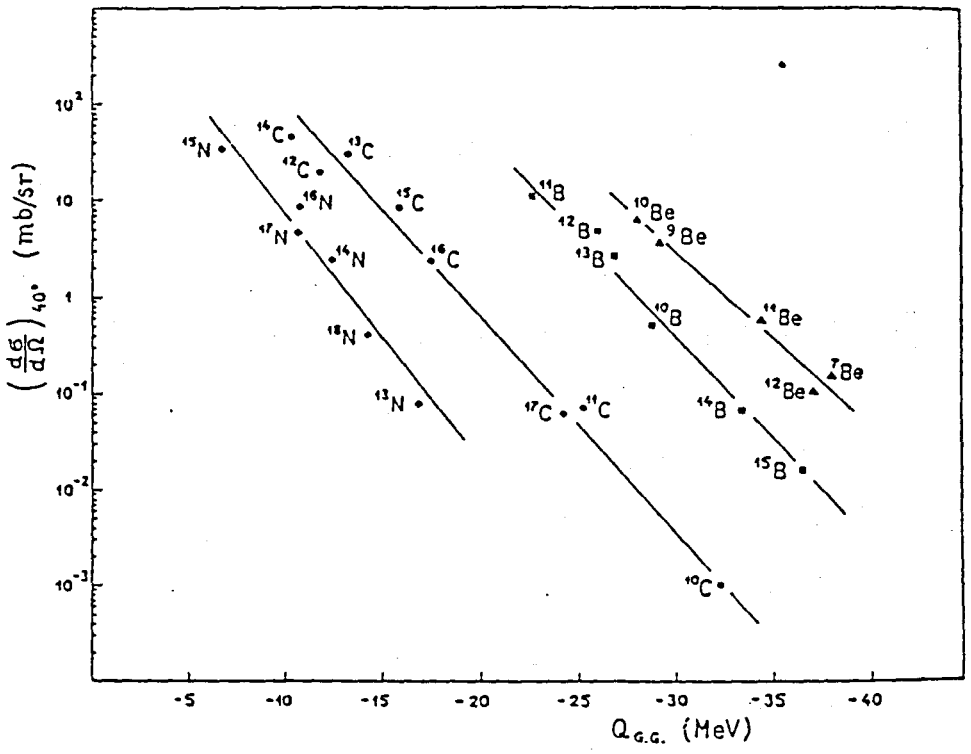

Fig.10 Dependence of differential cross sections for production of various isotopes with Q_{gg} for the reaction ^{232}Th (^{16}O,X) at an incident energy of 137 MeV (Ar 71).

2-3 Microscopic treatment of heavy-ion collisions

The importance of the direct process in heavy-ion reactions was pointed out for the quasi elastic region by our previous work (Su 77). Polarization of ^{12}B produced in the reaction $^{100}Mo(^{14}N,^{12}B)$ was measured at an incident energy of 90 MeV as a function of reaction Q-value. Polarization was large and negative in the region of small kinetic energy loss and became positive with the increase of the kinetic energy loss as shown in Fig. 11. The reaction Q-value, where the polarization crossed zero, corresponded to the maximum of the energy spectrum. The behaviour of the polarization was not understood in the framework of the frictional model. Instead, it was interpreted in terms of direct transfer of two protons from the projectile to the target nuclei(Is 78). The contribution of the direct processes was not realized until polarization was measured by us in heavy-ion collision.

A nucleon cluster c is transferred from the projectile nucleus A to the target nucleus B ;

$$B + (c + a) \longrightarrow (B + c) + a \qquad \text{with } A = (c + a).$$

The cluster is assumed to be in the orbit (l_1,λ_1) in the initial state and in the orbit (l_2,λ_2) in the final state. Here l and λ are the orbital angular momentum and its component along the z-axis perpendicular to the reaction plane. The relative velocity between both nuclei is v. The transfer process is shown in Fig. 12. The difference Δk in linear momenta between the initial and the final states is

$$\Delta k = \frac{mv}{\hbar} - \frac{\lambda_1}{R_1} - \frac{\lambda_2}{R_2} \quad . \tag{2-18}$$

The difference ΔL in angular momenta is the sum of the difference of

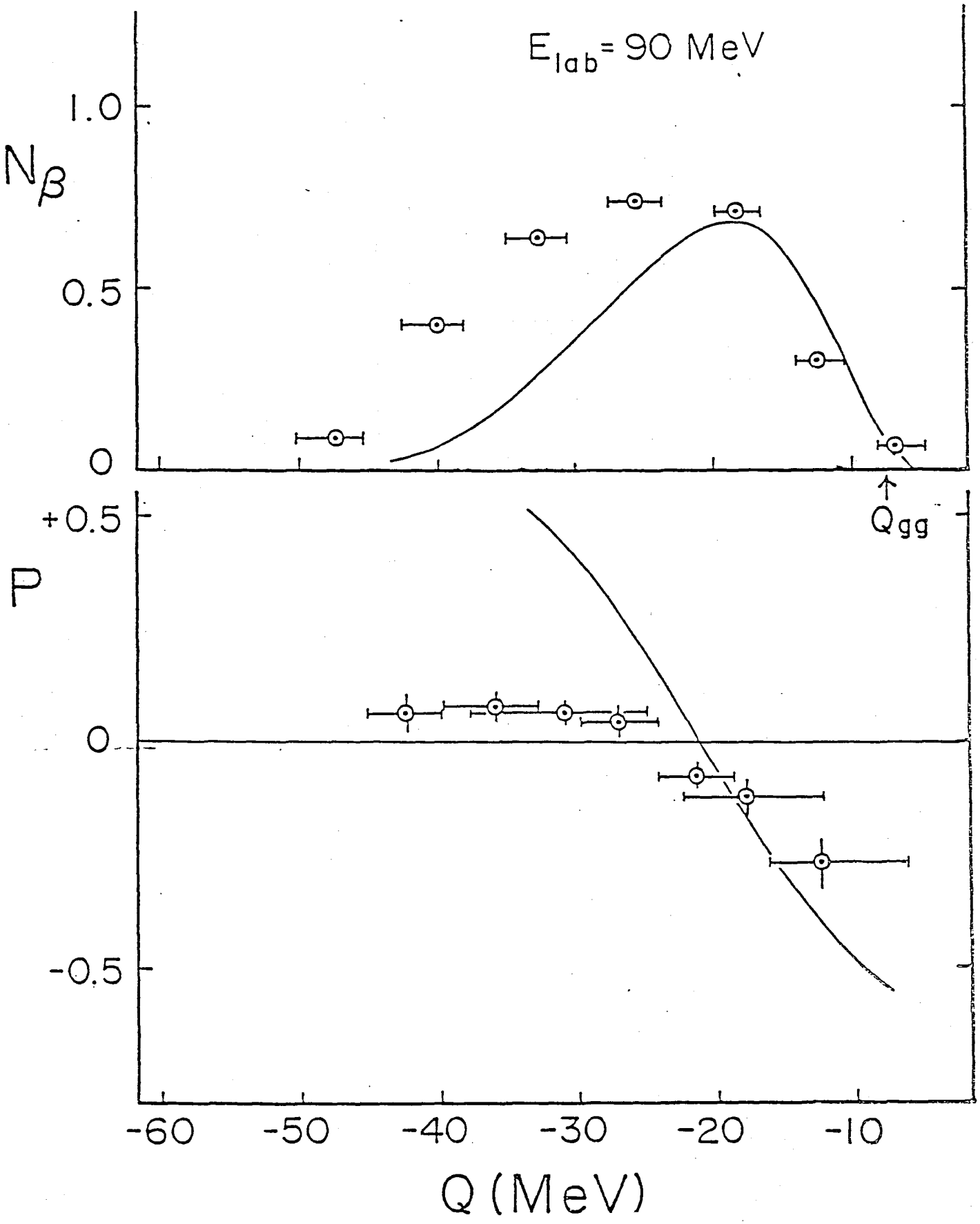

Fig.11 The spin polarization and the energy spectrum of ^{12}B produced in the reaction $^{100}Mo(^{14}N,^{12}B)$ at an incident energy of 90 MeV. The curves are for calculations in terms of the kinematical matching model proposed by Brink (Is 78).

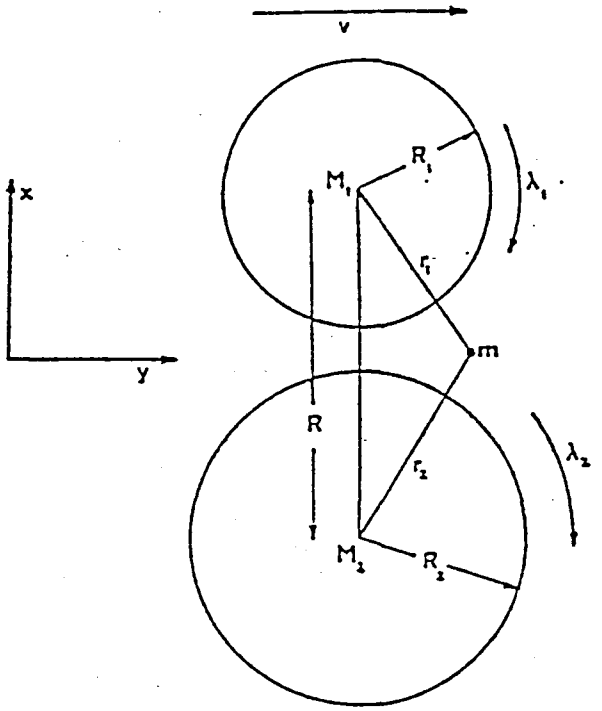

Diagram of the transfer process.

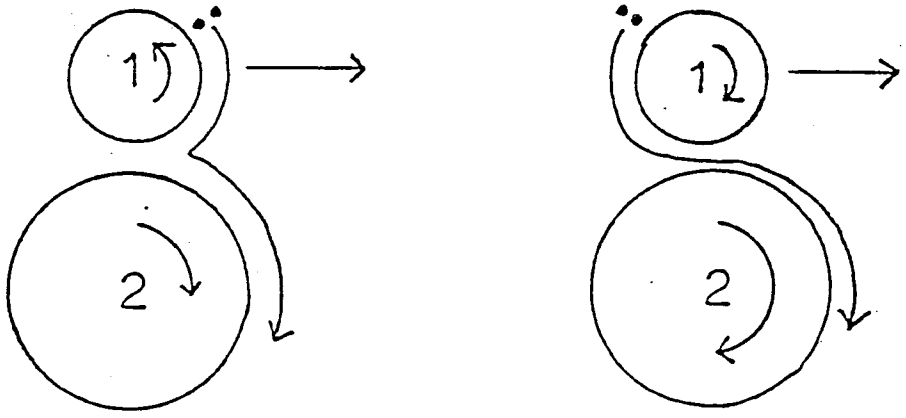

Fig.12 Schematic illustration of the direct cluster transfer process under the kinematical matching model proposed by Brink. The polarization expected in the residue after transfer of a cluster from the specific initial orbit is also shown (Br 72).

internal angular momenta $\lambda_2 - \lambda_1$ and the change of orbital angular momentum $\delta(\mu v R)$. The latter depends upon changes in μ, v and R and can be expressed as (Br 72)

$$\Delta(\mu v R) = \frac{m v}{2\hbar}(R_1 - R_2) + \frac{R}{v\hbar} \cdot \delta\left(\frac{\mu v^2}{2}\right). \qquad (2\text{-}19)$$

The quantity $\delta(\mu v^2/2)$ is just the change of relative kinetic energy. Thus the expression for the difference of angular momenta is

$$\Delta L = \lambda_2 - \lambda_1 + \frac{m v}{2\hbar}(R_1 - R_2) + \frac{R \cdot Q_{eff}}{v\hbar} \quad , \qquad (2\text{-}20)$$

where effective Q-value, Q_{eff}, is defined as $Q_{eff} = Q - (V_{ci} - V_{cf})$. The V_{ci} and V_{cf} are Coulomb energies before and after the transfer of the cluster, respectively and defined as $V_{ci} = Z_1 Z_2 e^2/R$ and $V_{cf} = Z'_1 Z'_2 e^2/R$, respectively. The Z_1 and Z_2 are the atomic numbers of the projectile and target nuclei and the quantities with prime refer to the values of reaction products. It is assumed in the model that the transfer of a cluster is favourable when linear and angular momenta are unchanged in the process, i.e., $\Delta L = 0$ and $\Delta k = 0$. The transfer of a cluster has, however, some probability around $\Delta k = 0$ because of the uncertainty principle, $\delta p \cdot \delta x = \hbar$ which results in some ambiguity in the linear momentum. The angular momentum is exactly conserved in any process so that ΔL is zero. However, with the inconsistency of the model that the internal angular momentum is quantized but that the relative orbital angular momentum is treated classically, may allow small deviations of ΔL from zero. The energy spectra of the reaction products have a maximum at the Q-value determined for $\Delta L = 0$ and $\Delta k = 0$ and have a bell shape distribution around the maximum. This Q-value is defined as a matching Q-value, Q_{match}, and is written as

$$Q_{match} = V_{ci} - V_{cf} - (1/2)mv^2. \qquad (2\text{-}21)$$

The reaction product "a" is polarized by the transfer of the cluster and the sign of the polarization of the product "a" is opposite to the sign of λ_1 because a hole state of the product "a" left after the cluster transfer is observed. Solving the equation with respect to λ_1, we obtain

$$\lambda_1 = \frac{R_1}{\hbar v} \left(\frac{1}{2} mv^2 + Q_{eff} \right). \qquad (2\text{-}22)$$

The quantity λ_1 is positive for $Q > V_{ci} - V_{cf} - (1/2)mv^2$ and negative for $Q < V_{ci} - V_{cf} - (1/2)mv^2$. The polarization then becomes zero at $Q_{match} = V_{ci} - V_{cf} - (1/2)mv^2$. This Q-value Q_{match} also corresponds to the largest probability for cluster transfer, i.e., the peak of the energy spectrum. This model for cluster transfer in heavy-ion reactions was first proposed by Brink and is referred to as the Brink model. A typical example of a calculated polarization of ^{12}B is illustrated with experimental data in Fig. 11.

Refinements of heavy-ion reaction theory from a microscopic view point have been carried out by several people. Kammuri et al. extended the Brink model to curved orbits (Ka 81, Ma 82). Ichimura et al. introduced the matching condition, $\Delta k = 0$ $\Delta L = 0$, in three dimensional space (Ic 83). Udagawa et al. developed a new DWBA calculation for the continuum final states (Ud 78). They replaced realistic nuclear final states by elements of an appropriately chosen analytic function which was determined by χ^2-fitting from a finite range DWBA calculation with numerous possible final states. Polarization of ^{12}B was reproduced by the DWBA calculation for the direct two proton transfer process (Ud 78). They pointed out the importance of target recoil. A characteristic behaviour of ^{12}B polarization in the region of small kinetic energy loss comes from interference between orbital angular

momenta differing by 1 unit and with opposite parity arising from the recoil effects. Even in the deep inelastic region, the experimental data have been well reproduced. By using a three step DWBA calculation, Tamura et al. succeeded in reproducing most parts of the energy spectrum and polarization of ejectiles produced in the inelastic reaction $^{58}Ni(^{16}O,^{16}O')$ (see Fig. 13) (Tm 80, Le 83). However, experimental data in the region of the largest kinetic energy loss was not completely fitted. In the DWBA calculation, some averaging procedures are introduced. The nuclear frictional forces stems from an average for large kinetic energy dissipation. Although the relationship between these averaging treatments is unclear, the origin of frictional forces will probably be established by an exact microscopic treatment of heavy ion collision processes. More elaborate treatments will be required to describe heavy-ion collision at large kinetic energy dissipation.

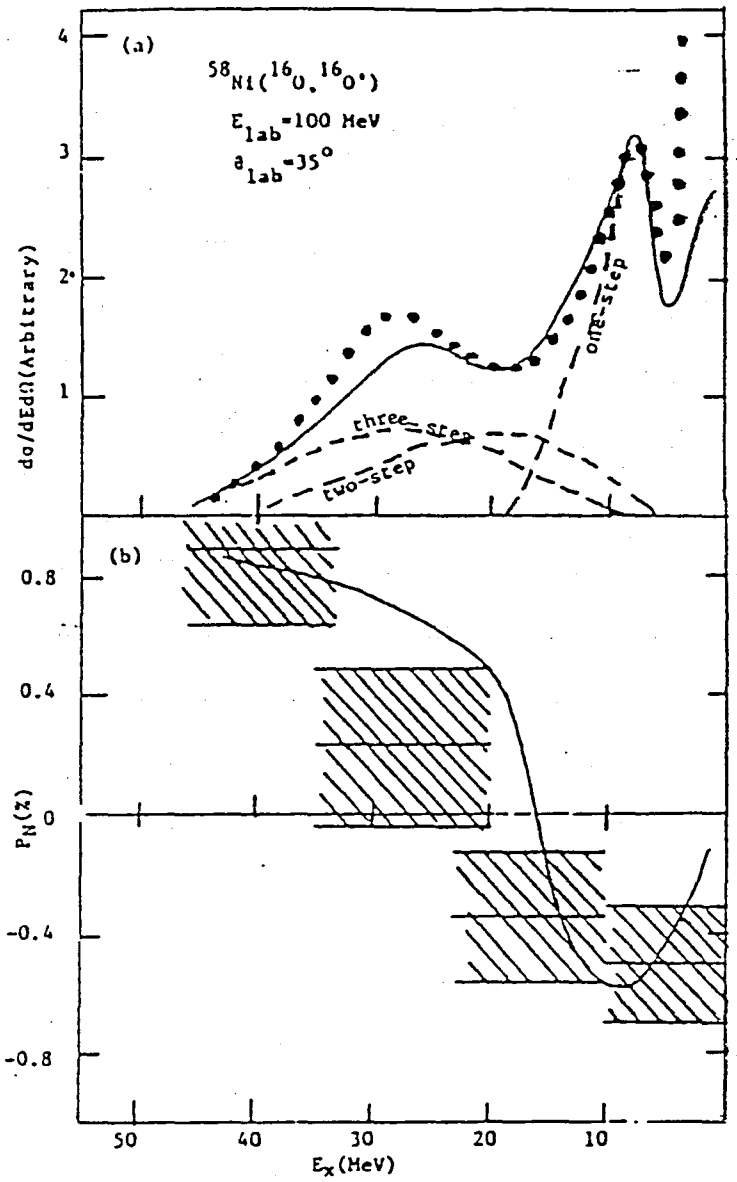

Fig.13 Experimental data of circular polarization in inelastic heavy-ion reaction $^{58}Ni(^{16}O,^{16}O')$ compared with the result of a calculation by use of three step DWBA developed by Tamura et al.(Tm 80)

CHAPTER 3

Experimental Methods

3-1 Basis of the polarization measurement

- a Production and implantation of ^{12}B
- b Hyperfine interactions of implanted ^{12}B and preservation of the polarization of ^{12}B
- c Determination of the polarization
- d Spin control
- e Polarization brought in the γ-ray cascade and particle decay

3-2 Details of experiments

- a Reaction chamber and production of ^{12}B
- b β ray detection
- c NMR
- d Timing control

3-3 Check experiment by use of the (d,p) reaction

3-4 Time and energy spectra of β rays

3-5 Summary of the polarization measurement

Nuclear spin polarization of projectile-like-fragments produced in heavy-ion reaction is expected to be perpendicular to the reaction plane which is formed by the axis of the incident beam and recoil. Thus the reaction products were collected in a scattering angle with finite solid angle in a practical measurement of the polarization, as shown in Fig 14. The experimental conditions for an energy determination of the reaction product, preservation of the polarization and asymmetry detection of β decay then must be optimized. The conditions described in Fig. 14 were the easiest and the most efficient for observation of the spin polarization of ^{12}B produced in ^{14}N induced reaction. The short β-decay half life of 20.3ms of ^{12}B, its high β-decay end-point energy of 13.37 MeV and large asymmetric parameter of -1 simplify the measurement of its polarization.

Considering the above properties of ^{12}B β decay, a beam pulsing method was employed for the ^{12}B production and beam-off counting time. This was essential for the detection of β rays with low background and the control of the ^{12}B spin. Since the reaction product ^{12}B was ejected with large kinetic energy, it could easily be implanted into a stopper foil. An energy-absorber foil of suitable thickness was selected and placed in between the target and the stopper foil to fix the kinetic energy range of implanted ^{12}B. The polarization of this ^{12}B was preserved in the stopper foil throughout its lifetime and determined from the asymmetry of the β decay both with spin inversion as well as without spin inversion in order to eliminate geometrical asymmetries in the detection system. Inversion of the polarization was done by the adiabatic fast passage (AFP) technique.

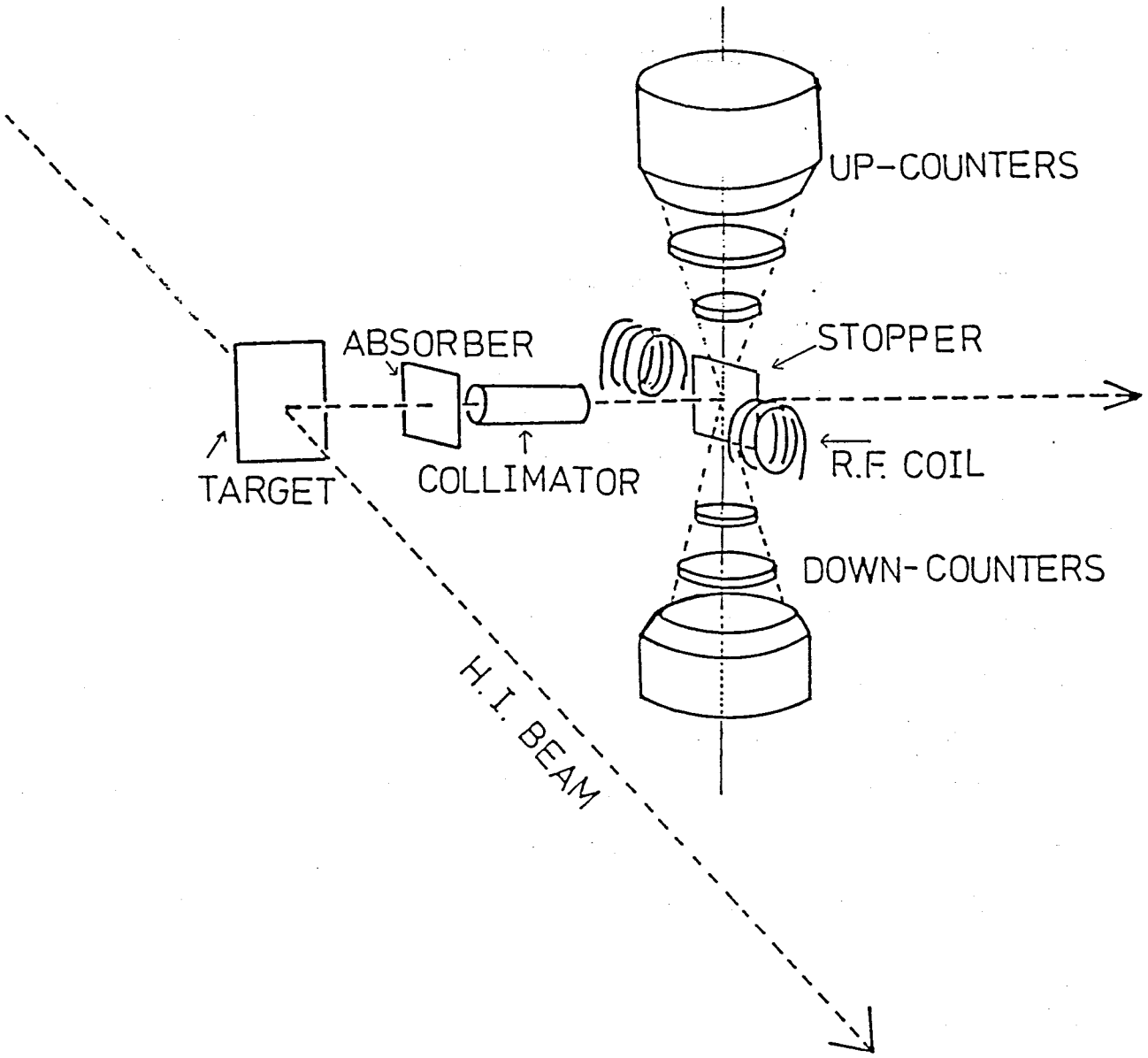

Fig.14 Schematic illustration of the polarization measurement system. The reaction product was collected in a scattering angle with finite solid angle and implanted in a stopper foil. An energy absorber was placed between the stopper and the target to determine the kinetic energy range of the reaction product implanted in the stopper. β rays emitted from the stopper were detected by a pair of counter telescopes placed above and below the reaction plane. A static magnetic field was applied perpendicular to the reaction plane and a set of rf coils was placed around the stopper; an rf magnetic field controlled the spin direction of reaction product implanted in the stopper.

3-1 Basis of the polarization measurement

3-1-a Production and implantation of ^{12}B

The β emitter ^{12}B were selected for the polarization measurement of projectile-like-fragment produced in heavy-ion reaction. Although no specific particle identification technique were used, the energy spectrum and the time spectrum of β rays emitted from the stopper foil were consistent of those of ^{12}B. The β emitters which have a similar lifetime and end point energy as ^{12}B produced in ^{14}N induced reaction are ^{13}B and ^{12}N. The β rays from these β emitters could not be rejected. The production cross sections of ^{13}B and ^{12}N were, however, expected to be less than that of ^{12}B and estimated by using the empirical Q_{gg} dependence. A contribution from ^{13}B was found to be less than 20 % of the total β-ray counts for the targets presently used except for ^{232}Th. The estimated production cross section of ^{13}B in ^{232}Th target was 35 % of the total β-ray counts. The production cross section of ^{12}N was negligibly small compared with that of ^{13}B. The estimated value of production cross sections of ^{13}B are shown in Table 1 as ratios to those of ^{12}B.

The kinetic energy range of ^{12}B implanted in the stopper foil was determined by using the range-energy method. The range of a charged particle in a material is a function of the atomic number Z, mass number A and the velocity v of the particle and given by

$$\text{Range} = f(v)(A/Z^2), \qquad (3\text{-}0)$$

where f(v) is a function of only the velocity of the particle. The range-energy relations for ^{12}B in various materials were calculated from

Target	Q_{gg} for ^{12}B	Q_{gg} for ^{13}B	ΔQ_{gg}	$\frac{\sigma(^{13}B)}{\sigma(^{12}B)}$
^{232}Th	-14.0	-15.8	-1.8	0.50
^{100}Mo	- 9.01	-13.1	-4.1	0.21
^{63}Cu	-13.1	-17.6	-4.5	0.18
^{56}Fe	-13.0	-20.9	-7.9	0.05
^{45}Sc	-12.1	-16.9	-4.8	0.16
^{27}Al	-13.2	-19.0	-5.8	0.11

$$\frac{\sigma(^{13}B)}{\sigma(^{12}B)} = \exp \frac{\Delta Q_{gg}}{T}$$

$$T = 2.6 \text{ MeV}$$

Table. 1 Estimated cross section of ^{13}B.

Mass of target nucleus and target-like-product is calculated from Weitzecker Bethe's mass formula as liquid drop mass. Mass of ^{14}N, ^{12}B and ^{13}B is taken from Table of Isotopes (Le 78).

Mean contamination rate $\sigma(^{13}B)/\sigma(^{12}B)$ is nearly equal to 0.15 except for ^{232}Th target

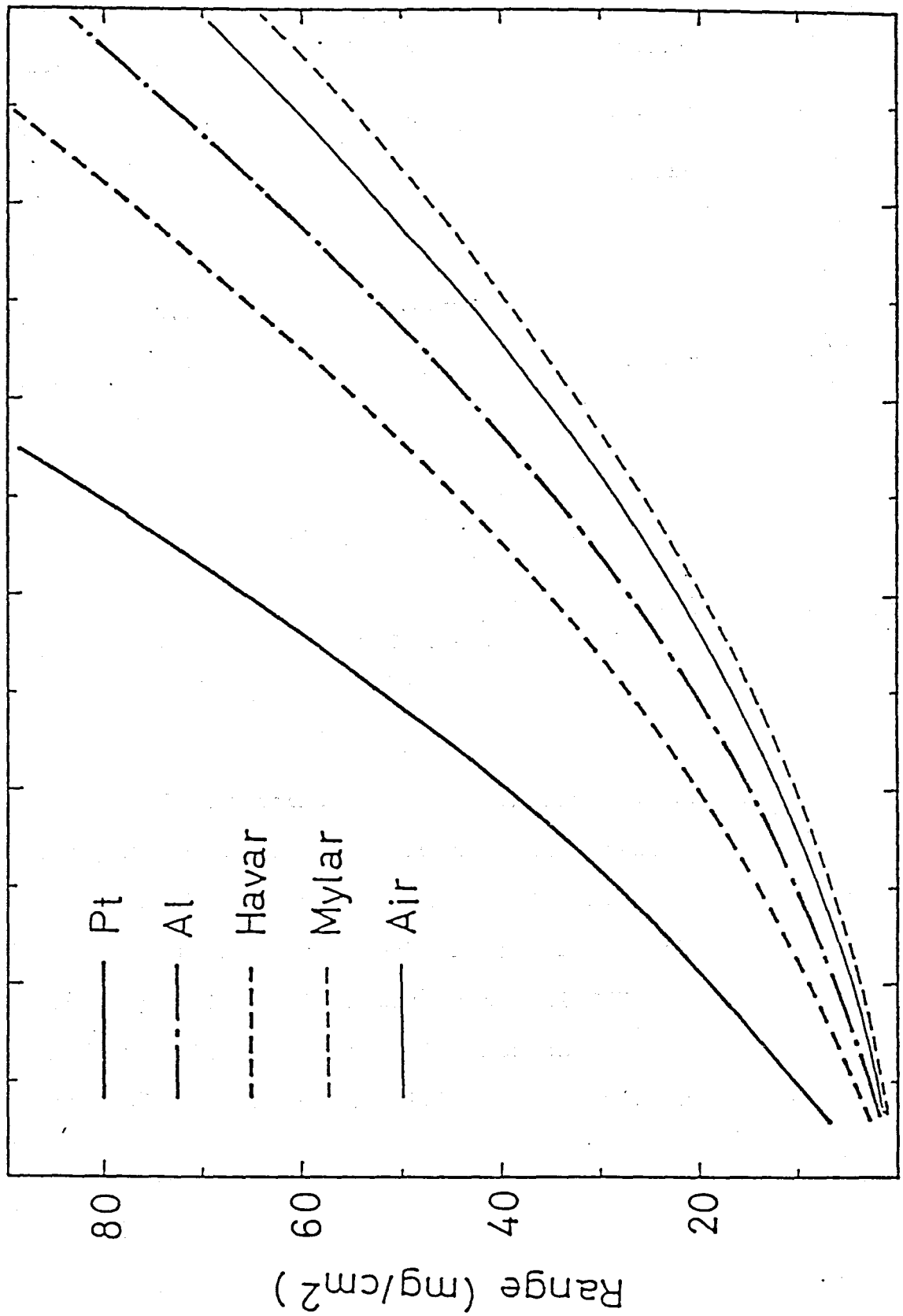

Fig.15 Range of ^{12}B in various materials as a function of kinetic energy.

those for ^{11}B (No 70) by using Eq. (3-0) and are given in Fig. 15.

The kinetic energy of the particle can be expressed as a function of the range of the particle observed. ^{12}B nuclei therefore was emitted out from an energy absorber foil with the energy degraded and stopped in the stopper foil. By choosing suitable thicknesses of the aluminium absorber and a platinum stopper, the energy window of ^{12}B were selected. One example of this method is shown in Fig. 16. The ambiguity of this method comes mainly from the range struggling around the mean range and is estimated to be less than 5 % of the total range.

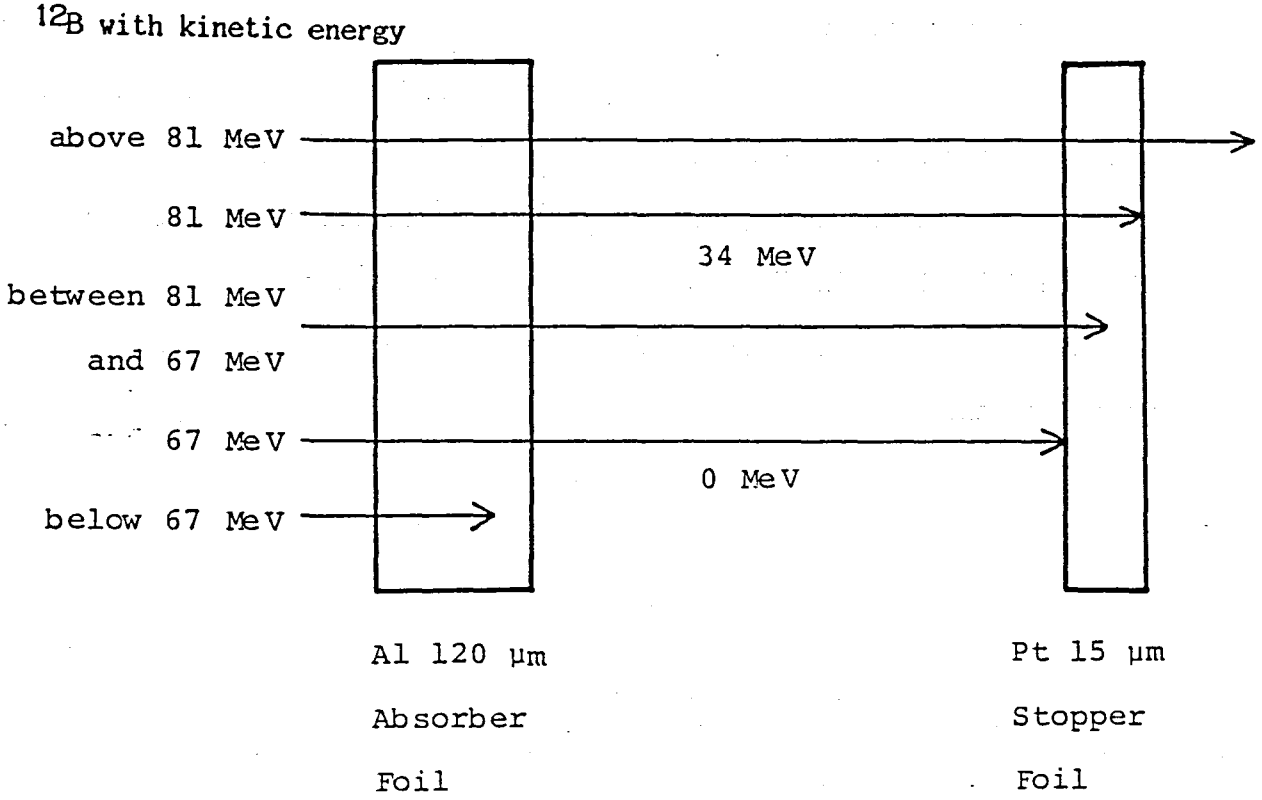

Fig 16 An example of range–energy method employed for the kinetic energy determination of ^{12}B. Reaction products ^{12}B with kinetic energy between 67 MeV and 81 MeV are stopped in the platinum stopper foil of 15 μm thickness by use of aluminium absorber foil of 120 μm

3-1-b Hyperfine interactions of implanted ^{12}B and preservation of the polarization of ^{12}B

Hyperfine interactions of ^{12}B with its atomic electrons and the atoms in the stopping material plays an important roles in preserving the polarization of ^{12}B during its lifetime. When ^{12}B is ejected from the target in vacuum, the nucleus ^{12}B has no atomic electrons. However, after passing through the energy absorber, kinetic energy of boron becomes low enough to capture electrons. The atom can be in various possible charge states during the flight from the absorber to the stopper and the nucleus can be under the influence of strong hyperfine fields. Especially for the charge states of 4^+, 2^+ and 0^+, hyperfine fields caused by unpaired electrons are strong enough to smear out the nuclear polarization immediately. The charge states distribution of the boron ions which pass through a thin foil is shown in Fig.17 as a function of its energy(Ma 68). The ^{12}B nuclei of kinetic energy below 10 MeV may be under the influence of hyperfine fields caused by unpaired orbital electrons. If a strong static magnetic field is applied in the direction of the nuclear polarization, both the atomic spin and nuclear spin of boron ion are decoupled and start to precess independently around the external field. As the magnetic moment of atomic spin is about 2000 times larger than that of nucleus, the nuclear spin is under the influence of of averaged hyperfine field, which is parallel to the external field. Thus the polarization of nuclei can be preserved during the flight in vacuum.

The travel time of ^{12}B in the stopper foil and in the absorber foil is estimated to be less than 1×10^{-12}s. Any electromagnetic interactions which arises in the atomic collision process does not flip the spin direction since the access time τ_a of the interaction is fast, i.e., the inverse of the collision frequency, which is $\tau_a = 10^{-15}$s.

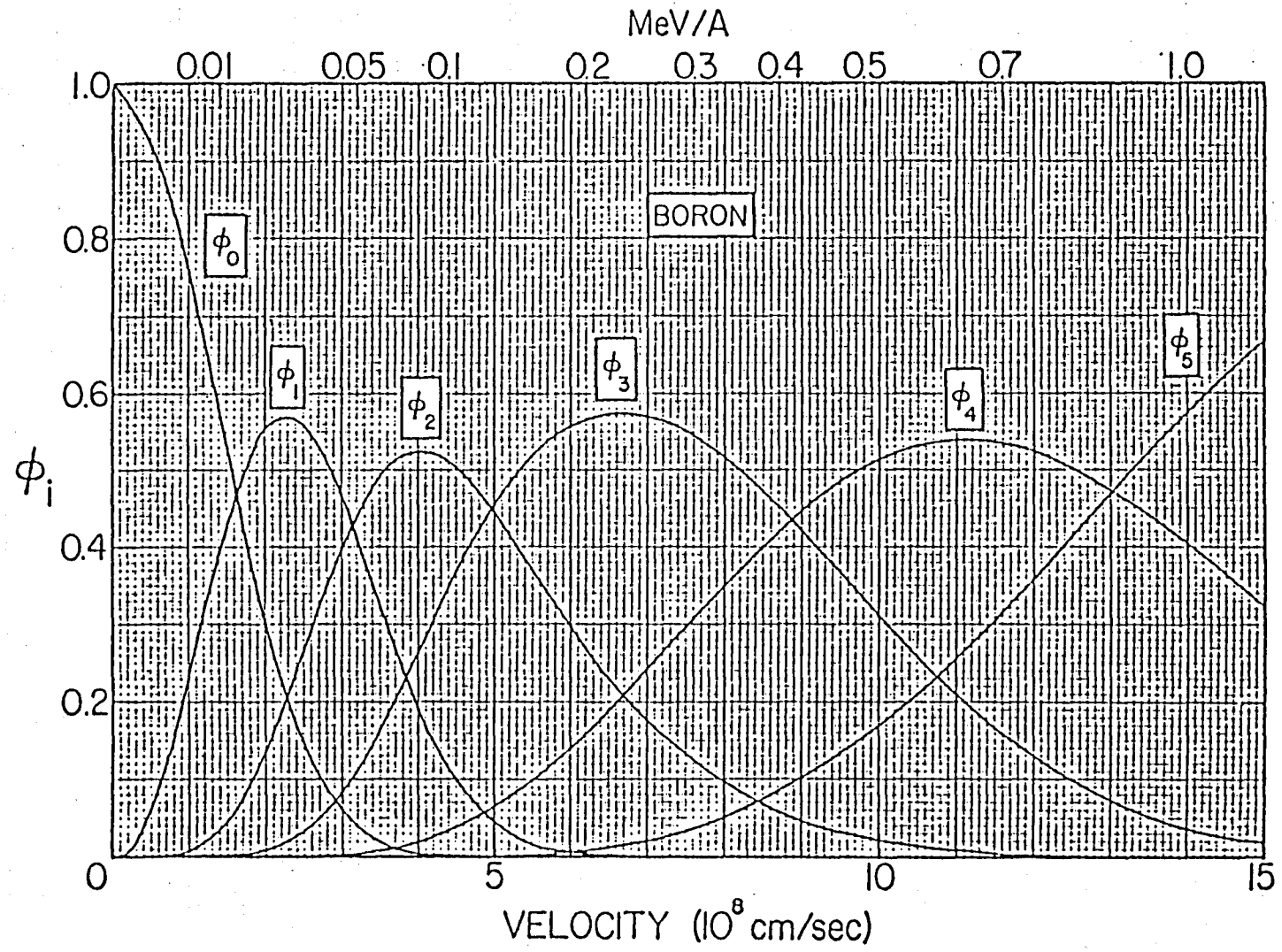

Fig.17 Equilibrated charge states distribution of boron-ion indicated as a function of its velocity. The ϕ_0, ϕ_1, ····· are the intensity distribution in charge states 0, +1, ····, respectively.

After stopping in a stopper foil of fcc metal, ^{12}B lies in an octahedral site and is not under the influence of an electric field gradient because the symmetry of the nearest neighbours is at least 3 fold symmetric about 3 independent axis. From the NMR width the dipoler field at the site is observed to be a few Oe (Mi 73). The nuclear spin of ^{12}B is easily coupled to the external magnetic field when the strength of the field is stronger than a few tens of Oe. As the result, the main origin of the destruction of spin polarization of ^{12}B in fcc metal is the interaction with the conduction electrons. This is mainly due to the contact interaction of the nucleus with the conduction electrons of S-symmetry. The spin lattice relaxation time T_1 in a fcc metal is estimated to be 0.1 s at room temperature by using the Korringer's relation(Kr 50). The material of the stopper foil was chosen as Pt. The relaxation time T_1 of ^{12}B in Pt was observed by J.Wells et al. to be about 1s (We 68) and was also experimentally determined by Sugimoto et al.(Su 68) to be ten times longer than the ^{12}B lifetime. These values are long enough to preserve the polarization of ^{12}B throughout its lifetime.

3-1-c Determination of the polarization

The β ray angular distribution from the spin polarized β emitter (Mo 57) is asymmetric due to parity non-conservation in the weak interaction and written as

$$W(\theta) = 1 + \frac{v}{c} PA\cos\theta, \tag{3-1}$$

where v and c are velocities of β rays and light, respectively. P is the nuclear polarization and A is the asymmetry parameter. The θ is the polar angle of β ray emission relative to the polarization axis.

The spin polarization P with spin I_i is defined by the following equation as

$$P = \sum_{m=-I_i}^{I_i} a(m)m \Big/ I_i \sum_{m=-I_i}^{I_i} a(m) \ , \tag{3-2}$$

where a(m) is the population of the magnetic sublevel with quantum number "m" and is normalized as

$$\sum_{m=-I_i}^{I_i} a(m)=1 \ . \tag{3-3}$$

The asymmetry parameter A (Mo 73)is written as

$$A = \frac{\pm[C_A]^2[<\sigma>]^2\Delta_{if} - 2C_V^*<1>^*C_A<\sigma>\sqrt{I_i/(I_i+1)}}{[C_V]^2[<1>]^2+[C_A]^2[<\sigma>]^2}$$

where Δ_{if} is the coefficient defined as

$$\Delta_{if} = \begin{cases} 1 & \text{for } I_f = I_i - 1, \\ 1/(I_i+1) & \text{for } I_f = I_i, \\ -I_i/(I_i+1) & \text{for } I_f = I_i + 1, \end{cases}$$

where I_f is the spin of the daughter state nucleus after β decay; The upper sign in Eq. (3-4) is applied to the positron emission; The <1> is the Fermi matrix element and $<\sigma>$ is the Gamow-Teller matrix element; C_V is the Fermi coupling constant and C_A is the Gamow-Teller coupling constant. According to the experimental results from ft-values, β decay from $^{12}B_{g.s.}$ to $^{12}C_{g.s.}$ is an allowed pure Gamow-Teller type transition. The decay scheme of ^{12}B is shown in Fig. 18. Therefore the asymmetry parameter A is shown to be -1.

Only β rays with higher energy (>3MeV) were counted in the present experiment in order to reject the low energy background β rays come from long lived β emitters; then v/c can be put equal to 1. The equation of the angular distribution can be rewritten in a simpler form,

$$W(\theta) = 1 - P\cos\theta.$$

We detected the β rays by the two sets of plastic scintillator counter telescopes which were placed above and below the reaction plane, i.e., in the direction of $\theta = 0$ and $\theta = \pi$. The β ray counts are given theoretically by integrating the distribution function around the polar angle as

$$N_{up} = N\varepsilon_{up} \frac{\int_0^{\alpha} W(\theta)2\pi\sin\theta d\theta}{\int_0^{\pi} W(\theta)2\pi\sin\theta d\theta}$$

$$= \frac{N}{4} \varepsilon_{up}(1-\cos\alpha)(2-P-P\cos\alpha) \ , \qquad (3\text{-}6)$$

$$N_{dn} = N\varepsilon_{dn} \frac{\int_{\pi-\alpha}^{\pi} W(\theta)2\pi\sin\theta d\theta}{\int_0^{\pi} W(\theta)2\pi\sin\theta d\theta}$$

$$= \frac{N}{4} \varepsilon_{dn}(1-\cos\alpha)(2+P+P\cos\alpha) \ , \qquad (3\text{-}7)$$

where N_{up} and N_{dn} are β ray counts of $\theta = 0$ and $\theta = \pi$ counters, respectively and α is polar angle subtended by the detector as shown in Fig. 19. N is the

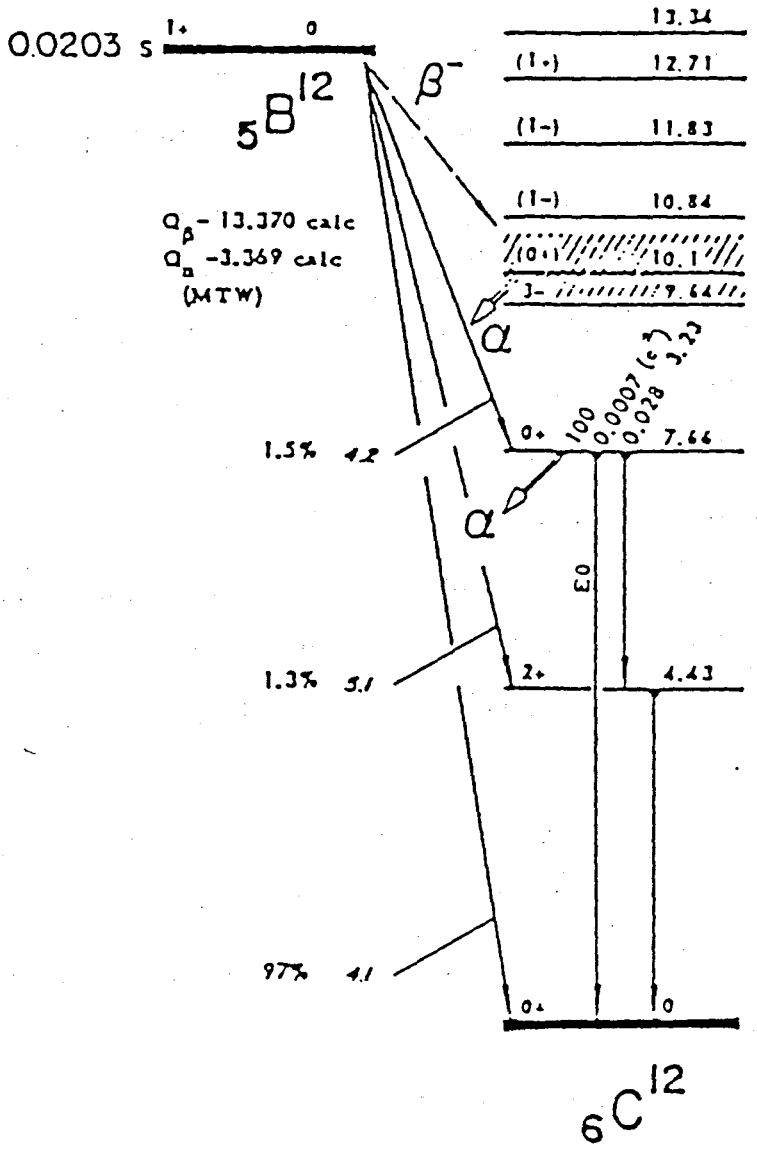

Fig.18 Decay scheme of ^{12}B.

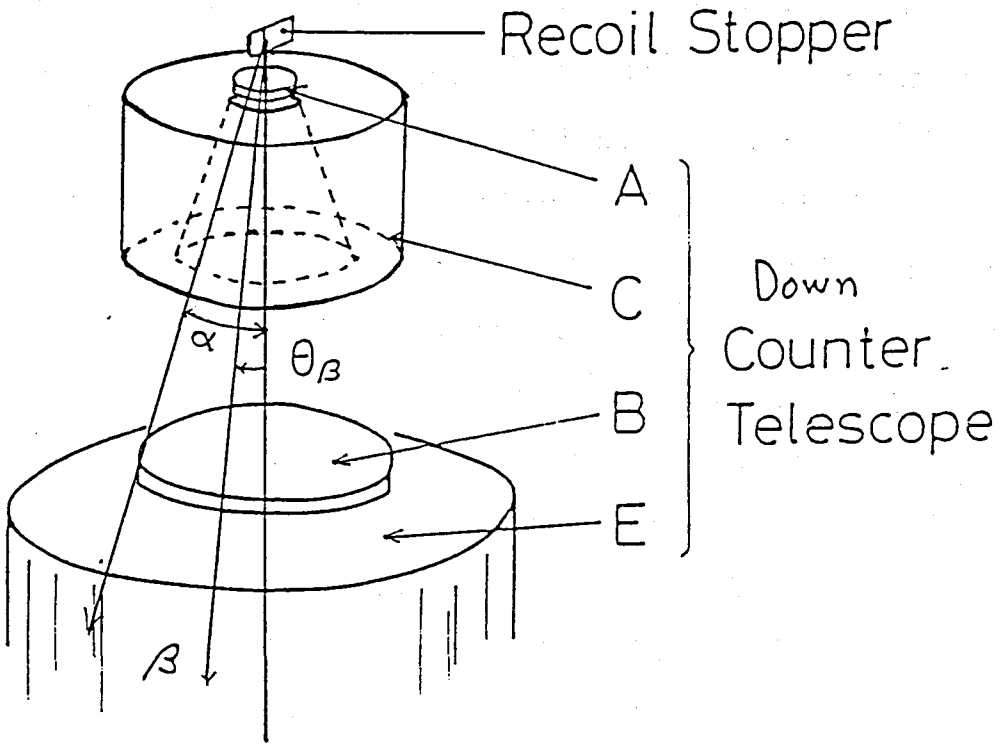

Fig.19 Arrangement of counters for the β ray measurement.
A, B, C and E are names of detectors (see 3-2-c).

total number of decayed ^{12}B nuclei. ε_{up} and ε_{dn} are detection efficiencies of the detectors at $\theta = 0$ and $\theta = \pi$ and also include the geometrical asymmetry of the respective detectors.

The β ray counts after inverting the direction of the polarization by using adiabatic fast passage method (AFP) by the NMR technique are likewise written by changing P to $-\chi P$, where χ is the efficiency of the polarization inversion. The rewritten equation is as follows. The subscript on means the measurement after the spin inversion because the rf field for AFP was induced through on-resonance frequency by means of NMR. The subscript off is used for the measurement without inversion of polarization, i.e., rf field for AFP was applied at off-resonance frequency. The left side of the Eq. (3-6) and (3-7) are rewritten as $N_{up\ off}$=····· and $N_{dn\ off}$=····· , respectively.

$$N_{up\ on} = \frac{N}{4}\,\varepsilon_{up}\,(1 - \cos\alpha)(2 + P\chi + P\chi\cos\alpha)\ . \tag{3-8}$$

$$N_{dn\ on} = \frac{N}{4}\,\varepsilon_{dn}\,(1 - \cos\alpha)(2 - P\chi - P\chi\cos\alpha). \tag{3-9}$$

Then the ratio R of the counting rate given in Eq. (3-10) does not depend on the detector efficiencies.

$$R^2 = \frac{N_{upoff}}{N_{dnoff}} \Big/ \frac{N_{upon}}{N_{dnon}}$$

$$= \frac{(2 - P - P\cos\alpha)(2 - P\chi - P\chi\cos\alpha)}{(2 + P + P\cos\alpha)(2 + P\chi + P\chi\cos\alpha)}. \tag{3-10}$$

By using R, the spin polarization P is obtained independent of the geometrical asymmetry of the measurement system and is written as

$$P = \frac{(3 - \chi)}{(1 + \cos\alpha)} \frac{(1 + R)}{(1 - R)} . \qquad (3\text{-}11)$$

The efficiency of the polarization inversion χ is known to be larger than 0.95 (Mi 73), α was 24 deg, therefore the spin polarization P is determined from the experimental ratio R as

$$P = 1.1 \frac{(1 + R)}{(1 - R)} . \qquad (3\text{-}12)$$

In order to subtract the possible effect of hyperfine interaction in polarization for slow ^{12}B nuclei, in the actual experiment, the polarization was determined from the two asymmetry measurements. As described in 3-1-b, ^{12}B with kinetic energy lower than 10 MeV can be in several possible atomic-charge states. The measurements were both with a thick stopper and with a thin stopper and the thickness of the thin stopper was selected to stop ^{12}B with kinetic energy below 10 MeV. The counts of β rays observed with the thin stopper were subtracted from those with the thick stopper. As a result the counts of the β rays from ^{12}B which had no orbital electrons during flight were obtained. The β ray counts used for the polarization determination were thus:

$N_{up\ on} = N_{up\ on}(thick) - N_{up\ on}(thin).$

$N_{up\ off} = N_{up\ off}(thick) - N_{up\ off}(thin).$

$N_{dn\ on} = N_{dn\ on}(thick) - N_{dn\ on}(thin).$

$N_{up\ off} = N_{dn\ off}(thick) - N_{dn\ off}(thin).$

Here N (thick) means the β ray counts with a thick stopper and N (thin) means that with a thin stopper. The background β rays emitted from the outside of the stopper foil were also rejected by using this subtraction.

3-1-d Spin control

An adiabatic fast passage method (AFP) (Mi 73) was employed in order to invert the polarization of ^{12}B. As mentioned in the introduction of this chapter, the static magnetic field was applied around the stopper foil partly for the purpose of the NMR. A pair of radio frequency (rf) coils was placed around the foil in the reaction plane (see Fig. 14) and linear rf magnetic field was produced for NMR. The magnetic moment μ precesses around the external static magnetic field with the Larmor frequency $\nu_L = \omega_L/2\pi = \gamma H_0/2\pi$, where γ is the gyromagnetic ratio of a nucleus (see Fig. 20). When the linear rf magnetic field $2H_1\cos\omega$ is induced perpendicular to the external static magnetic field, the magnetic moment μ precesses around an effective magnetic field, i.e., the external magnetic field $\vec{H}_0$ reduced by $(\vec{\omega/\gamma})$ and $\vec{H}_1$.

(Note that the effective rotating strength H_1 obtained by the linear field $2H_1\cos\omega t$ is $|H_1 e^{i\omega t}| = H_1$)

This phenomenon is intuitively understood in the rotating coordinate system which rotates simultaneously with the $\vec{H}_1$. In this coordinate the strength of reduced external magnetic field $\vec{H}_0'$ is as

$$\vec{H}_0' = \vec{H}_0 - \vec{\omega/\gamma} . \qquad (3-13)$$

The magnetic moment μ precesses around the effective magnetic field, $\vec{H}_{eff} = \vec{H}_0' + \vec{H}_1$ with Larmor frequency $\omega_L' = \gamma H_{eff}$.

(Note that H_1 becomes a static magnetic field in the coordinate.)

The strength of H_{eff} is given by the following equation.

$$|H_{eff}| = \sqrt{H_1^2 + H_0'^2} = \sqrt{H_1^2 + (H_0 - \omega/\gamma)^2} \qquad (3-14)$$

The angle θ between the $\vec{H}_1$ and $\vec{H}_{eff}$ is written as

$$\theta = \tan^{-1}\left(\frac{H_0 - \omega/\gamma}{H_1}\right) \qquad (3-15)$$

This situation is seen in Fig. 20.

By scanning the rotating angular velocity ω from $\omega < \gamma H_0$ to $\omega > \gamma H_0$ through the resonance angular velocity $\omega_0 = \gamma H_0$ the direction of $\overrightarrow{H_{eff}}$ is changed from parallel to $\overrightarrow{H_0}$ to antiparallel to $\overrightarrow{H_0}$. If the change in rotation of the angular velocity of dH_{eff}/dt is sufficiently slower than $\omega_L{}'$, the magnetic moment μ follows the $\overrightarrow{H_{eff}}$. This phenomenon is the adiabatic fast passage (AFP). The change in rotation angular velocity of H_{eff} is estimated as $d\theta/dt$. Near the resonance angular velocity $\omega_0 = \gamma H_0$ the quantity $d\theta/dt$ is written as

$$\frac{d\theta}{dt} = \frac{d}{dt}\left(\frac{H_0 - \omega/\gamma}{H_1}\right)$$

$$= -\frac{1}{\gamma H_1} \cdot \frac{d\omega}{dt} \qquad (3-16)$$

and $\omega_L{}'$ is

$$\omega_L = \gamma H_{eff} = \gamma\sqrt{H_1{}^2 + (H_0 - \omega/\gamma)^2} \ . \qquad (3-17)$$

Then the condition of AFP $\omega_L{}' \gg d\theta/dt$ is rewritten in following equation.

$$-\frac{1}{\gamma H_1} \cdot \frac{d\omega}{dt} \ll \gamma\sqrt{H_1{}^2 + (H_0 - \omega/\gamma)} \ . \qquad (3-18)$$

Near the resonance angular velocity, H_0 is nearly equal to ω_0/γ. Then

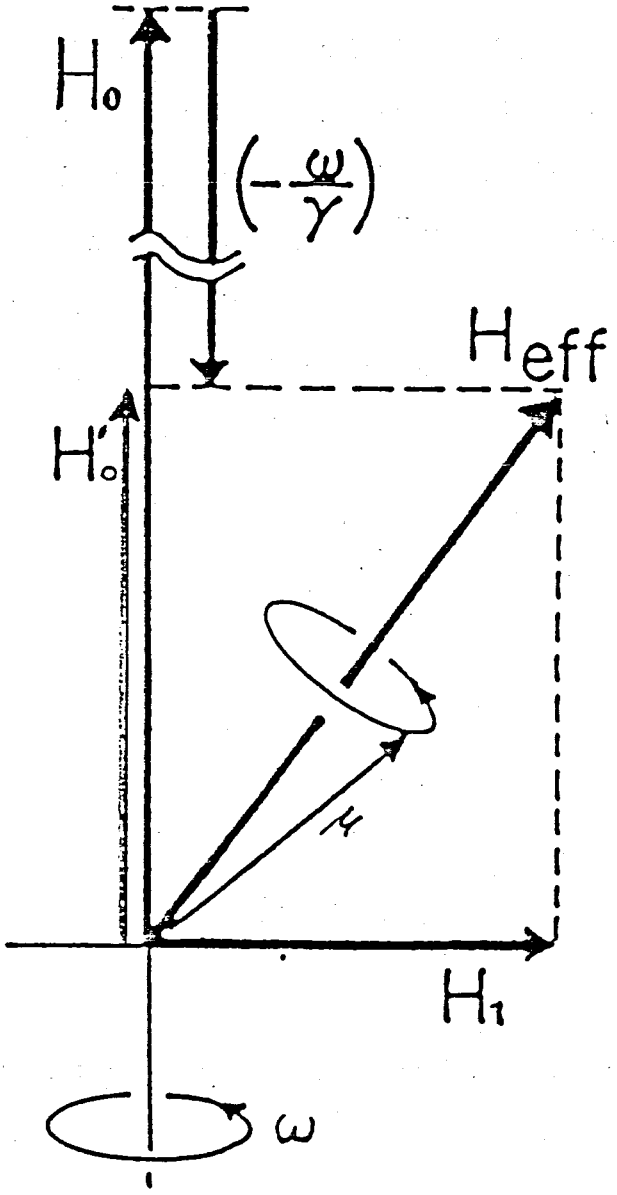

Fig.20 Schematic illustration of the relation of H_1, H_0,H_0' and H_{eff}.

the AFP condition is again rewritten as

$$-\frac{1}{\gamma H_1}\cdot\frac{d\omega}{dt} \ll \gamma H_1 \qquad (3-19)$$

or,

$$\frac{\Delta\omega}{\Delta t} \ll (\gamma H_1)^2 , \qquad (3-20)$$

where $\Delta\omega$ is the frequency modulation width of rf and Δt is the time period of the modulation. In the experiment, Δt is about 2.5 ms and $\Delta\omega$ is about 2πx20 kHz·rad. The gyromagnetic ratio γ of ^{12}B was determined as 765 Hz/Oe(Su 68). The strength of H_1 which is sufficient for the inversion of ^{12}B spin is defined as

$$H_1 \gg 1.5 \text{ Oe}. \qquad (3-21)$$

In addition to such condition as described above, H_1 has to be stronger than, or equal to the strength of dipolar field δ in the host material. In an fcc metal as platinum, δ is known to be about 2 Oe. Thus a necessary strength of H_1 is

$$H_1 > 2 \text{ Oe}. \qquad (3-22)$$

In the actual experiment the amplitude of H_1 is also modulated sinusoidally in the rf amplitude as a function of time as shown in Fig. 21 in order to start the θ value from near zero and to stop the θ value near π even with such a narrow frequency modulation of 20 kHz.

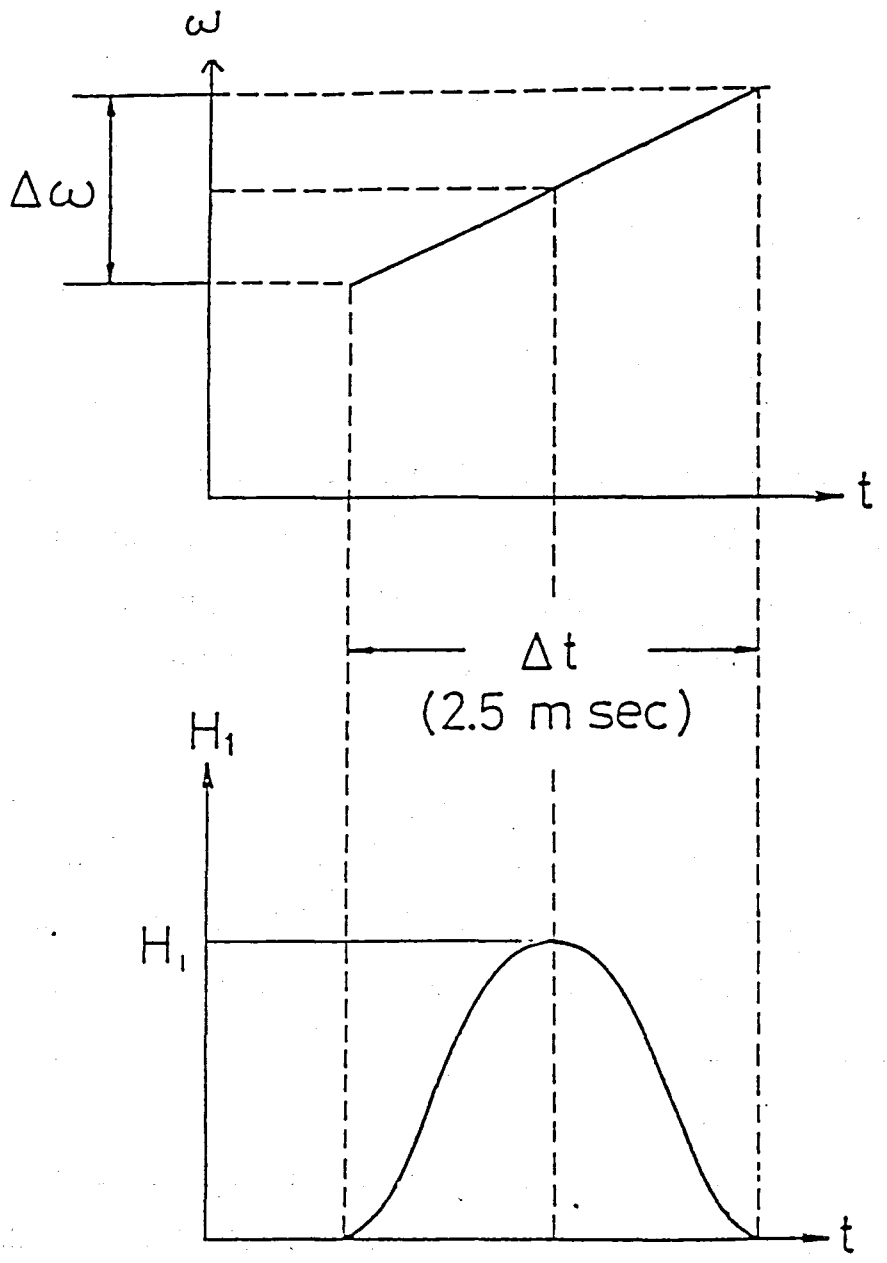

Fig.21 Sinusoidal modulation of the amplitude and the frequency of H_1 as a function of time.

3-1-e Polarization brought in the γ ray cascade and particle decay

There are four interactions which attenuate the primary polarization produced by the nuclear reaction. These are: (1) particle emission of excited nucleus such as $^{13}C \rightarrow p + ^{12}B$; (2) γ decay from the excited ^{12}B state to the ground state; (3) the hyperfine interaction between the nuclear spin and orbital electron in flight and (4) the spin lattice interaction of ^{12}B spin in Pt metal. Since the first two are rapid processes compared with β decay, the depolarization rates from these phenomena were estimated by utilizing the results from other experiments. The depolarization from (3) was, however, essentially removed by using the two stoppers of different thickness as mentioned in 3-1-c. The last depolarization effect was determined from our own check experiment and will be described in 3 - 3. The details of the estimation of depolarization from the first two processes are as follows.

(1) Particle emission

The particle emission processes reduce the magnitude of ^{12}B polarization. However the sign of the polarization is unchanged during the process. R.Ost et al. carried out a coincidence experiment between p and ^{12}B produced in ^{13}C induced reactions(Os 76). They showed that the contribution to the ^{12}B production from the sequential decay of ^{13}C was less than 20 %. Their experiment was done at a lower incident energy, about 7.5 MeV/u, and the quasi elastic collision was the dominant process. In the deep inelastic collision the contributions from such sequential processes are expected to become smaller than for the case of their experiment.

The upper limit of depolarization by this process is estimated to be less than 20 % of the initial value.

(2) γ decay

Only four excited levels of ^{12}B are stable against the particle decay

and the highest excitation energy of the levels is 3.31MeV. The energy range of 3MeV is small enough to assume that each level is populated with equal probability and equal polarization. The parity and the spin of each level were well known. The γ ray multipolarity, transition type and branching ratios were also well established (Ol 68, Ch 68). The level scheme of ^{12}B is shown in Fig. 22.

The depolarization by γ decay is then calculated as follows.

The level population following the γ decay to a level with spin J_f is related to the initial population as

$$a(m_f) = \sum_{m_i=-J_i}^{J_i} |\langle J_f\, m_f\, \lambda\, m_i - m_f \,|\, J_i\, m_i\rangle|^2 Q(m_i) \quad , \qquad (3-23)$$

where λ is the multipolarity of the γ decay and the suffix i and the suffix f mean the quantities of the initial and the final levels, respectively. By using the equation, the polarization of the final level is calculated from the initial polarization. The depolarization rate, R_{dep}, is calculated as

R_{dep} = P(final state)/P(initial state)

$$= (-1)^{\lambda - Ji - Jf + 1}\, W(\, J_i\ J_i\ J_f\ J_f\ ;\ 1\ \lambda\,) \sqrt{\frac{J_i(2J_i+1)(J_f+1)(2J_f+1)}{(J_i+1)J_f}} \quad , \qquad (3-24)$$

where $W(\, J_i\ J_i\ J_f\ J_f\ ;\ 1\ \lambda\,)$ is a Racah coefficient. The coefficient is calculated by using J_i, J_f and λ and the final form of the depolarization coefficient is

$$R_{dep} = \frac{1}{2} \cdot \frac{J_i(J_i+1) + J_f(J_f+1) - \lambda(\lambda+1)}{(J_i+1)J_f} \qquad (3-25)$$

The numerical values of R_{dep} are shown in Table 2 for the ^{12}B case. The

total depolarization rate is estimated to be about 75 % of the initial value under the assumption of equal population and equal polarization.

Note that the total depolarization rate is estimated to be 89 % under the assumption of equal polarization and weighted population which is proportional to $(2J_i + 1)$.

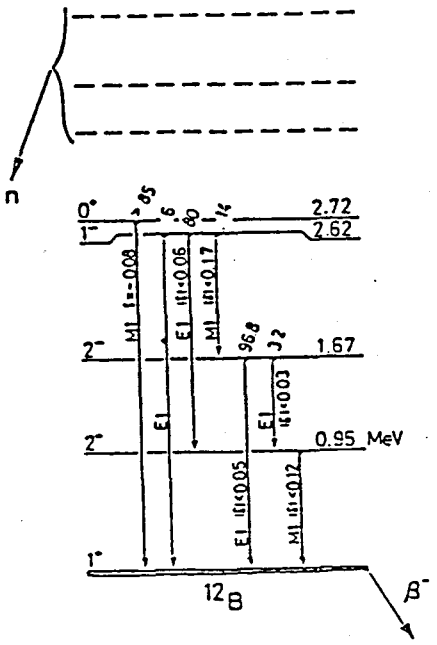

Fig.22 Level scheme of ^{12}B.

Transition	Transition Type	R_{dep}
$0^+ \rightarrow 1^+$	M1	0
$1^- \rightarrow 1^+$	E1	0.5
$\rightarrow 2^+$	E1	0.75
$\rightarrow 2^-$	M1	0.75
$2^- \rightarrow 1^+$	E1	1
$\rightarrow 2^+$	E1	0.825
$2^+ \rightarrow 1^+$	M1	1

Table. 2

Reduction rate of ^{12}B polarization by a γ ray cascade

3-2 Details of the experiment

3-2-a Reaction chamber and the production of ^{12}B

The reaction chamber used in the experiment is shown in Fig. 23. The main design feature was to obtain a large solid angle for the collection of ^{12}B and a wide selection range of scattering angle. The reaction chamber was built of plastic in order to avoid production of long lived background activities. The chamber consisted of three parts, i.e., target chamber, absorber chamber and stopper chamber. In the target chamber, the β emitter ^{12}B produced by the nuclear reaction was collimated into the scattering angle θ_L and was led to the absorber chamber in which the energy absorber, an aluminium foil with suitable thickness, was placed. After passing through the absorber, ^{12}B was implanted in the platinum stopper foil which was placed in stopper chamber. The thickness of the absorber foil and the stopper foil was remote-controlled from the measurement room. The solid angle of ^{12}B collection was about 32 msr. The measurable scattering angle varied from 6 deg. to 60 deg.

The stopper chamber and apparatus around the stopper chamber were constructed for efficient detection of β rays. As mentioned above, the stopper chamber was made of plastic material(Nylon). This was also necessary for reducing the back scattering of β rays at the chamber wall. Due to the same reason, several features were incorporated: A pair of rf coils for NMR was mounted outside the stopper chamber as shown in Fig. 24. This was

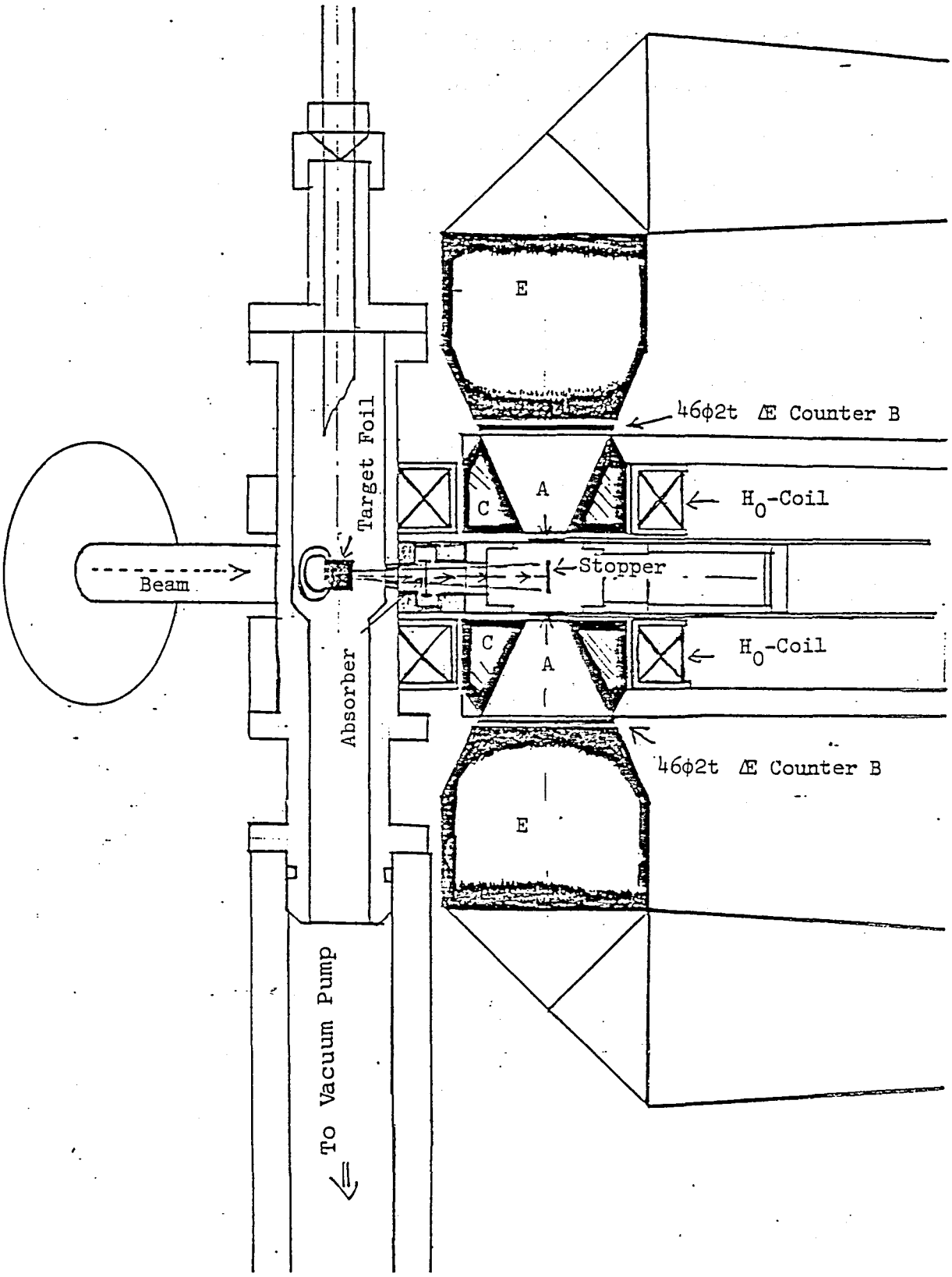

Fig 23 Reaction chamber used for the present study.

necessary to eliminate heavy elements in the stopper chamber except for the stopper foil itself. Also the static magnetic field was applied by an air core magnet of Helmholtz type. Back scattering of β rays at iron pole face for a steel magnet would have been saved.

The beam line arrangement of Course-D and Course-K in RCNP are shown in Fig. 25. The experiments were carried out at these two courses. A ^{14}N beam accelerated by the 230 cm AVF cyclotron at RCNP was focused on the target with size about 3 mm dia. A typical beam intensity of ^{14}N ions was about 100pnA. Energies of the beam were 210 MeV for $^{14}N^{+5}$ ions and 130 MeV for $^{14}N^{+4}$ ions. The targets were self-supporting metalic foils of about 10 mg/cm^2 thickness. Energy loss of the incident ^{14}N ion in the target foil was about 20MeV. The effective incident energy was defined as the energy at the half target thickness and calculated by using the range-energy relations. The beam passing through the target was stopped in the target chamber.

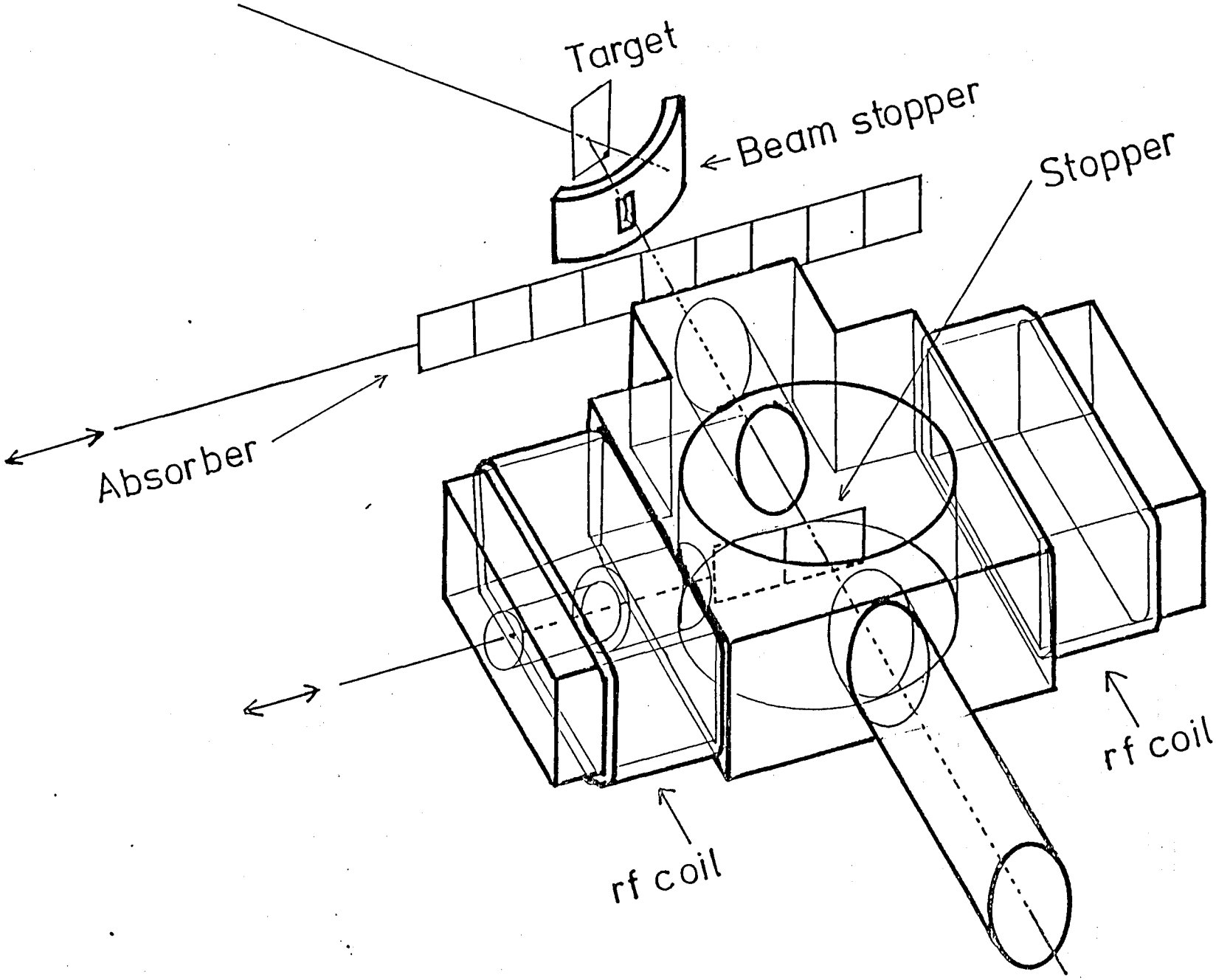

Fig 24 A pair of rf coils mounted outside the stopper chamber.

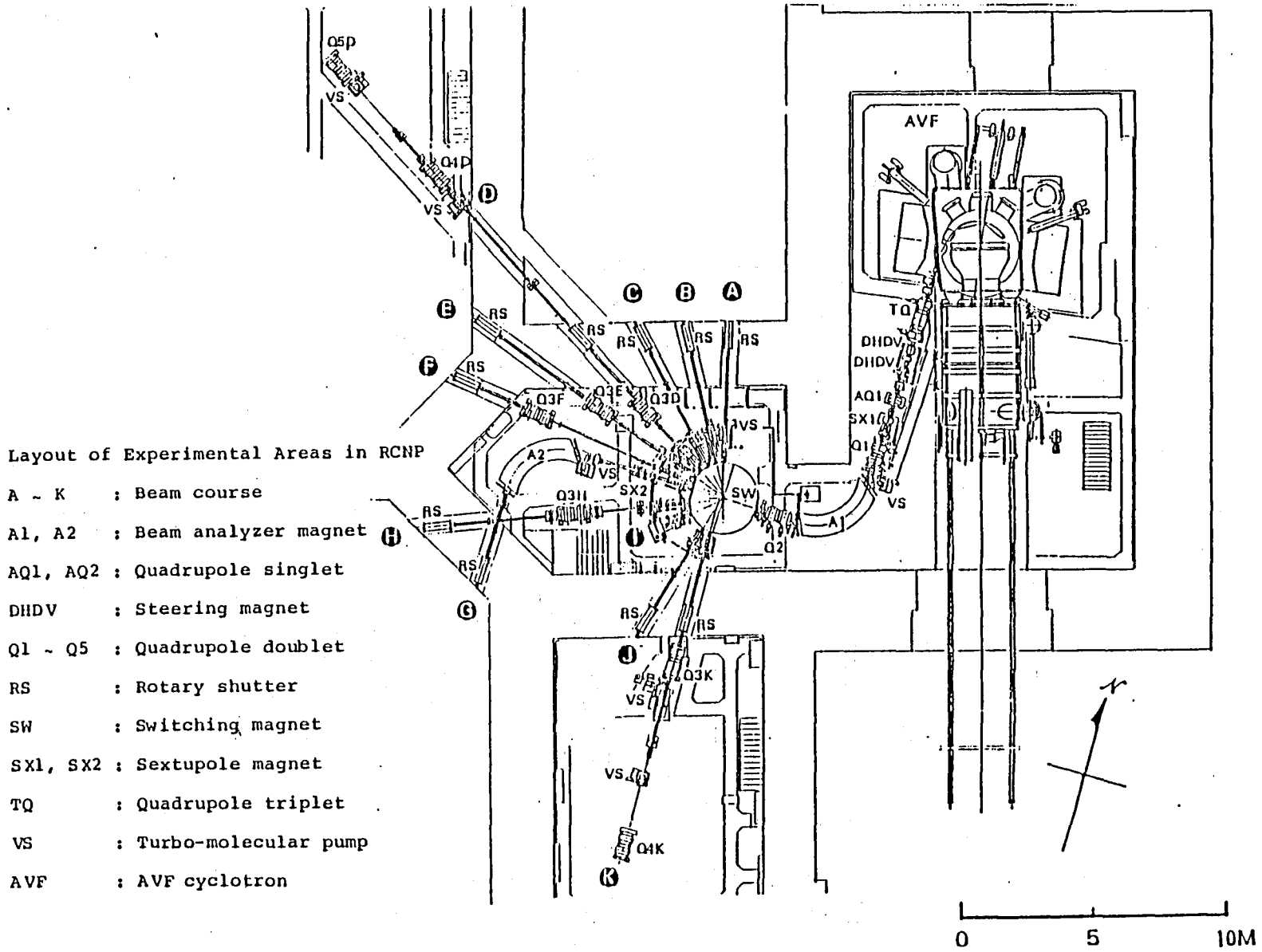

Fig. 25 The beam lines of course-D and course-K at RCNP

3-2-b β ray detection

Two sets of plastic scintillator counter telescopes were placed above and below the stopper foil perpendicular to the reaction plane in order to detect the β rays emitted from the ^{12}B in the stopper foil. A counter telescope consisted of three coincidence counters. There were two minimum ionizing ΔE counters, A and B and one energy counter E. One anti-coincidence cone shaped counter, C, was also placed in between A and B as shown in Fig. 20. The dimensions of the two ΔE counters were 12mm in diameter 1mm thick and 46mm in diameter 2mm thick, respectively. The solid angle subtended by the telescope was defined by these two counters and partly by C counter. The energy loss of a β ray in the ΔE counter was about 200 keV for A counter and was 400 keV for B counter. The deflection of the path of β ray in the counter by the multiple scattering was negligibly small, i.e., less than 5 deg. The energy resolution of E counter was about 15 %. The material of counters was the plastic scintillator of high energy grade made by C-I Kogyo Co., Japan. The light signals in each scintillator was transmitted a photomultiplier by means of a lucite light guide. The photomultipliers were R329-02 for B, C and E counters and R647-09 for A counter, manufactured by Hamamatsu T-V Inc. Japan.

A schematic diagram of the β ray counting electronics is shown in Fig. 26. The output signal from A counter was amplified by a fast amplifier and was fed to a fast leading-edge discriminator. The output signal from B counter was immediately fed to a fast leading-edge discriminator. NIM fast logic signals of 10ns wide were obtained by discriminating the output signals from A and B counters. The threshold level for the signals from A and B counters was chosen slightly below the signal of the minimum ionization energy. The output signal from C counter was immediately fed to a fast

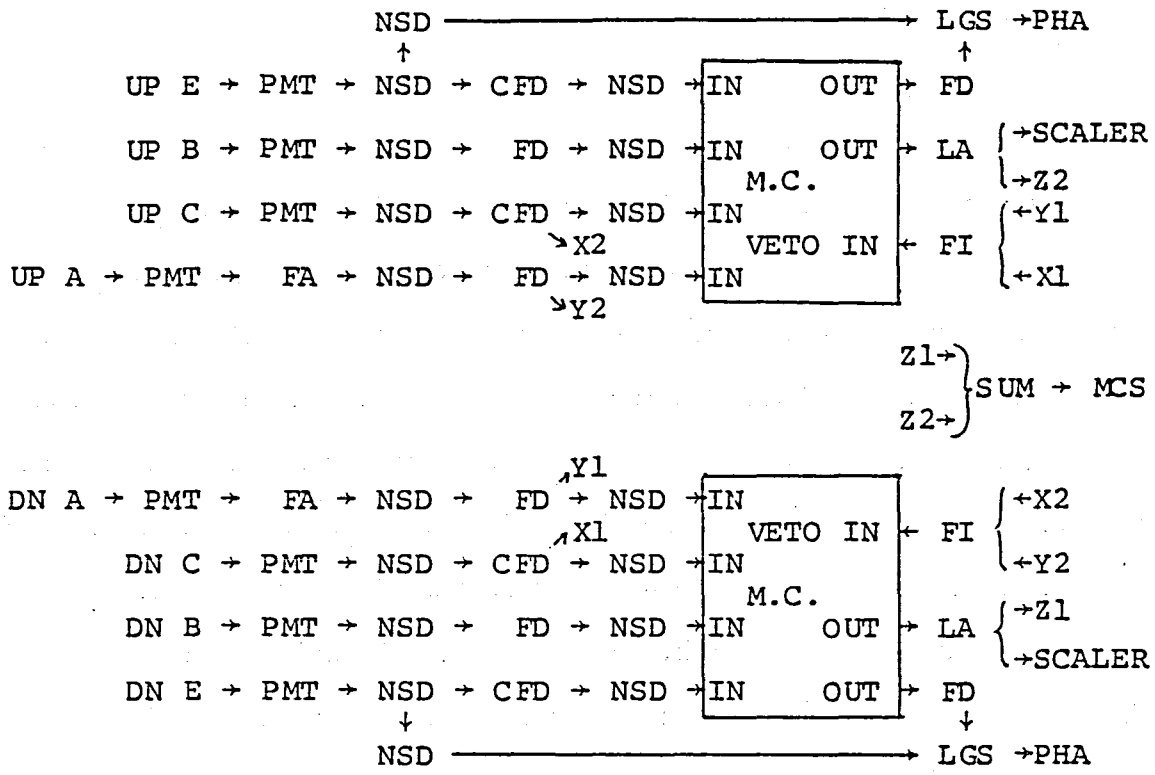

PMT : Photo Multiplier + Breeder

NSD : Nano Second Delay

CFD : Constant Fraction Discriminator

FD : Fast Discriminator

M.C.: Majority Coincidence; Majority = 4

FA : Fast Amplifier

LGS : Linear Gate Stretcher

LA : NIM to TTL Level Adapter

FI : Logic Fan In

SUM : Sum Amplifier

Fig.26 Electronics circuit for the β ray measurement.

constant-fraction discriminator to obtain a NIM fast logic signal of 20 ns wide. The threshold level for this was selected slightly above the photomultiplier-noise level.

The output signal from E counter was divided into two parts. One was immediately fed to a fast constant-fraction discriminator and NIM fast logic signal of 10ns wide was obtained. The threshold level for the E counter was set at 3 MeV. Another was shaped and gated by a fast linear-gate stretcher. The gating logic was an ($A \cap B \cap \bar{C} \cap E$) signal. The stretched and gated linear signal was fed to a PHA for β ray energy analysis.

True β ray events were defined as ($A \cap B \cap \bar{C} \cap E$) by using a majority coincidence unit. The time resolution was 20 ns. The output logic signal was fed to a fast linear-gate stretcher as a gating signal as described above. The same signal was also converted to NIM slow logic by level adapter and was fed to two scalers which count the number of events following the inversion of ^{12}B polarization and events following without an inversion respectively. A time spectrum was obtained by counting the summed events of up and down telescopes.

A typical maximum single counting rate was about 100kc/sec for C counter and 10kc/sec for B counter and 1kc/sec for A and E counters. The time resolution of 20ns was short enough to reject the accidental coincidence events.

Anti-coincidence signals were also obtained from A and C counters of the other counter telescope located at the opposite side with respect to the stopper foil in order to reject the event which penetrated the up and the down counter telescopes simultaneously, for example, a cosmic ray. A typical true count rate was about 10 c/sec.

3-2-c NMR

A wide band rf amplifier with 400W output was constructed in order to produce an rf magnetic field, strong enough to induce the AFP. A 5F20RA vacuum tube was used for the final output stage of the rf amplifier as shown in Fig. 27. The rf electric power produced by the amplifier was induced into a rf coil and produced the rf magnetic field in the coil.

An rf coil was also constructed for the present experiment. The inductance of the coil was about 250μH. The strength of the external static magnetic field used was 221 Oe and the resonance frequency of ^{12}B in this field was about 169kHz. The impedance of the coil at this frequency was about 275 ohm. The strength of rotating magnetic field produced by the coil was estimated by using V_{pp}, the peak to peak voltage between the both end of rf coil, as follows.

$$H_1=(V_{pp}/4)/275 \times S, \qquad (3-26)$$

where S is the strength of static magnetic field produced in the coil when a DC current of 1A is supplied. At the size of this coil, S was about 5 Oe. The necessary strength of H_1 or V_{pp} was determined by a check experiment. Details of this check experiment will be described in section 3-3.

The frequency and amplitude of the rf were modulated for AFP. Frequency modulation was done by using a voltage-controlled frequency (VCF) of a function generator (FG). At the beginning of a spin control period a ramp voltage was initiated. This signal was mixed with an output of a 1bit digital to analog converter (DAC), which converts a 1bit control logic signal to two different analog voltages in alternative beam-count cycle as shown in Fig. 28. The mixed signal was fed to a VCF input of a FG. A resultant rf for spin control was generated with an on-resonance frequency range of 160 kHz —> 178 kHz and with an off-resonance frequency range of 260 kHz —> 278

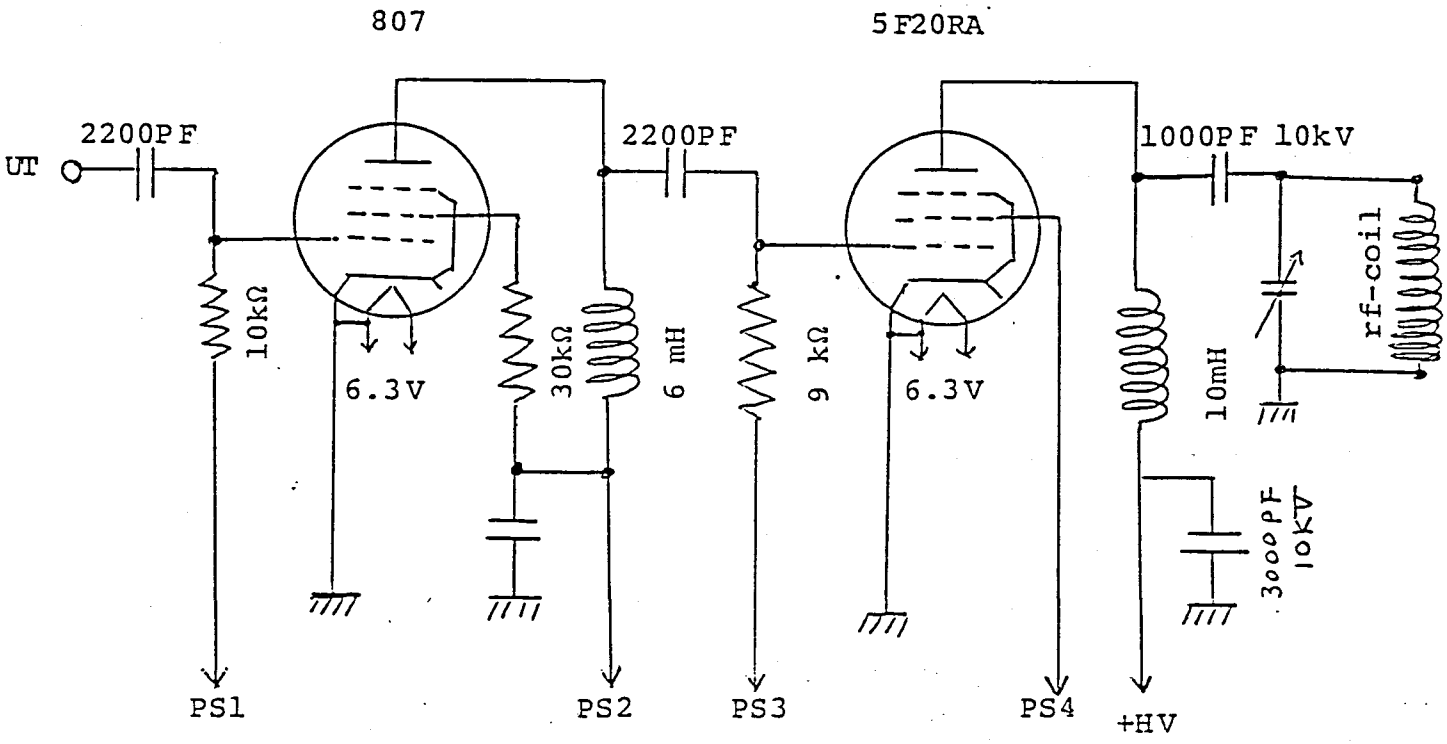

PS1	-30V∽-90V	Constant Voltage Bias Supply
PS2	+300V	Constant Voltage Power Supply
PS3	-50V∽-120V	Constant Voltage Bias Supply
PS4	+400V	Constant Voltage Power Supply
+HV	+2000V	Constant Voltage Power Supply

Fig.27 Circuit of rf amplifier with 400 W output.

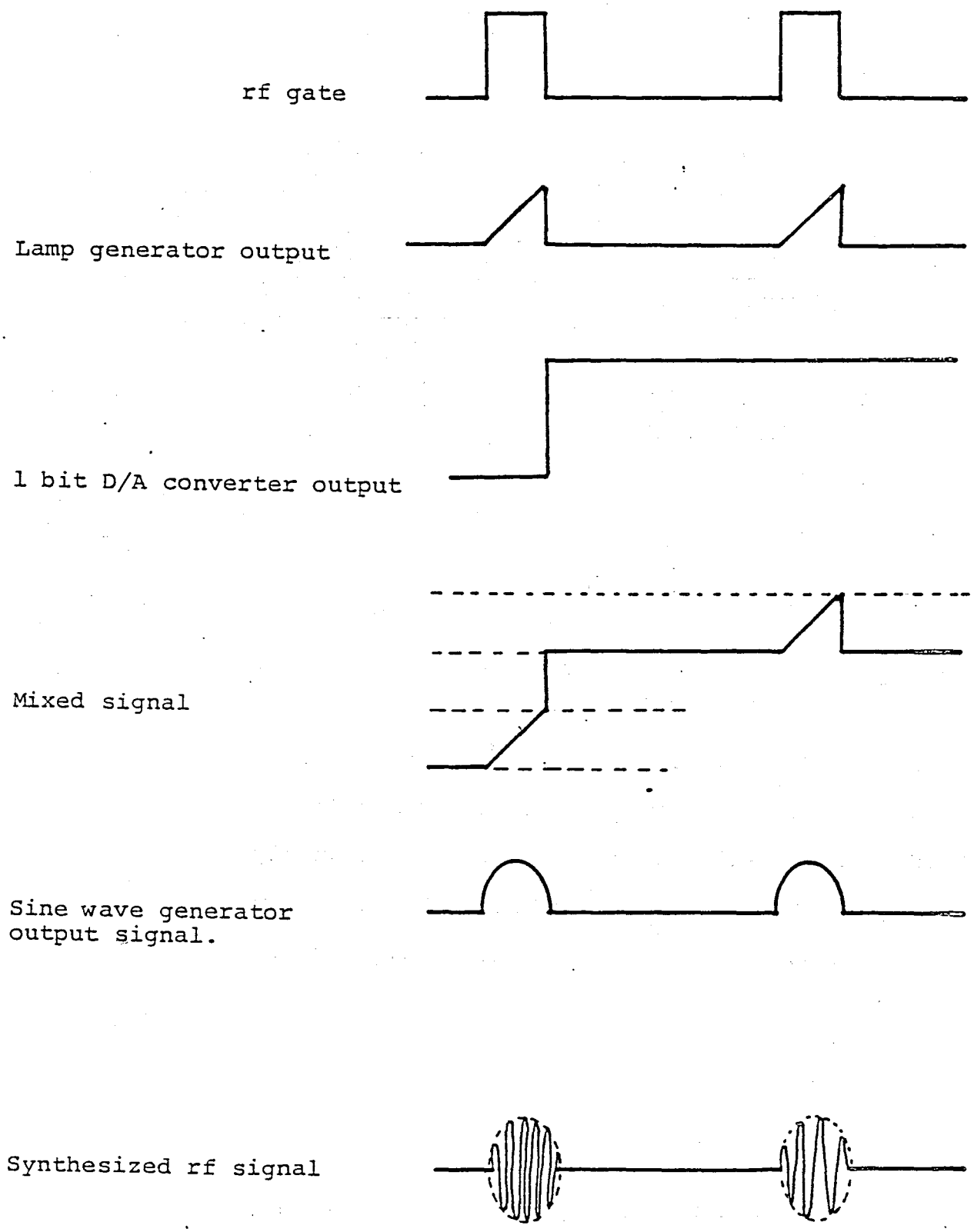

Fig.28 Synthesized rf for AFP with amplitude and frequency modulations.

kHz. This rf was also sinusoidally modulated in its amplitude as a function of time. A sine-wave generator (SG) was triggered at the beginning of the spin control period and an output signal of a SG was fed to an amplitude modulator (AMG) in order to modulate the rf in the amplitude. The modulated rf for both frequency and amplitude was fed to an rf-gate which opened in the spin control period only and the gated rf was fed to a power amplifier. A block diagram of the rf system is shown in Fig. 29. Control logics for the rf were generated by a micro computer (See following section).

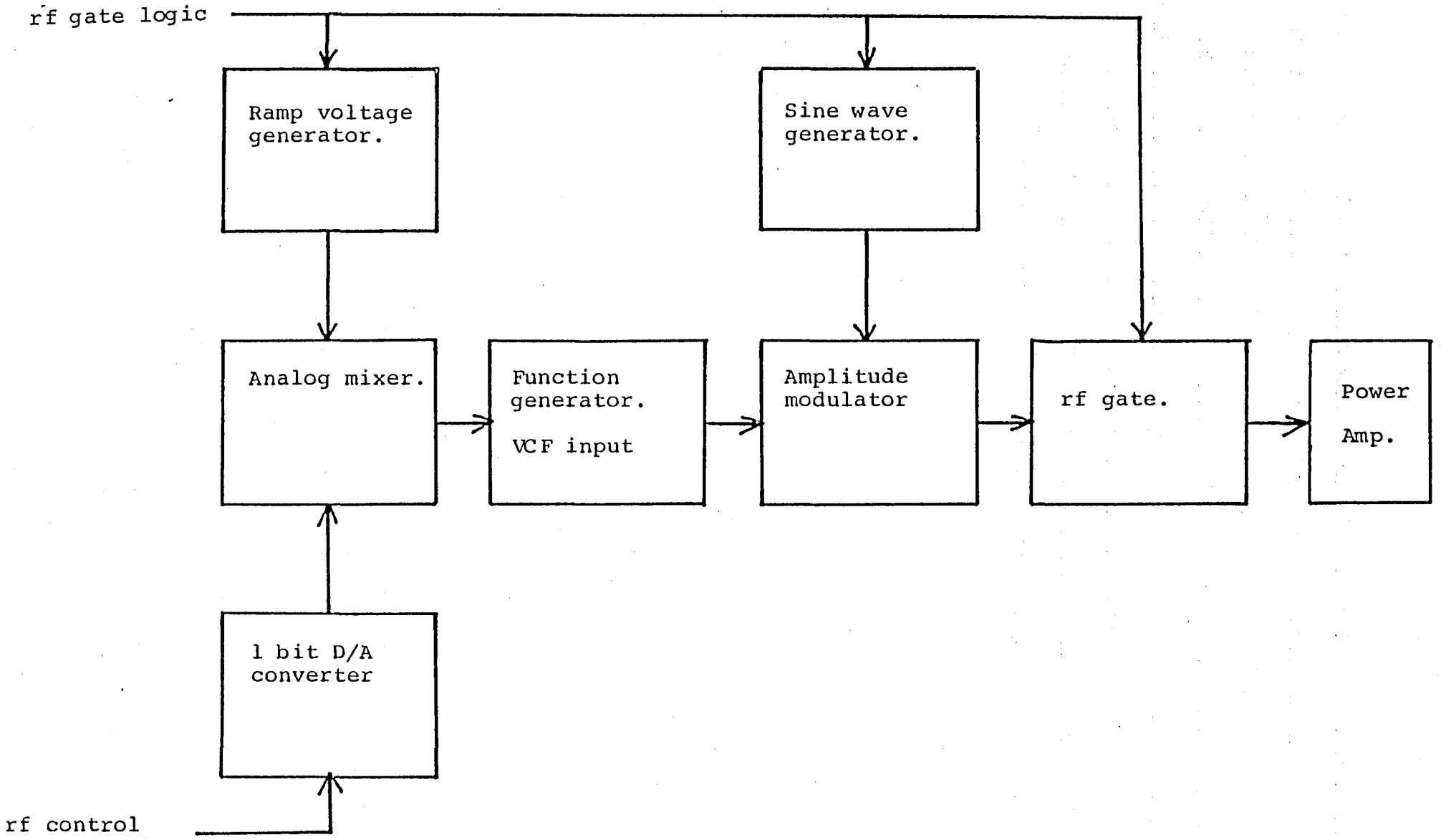

Fig.29 Block diagram of rf control system.

3-2-d Timing control

The time flow chart of the actual experiment, the data taking, spin control and beam irradiation is schematically shown in Fig. 30. One beam count cycle was 64 ms. During the first 29ms a target was bombarded by ^{14}N ions. The following 35 ms without beam was used for β-ray counting and polarization inversion. Spin was inverted by an rf applied during 2.5 ms following right after the end of the beam cycle. Another rf was also applied for 2.5 ms at the end of the beam-off time to restore the spin direction back. In the following beam-count cycle, ^{12}B spin polarization was not inverted, i.e., an rf was applied on off-resonance frequency. A pair of resonance-on and resonance-off period was alternatively repeated. For the beam pulsing Dee voltage of the AVF cyclotron was modulated in the 30 % from a normal acceleration voltage.

The sequence described above was controlled by a micro computer which generated parallel-4-bit-patterns with TTL level as a function of time as shown in Fig. 31. The first bit was used for the beam pulsing. The beam bombardment was done in the period of logic-level 1. The second bit was used for the bin-gate signal. The β-ray counting electronics operated in the period of logic-level 1. The third bit was used for the rf control. A ramp generator and a sine-wave generator were initiated by the positive edge of this logic and a rf-gate opened during logic-level 1 of this bit. The fourth bit changed its level in an alternate beam-count cycle and was fed to a 1 bit DAC in order to shift the initial voltage for the VCF in every other beam-count cycle.

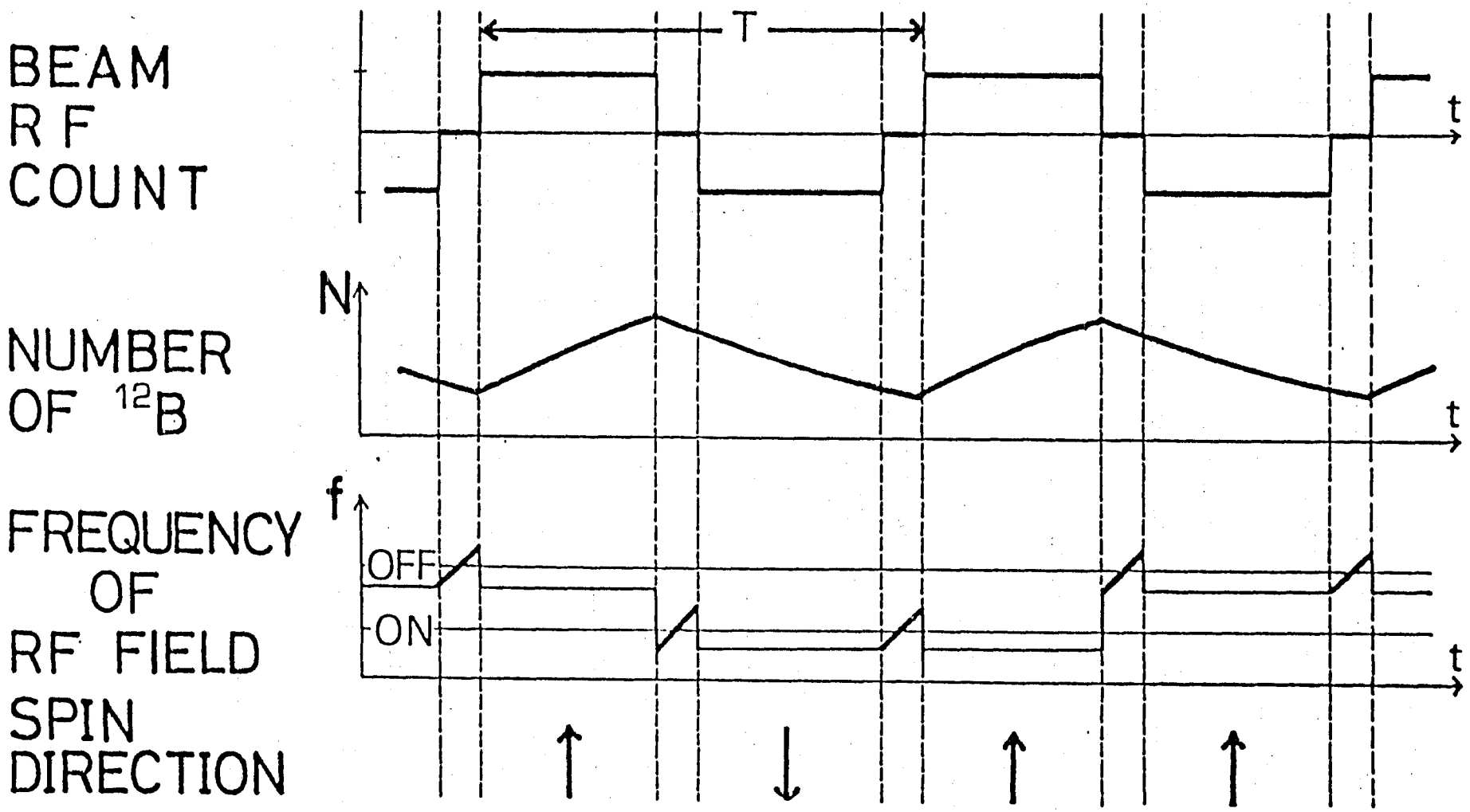

Fig.30 The time flow chart of the experiment.

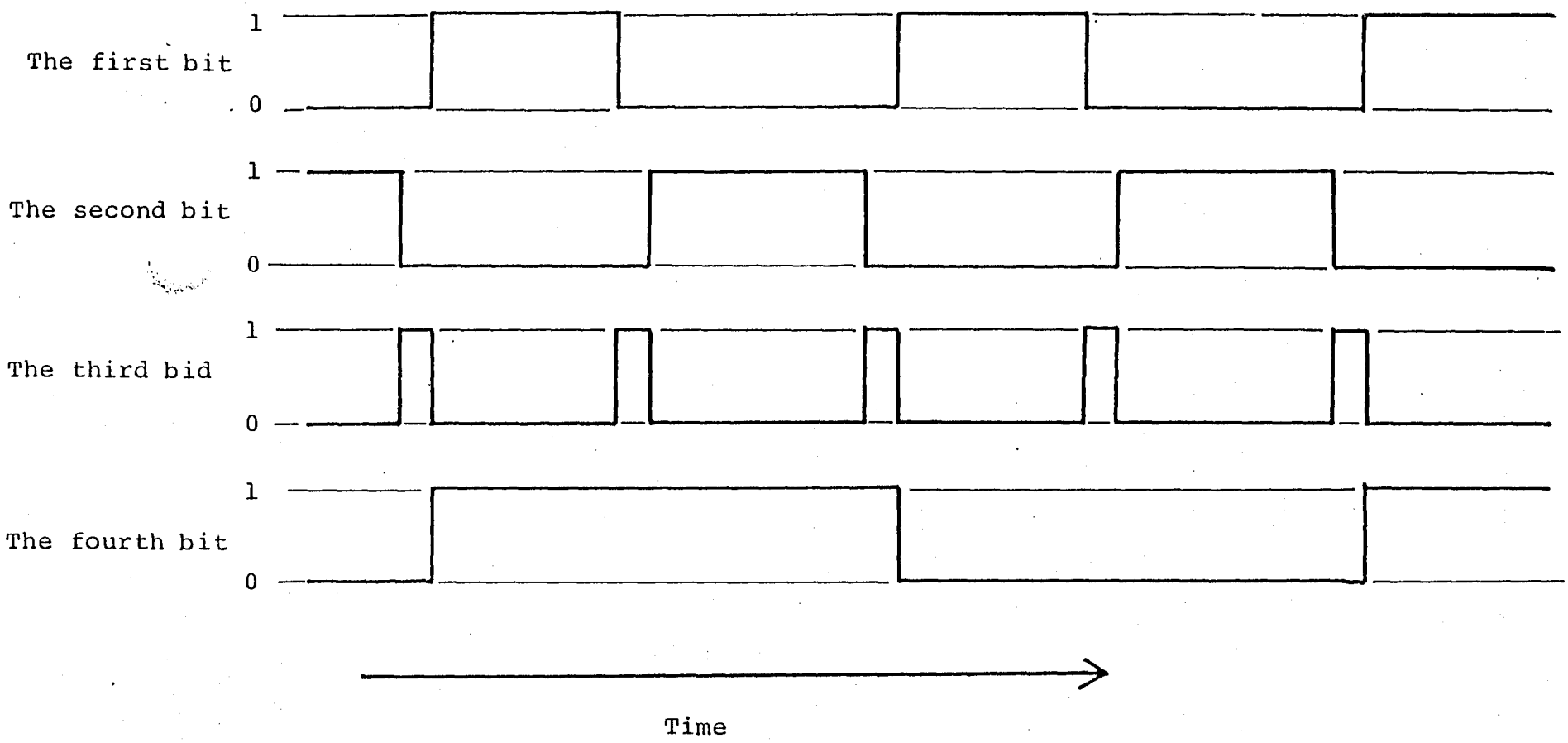

Fig.31 Parallel 4 bit pattern for controling the measurement system.

3-3 Check experiment by use of the (d,p) reaction.

A typical counting rate in the present experiment at RCNP was about 10 c/s as described in 3-2-b. It was impossible or inefficient to check the measurement system by using the beam from the AVF cyclotron. The total system for ^{12}B polarization measurement was tested by using polarized ^{12}B produced in the $^{11}B(d,p)^{12}B$ reaction (Su 68) at Osaka University, Laboratory of Nuclear Studies. The incident deuteron energy was 1.5 MeV and was obtained by the 4.75 MV Van de Graff accelerator. The conditions of the check experiment are summarized in Table 3. The aims of the check experiment were as follows.

(1) Determination of the strength of the external static magnetic field necessary.

The asymmetry change R of β decay was measured as a function of H_0 as shown in Fig. 32-a. The asymmetry of β rays increased with proportion to the strength of H_0 and saturated with $H_0 > 150$ Oe. Thus a practical H_0 was chosen to be 221 Oe. This field strength was produced by a coil current of 4.00 A.

(2) Nuclear Magnetic Resonance

The H_0 was set at 221 Oe. The asymmetry change R of β decay was measured as a function of H_1 frequency by applying AFP for the confirmation of the spin control by means of NMR. The resonance frequency was found to be 169 kHz which is shown in Fig. 32-c and agrees with the known value (Su 68). The line width of the resonance measured was consistent with the rf modulation width superimposed on a field inhomogeneity of 2 %.

Conditions of Check Experiment	
Nuclear Reaction	$^{11}B(d,p)^{12}B$
Incident Energy	1.5 MeV
Target	Natural Boron 100μg/cm^2 Tantal Backing
Scattering Angle	45°
Typical Counting Rate of β rays	1000 cps
Beam Intensity	10 μA

Table 3 Conditions of the check experiment.

(3) ^{12}B polarization as a function of H_1 strength

The asymmetry change R of β decay was measured as a function of peak to peak rf voltage applied on the rf coil in order to fix the rf intensity necessary for AFP. The result is shown in Fig.32-b. The peak to peak rf voltage of 600V was found sufficient to invert the ^{12}B polarization by means of AFP. This V_{pp} value corresponded to an H_1 strength of about 2.5 Oe.

(4) Spin lattice relaxation time of ^{12}B polarization in Pt metal

The spin lattice relaxation time T_1 of ^{12}B in Pt metal was measured under the conditions of H_0=221 Oe and H_1= 9 Oe which were used in experiments at RCNP. The polarization of ^{12}B was measured as a function of time and the relaxation time of 300ms was observed. This value is consistent with the previous results (Su 68). The relation between the initial polarization and the measured polarization was calculated by using this T_1 with

$$P_f = P_i \cdot \frac{\int_0^{29} e^{-t/T_1}\,dt \int_{31.5}^{61.5} e^{-t/T_1}\,dt}{\int_0^{29} dt \int_{31.5}^{61.5} dt} \qquad (3\text{-}27)$$

$$= 0.9\, P_i$$

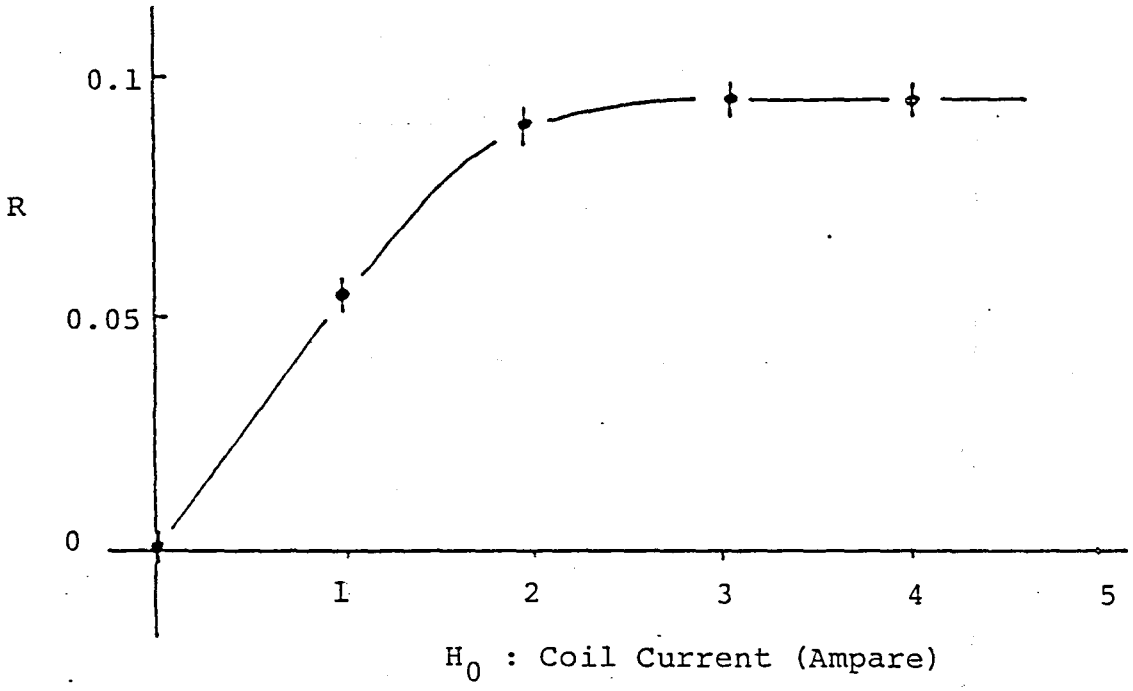

Fig.32-a β ray asymmetry R as a function of strength of H_0.

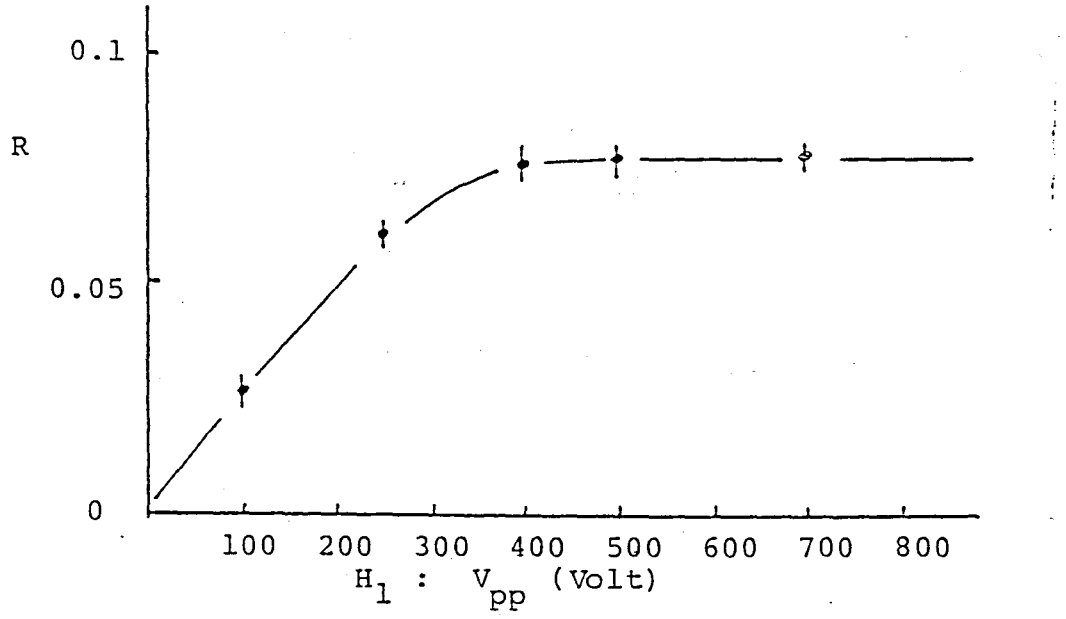

Fig.32-b β ray asymmetry R as a function of strength of H_1.

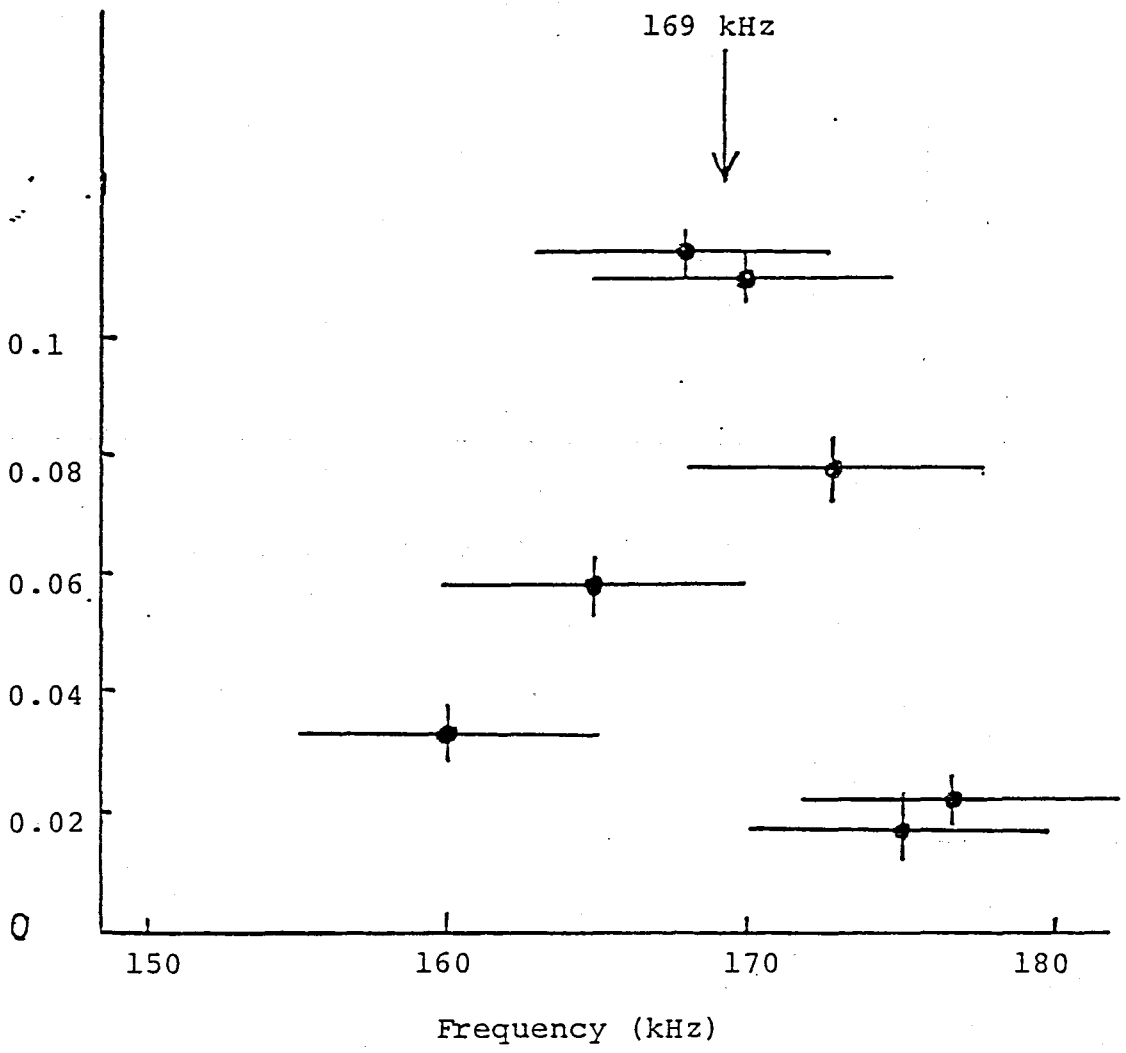

Fig.32-c β ray asymmetry R as a function of the frequency of H_1.

3-4 Time and energy spectra of β rays

The reaction products ^{12}B were identified by their β decay end point energy of 13.37MeV and half life of 20.3ms as described in 3-1-a. A typical energy spectrum and a time spectrum of the β rays are shown in Fig. 33. The intensity of the long-lived background and short lived component as well as lifetime were yielded by fitting the following two component expression to the time spectrum.

$$Y = A\exp(-t/\tau) + B \qquad (3\text{-}28)$$

A χ^2 diagram is shown in Fig. 34. The β decay half life obtained was $\tau = 20 \pm 2$ ms which is consistent with the known half life of ^{12}B. The contaminating long-lived component was found to be less than 10 % of total β-ray counts.

The energy spectrum of β rays also indicated a reasonable end point β ray energy from ^{12}B.

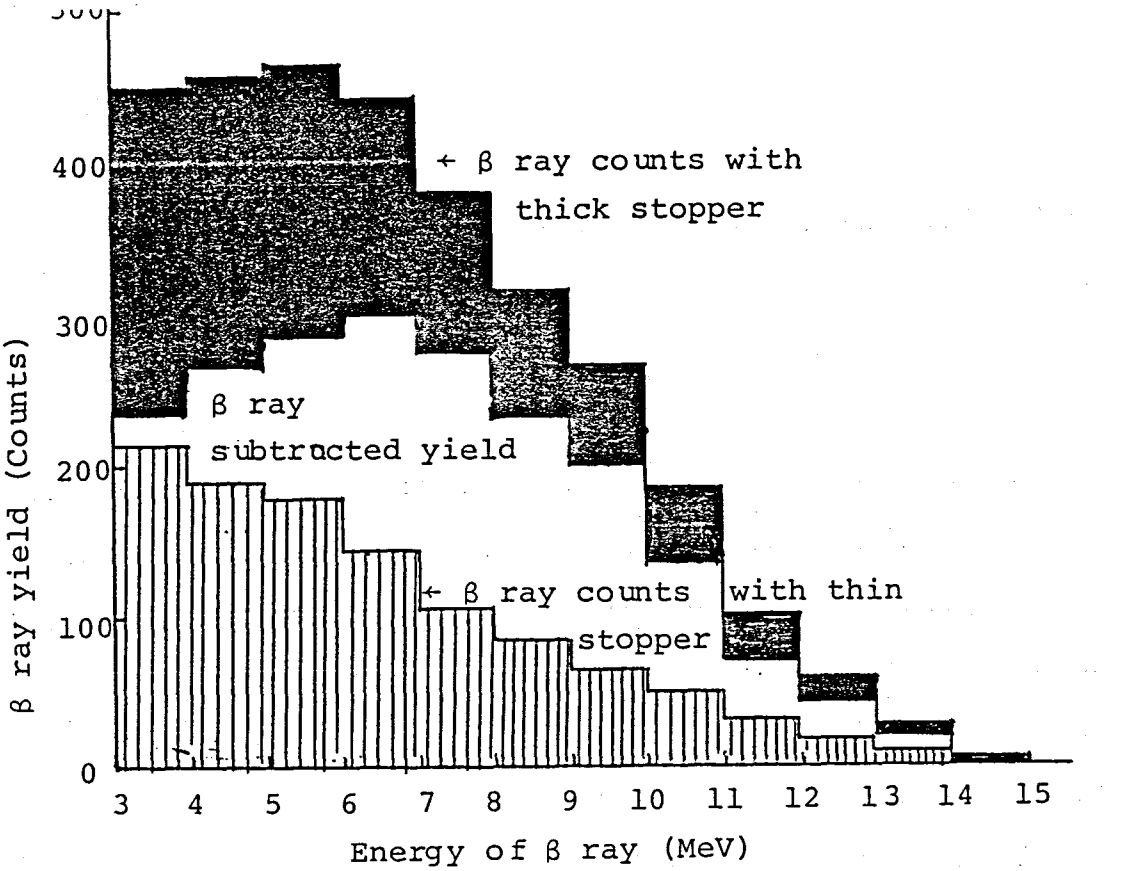

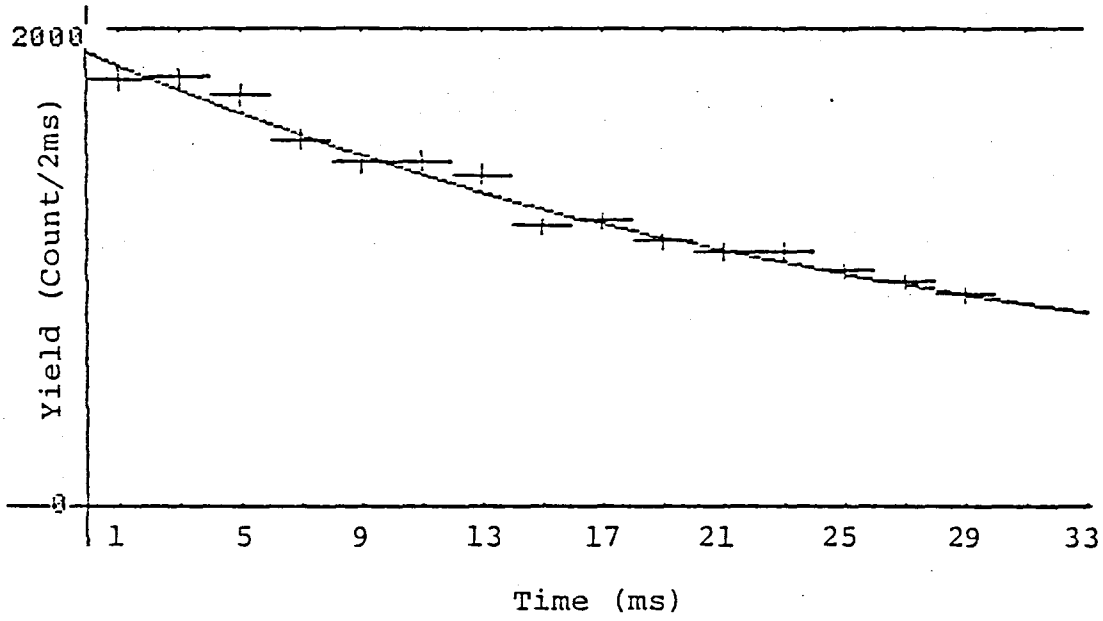

Time Spectrum

Fig.33 Typical energy spectrum and time spectrum of β rays.

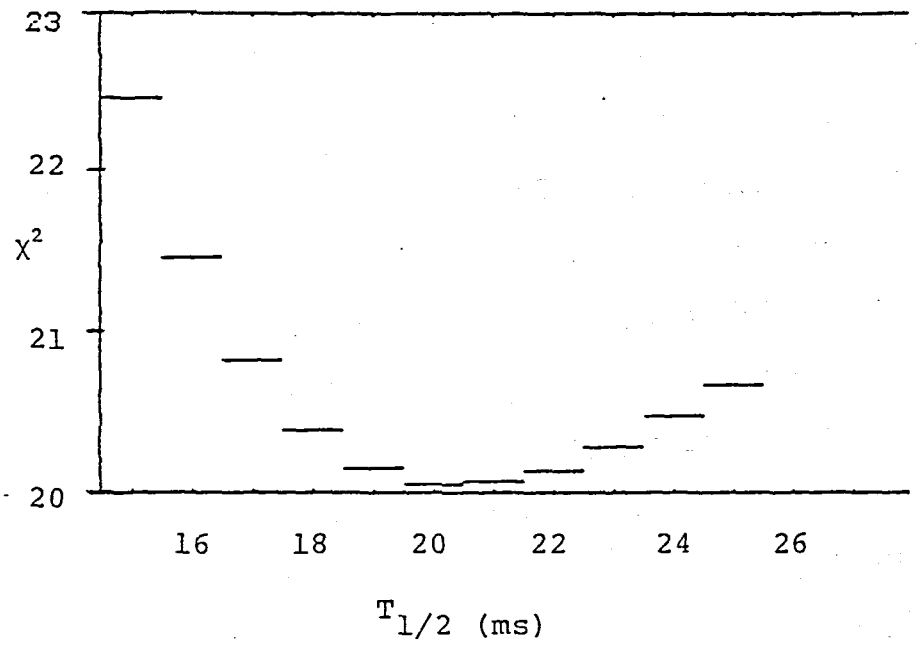

Fig.34 χ^2 distribution of a two component fit of time spectrum of the β rays indicated as a function of half life of the β rays.

3-5 Summary of the polarization measurement

The reduction factors R_{dep} = P(final)/P(initial) of the ^{12}B polarization are summarized as follows.

(1) Particle decay about 80 %

(2) γ decay about 75 %

(3) Spin lattice interaction about 90 %

In addition to these reduction factors, the reduction from the β ray contributing from ^{13}B is estimated to be about 80 %, as described in 3-1-a.

From the product of each reduction factor, the total depolarization rate is found approximately to be 0.4.

P(observed) = 0.4 · P(produced by the nuclear reaction) (3-29)

That is, the primary polarization produced in the nuclear reaction is about 2.5 times larger than the observed polarization. The experimental results are not corrected for these effects.

(Note that the reduction factor from ^{13}B contamination becomes about o.65 in ^{232}Th target and the total depolarization rate is estimated to be about 0.35 because of an exceptionally large contamination.)

CHAPTER 4

Results and discussion

4-1 Experimental results

4-1-a Target mass dependence

4-1-b Scattering angle dependence

4-1-c Incident energy dependence

4-1-d Summary of the experimental results

4-2 Discussion

4-2-a Analysis by use of frictional model

4-2-b Coexistence of the different reaction mechanisms

4-2-c Comparison with other experimental results

4-1 Experimental results

Spin polarization of ^{12}B produced in the reaction $^{100}Mo(^{14}N,^{12}B)$ was measured in our work prior to 1978 and the results are shown in Fig. 35 (Su 77, Ta 78). The polarization was large with the negative sign in the region of small kinetic energy loss, became positive or zero with increase of the kinetic energy loss and was again negative in the region of large kinetic energy loss. This dependence of the polarization on the reaction Q-value was almost the same for the other reactions studied here with ^{232}Th, ^{nat}Cu and ^{nat}Fe targets but the reaction Q-value at zero crossing of the polarization changed as a function of the target mass A, scattering angle and incident energy. The change of the zero crossing of the polarization is understood in the framework of the friction model and direct two proton transfer.

A different dependence of polarization on the reaction Q-value was found in the reaction with a light target (Ta 80, Mi 81). Here the polarization in the region of small kinetic energy loss was positive and the gross behaviour of the polarization was explained solely by the friction model for the ^{27}Al target. With the ^{45}Sc target, polarization in the region of small kinetic energy loss was almost equal to zero. This change of polarization indicates coexistence of the two proton transfer process and the frictional process in the region of small kinetic energy loss (Ta 81).

The experimental conditions for the reactions presently studied, i.e., target nucleus, scattering angle and incident energy, are summarized in Table 4.

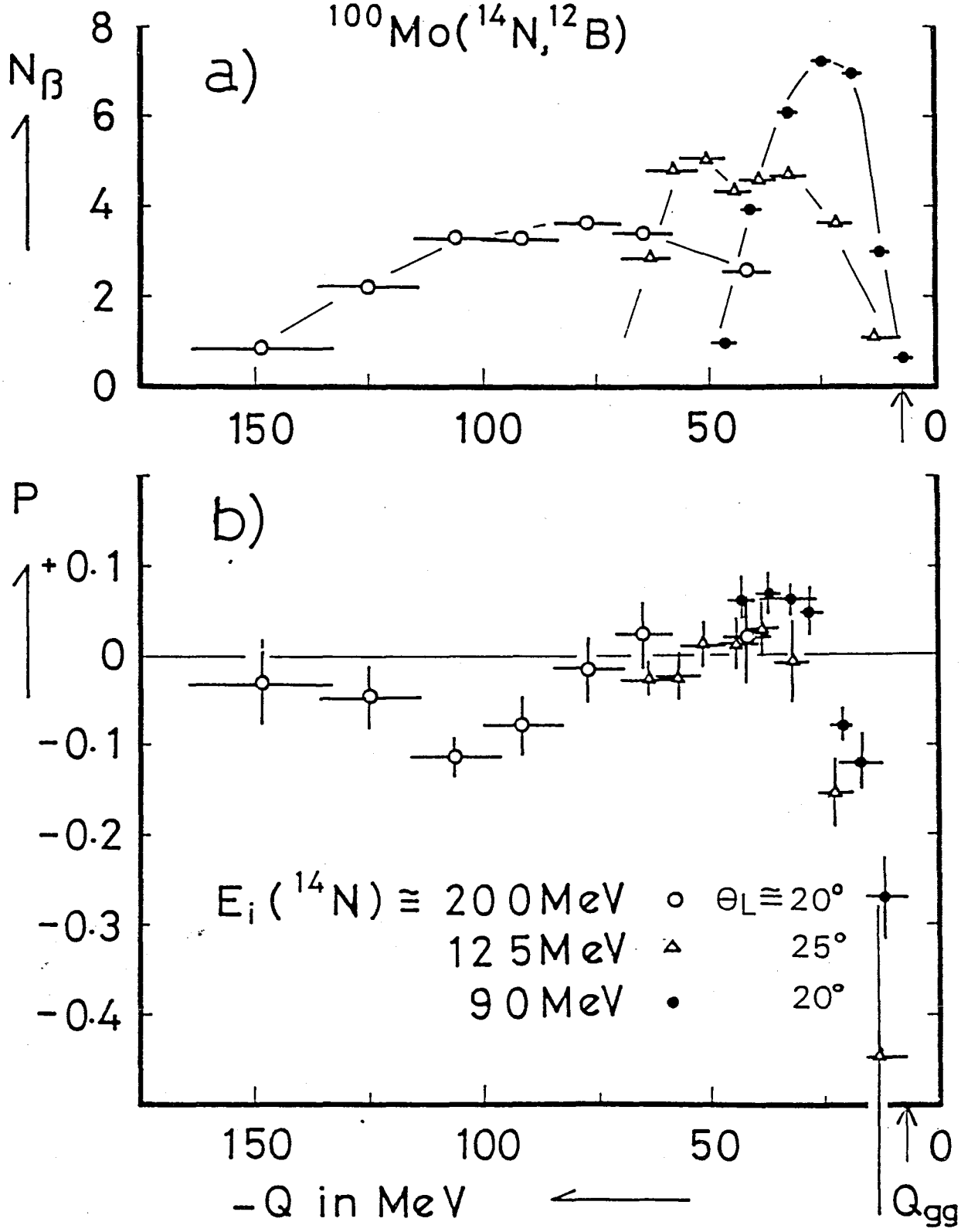

Fig.35 Experimental results of our previous study. Polarization of ^{12}B produced in $^{100}Mo(^{14}N,^{12}B)$ at incident energies of 90, 120 and 200 MeV.

Target	Incident Energy(MeV)	Scattering Angle(Deg.)
^{232}Th	129	30
	200	30
^{100}Mo	120	25, 35
	122	13, 20
	200	20
^{nat}Cu	120	20
^{nat}Fe	116	15
	112	25
^{45}Sc	114	13, 20
^{27}Al	115	6, 10
	120	20
	200	20

Table. 4 Summary of the experimental conditions, targets, scattering angles and incident energies.

4-1-a Target mass dependence

The experimental results of the ^{12}B polarization and ^{12}B energy spectrum measured near the grazing angle are shown in Fig.36. The vertical bars are the statistical uncertainties. The horizontal bars show the kinetic energy (Q-value) windows for ^{12}B deduced from the range-energy method.

The targets used are ^{27}Al, ^{45}Sc, ^{nat}Fe, ^{nat}Cu, ^{100}Mo and ^{232}Th, the incident energy was about 120Mev. For heavy targets, ^{nat}Fe, ^{nat}Cu, ^{100}Mo and ^{232}Th, large and negative polarization was also clearly observed in the region of small energy loss. The polarization became positive or zero with increase of energy loss. The Q-value for the polarization at zero crossing was almost the same compared with a ^{100}Mo target. The polarization became negative again in a region of larger energy loss. The Q-value for this zero crossing was, however, different from that of the ^{100}Mo target and shifted towards a large energy loss with increase of the mass number of targets, A. To simplify description of the experimental results, special appellations are given to the following points:

(1) First zero crossing;

Point where the polarization changes to positive (or zero) from a negative value with increase of the kinetic energy loss.

(2) Second zero crossing;

Point where the polarization changes to negative from positive (or zero) value with increase of the kinetic energy loss.

These points are shown schematically in Fig. 37. A systematic dependence of the polarization on the mass number of target nucleus can be described as follows:

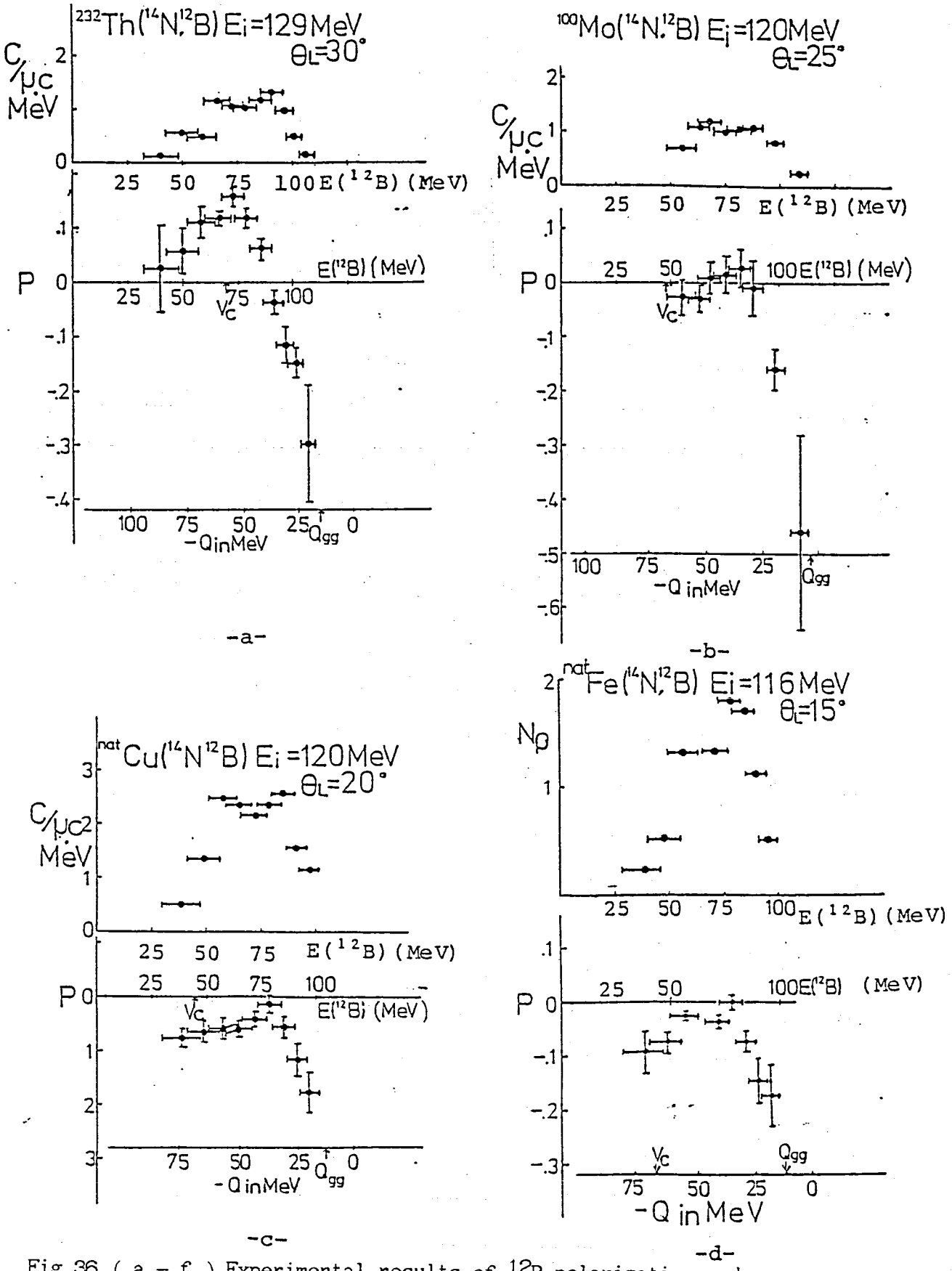

Fig.36 (a – f) Experimental results of ^{12}B polarization and energy spectrum measured near the grazing angle for various targets. The vertical bars are the statistical uncertainties and the horizontal bars show the kinetic energy (Q-value) windows deduced from the range-energy relation. Effects of the possible depolarization (See 3-5) are not corrected.

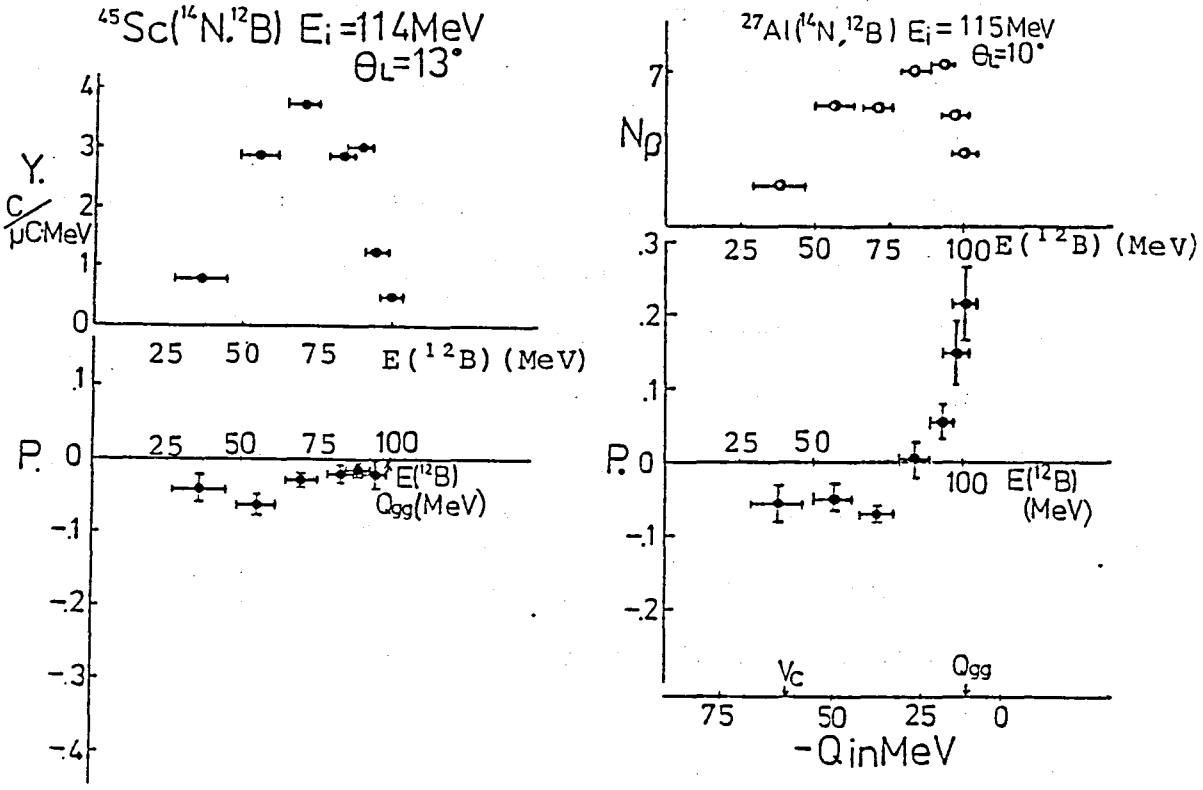

-e- -f-

Fig.36 (a - f) Experimental results of ^{12}B polarization and energy spectrum measured near the grazing angle for various targets. The vertical bars are the statistical uncertainties and the horizontal bars show the kinetic energy (Q-value) windows deduced from the range-energy relation. Effects of the possible depolarization (See 3-5) are not corrected.

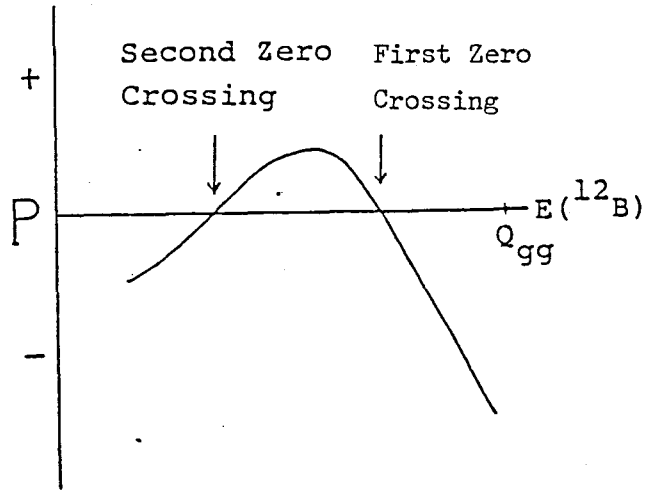

Fig.37 Diagram indicating the first and the second zero crossings of the polarization.

(1) The first zero crossing is almost independent of A.

(2) The second zero crossing shifts toward small energy loss with decrease of A.

The first and the second zero crossings coincide for ^{nat}Fe and ^{nat}Cu targets. For a light target, another change of the polarization was observed. For ^{27}Al, the polarization in the region of small energy loss was large and positive and became negative with increase of kinetic energy loss. For ^{45}Sc, the polarization in the region of small energy loss was nearly equal to zero.

(3) The polarization for the least energy loss changes from a large negative to a large positive value for $A < 45$.

In the other words, the first zero crossing disappears when $A < 45$ and only the second zero crossing is seen for ^{27}Al.

A third systematic dependence of the polarization as a function of A is thus obtained. The systematic change of the second zero crossing is also obtained for ^{27}Al and ^{45}Sc. The experimental results near the second zero crossing with various targets are displayed in Fig. 38-a and these near the first zero crossing are displayed in Fig. 38-b. The systematic dependence (1) and (2) are clearly shown in these figures. The polarization in the region of small energy loss is shown in Fig. 39 to indicate the dependence (3).

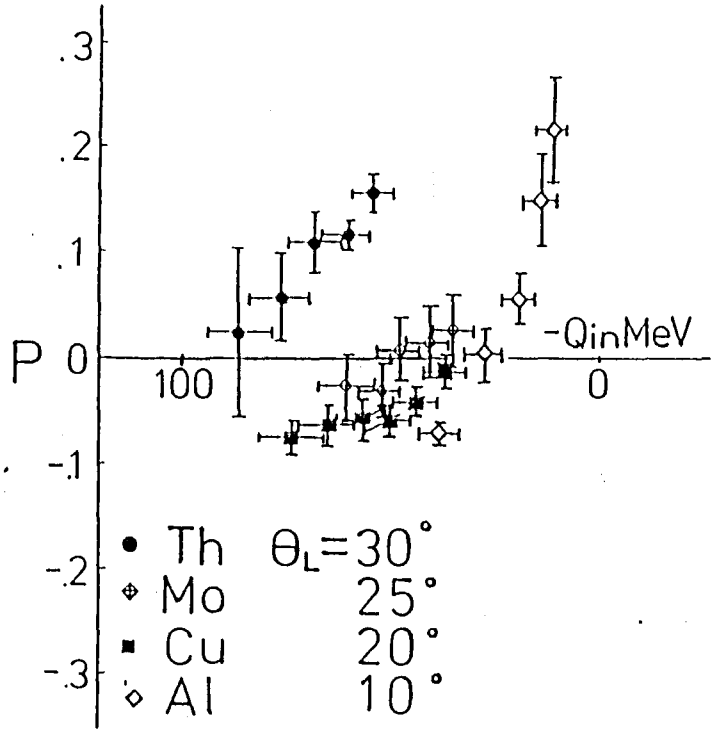

Fig.38-a Superposed illustration of experimental results near the second zero crossing measured near the grazing angle for various targets.

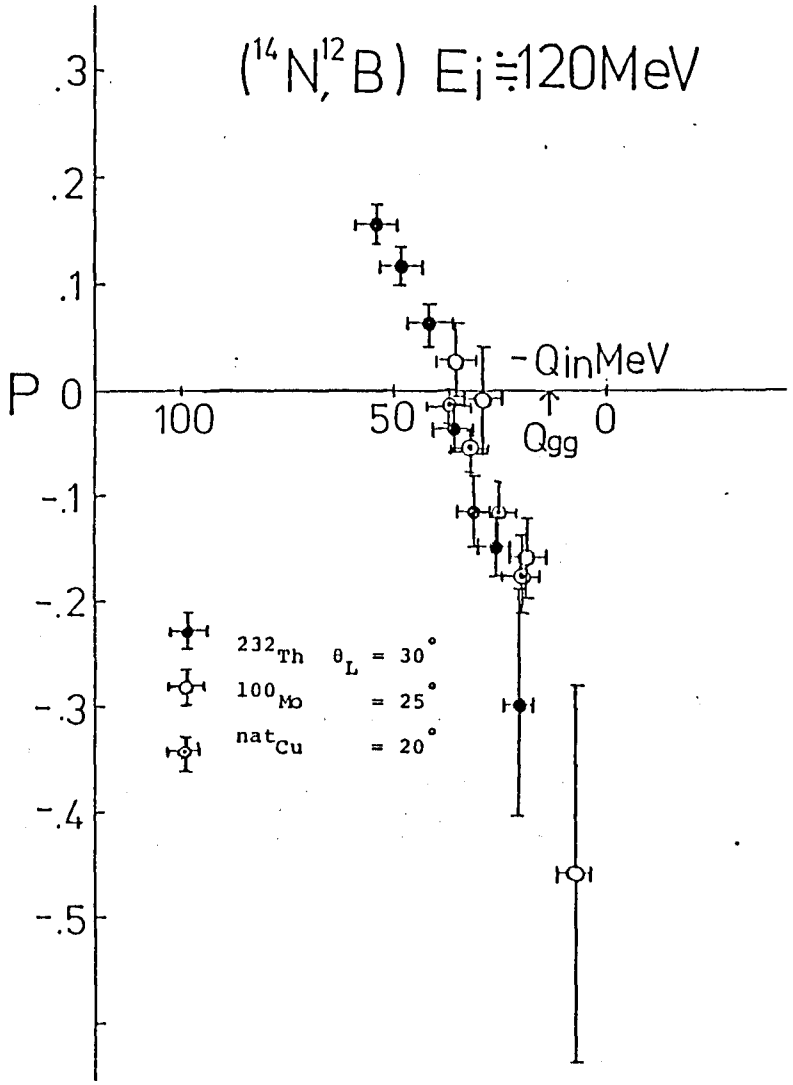

Fig.38-b Superposed illustration of experimental results near the first zero crossing measured near the grazing angle for various targets.

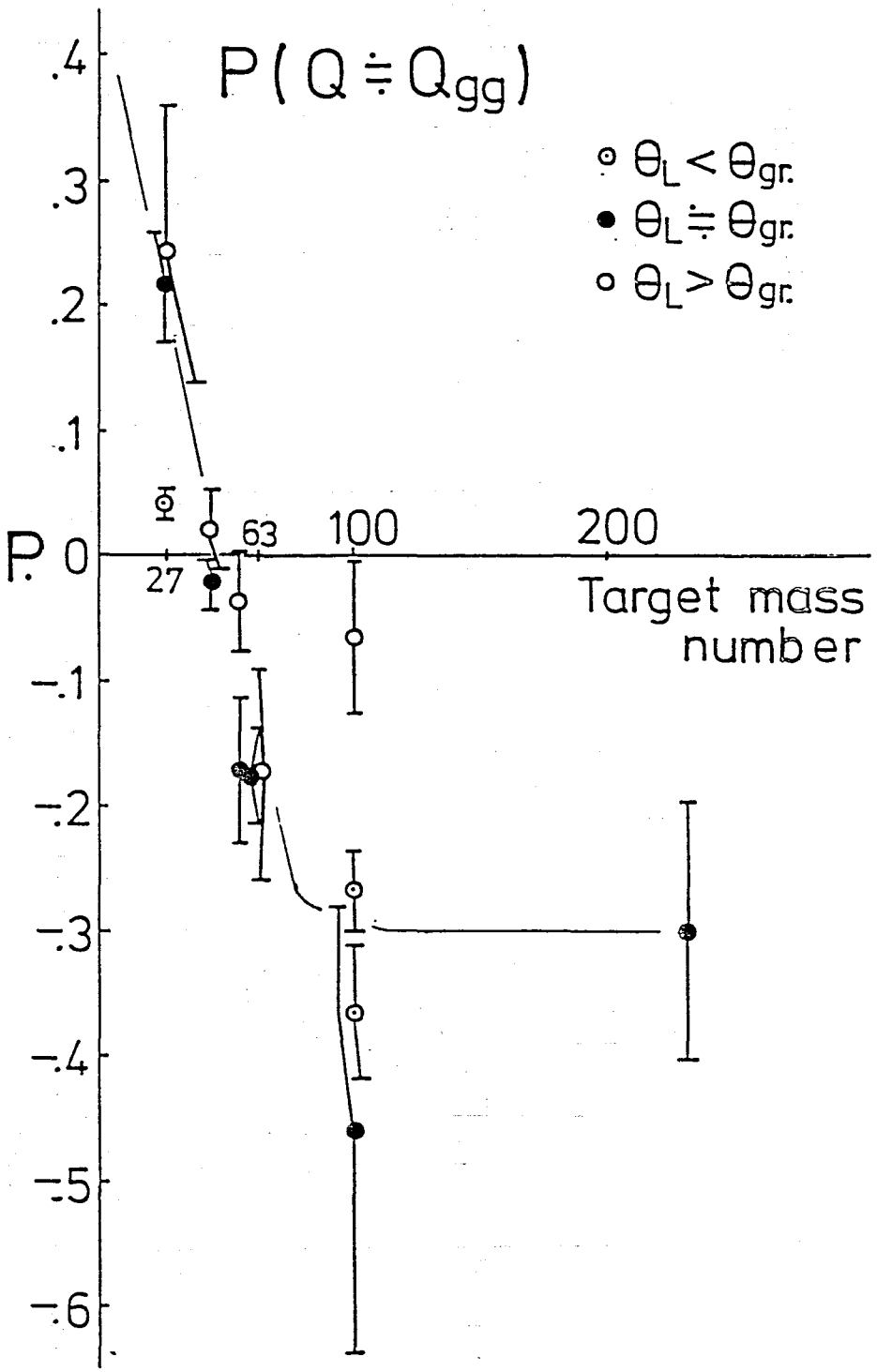

Fig.39 The polarization for the region of small energy loss. The mass number of target, A is plotted along the abscissa and the solid line is a guide of eye. The polarization changes from a large negative value to a large positive value at A = 45.

4-1-b Scattering angle dependence

The polarization of ^{12}B was also measured as a function of scattering angle. The experimental results measured at forward and backward angles from the grazing angle are shown in Fig. 40 and summarized in Fig. 41.

Two clear trends of polarization with scattering angle were observed. One is the shift of the first zero crossing. As a typical example for ^{100}Mo, the first zero crossing moves to small energy loss when the scattering angle increases in the backward angle. In the other words, the polarization in this energy loss region shifts towards the positive direction with increasing scattering angle. This tendency was observed also for ^{nat}Fe and ^{45}Sc.

The other trend was observed in the relative value of the polarization. The polarization of ^{12}B with kinetic energy below the second zero crossing became large with increase of scattering angle. As a typical example, the maximum value of negative polarization for ^{27}Al was about -0.2 at θ_L = 20 deg., about -0.08 at θ_L = 10 deg. and about -0.04 at θ_L = 6 deg. This trend with scattering angle was observed also for ^{nat}Fe and ^{45}Sc.

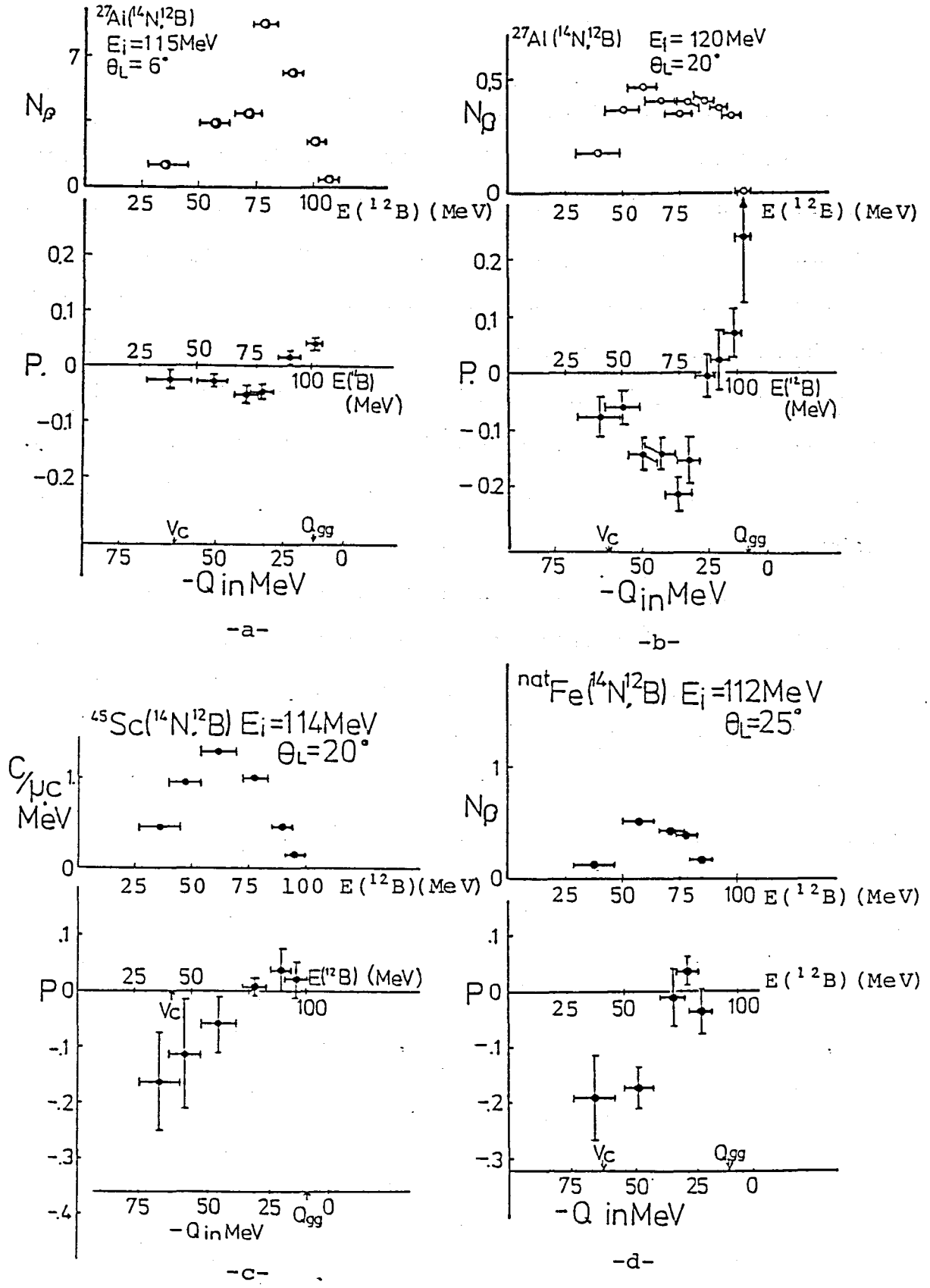

Fig.40 (a – g) Experimental results of ^{12}B polarization and energy spectrum measured on various scattering angles. The vertical bars are the statistical uncertainties and the horizontal bars show the kinetic energy (Q-value) windows deduced from the range-energy relation. Effects of the possible depolarization (See 3-5) are not corrected.

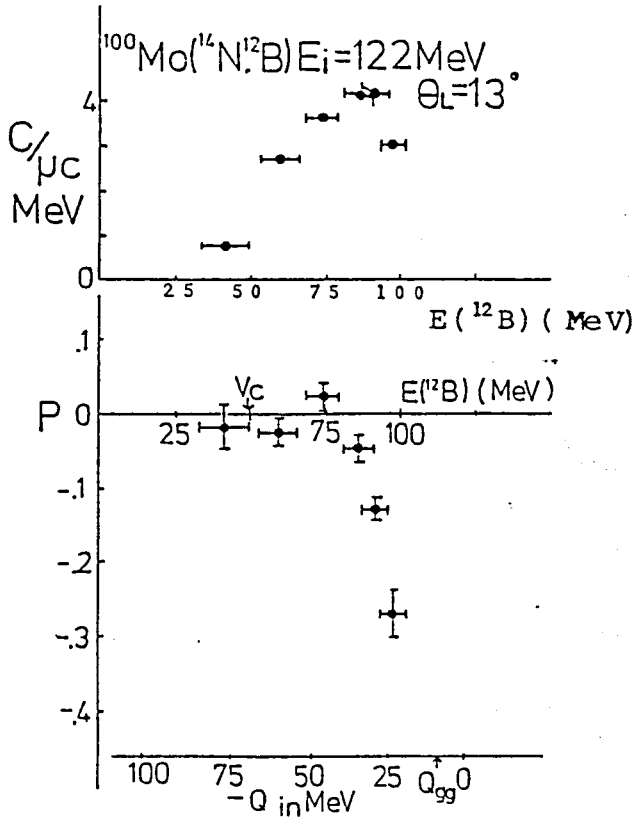

-e-

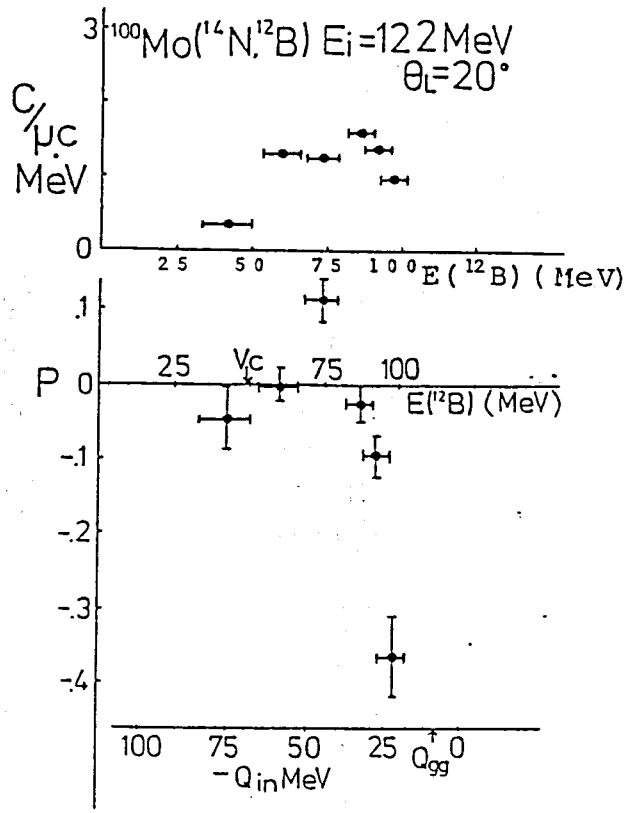

-f-

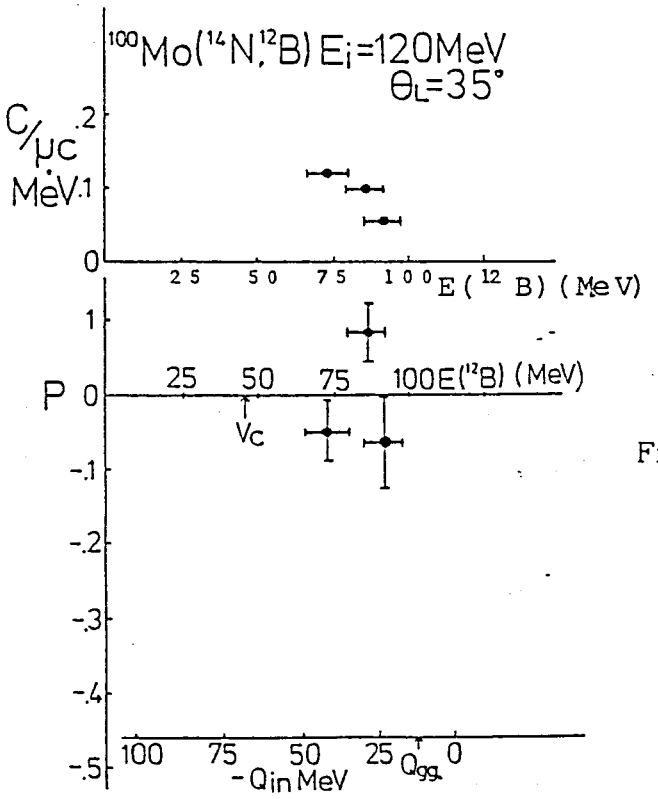

-g-

Fig.40 (a - g) Experimental results of ^{12}B polarization and energy spectrum measured on various scattering angles. The vertical bars are the statistical uncertainties and the horizontal bars show the kinetic energy (Q-value) windows deduced from the range-energy relation. Effects of the possible depolarization (See 3-5) are not corrected.

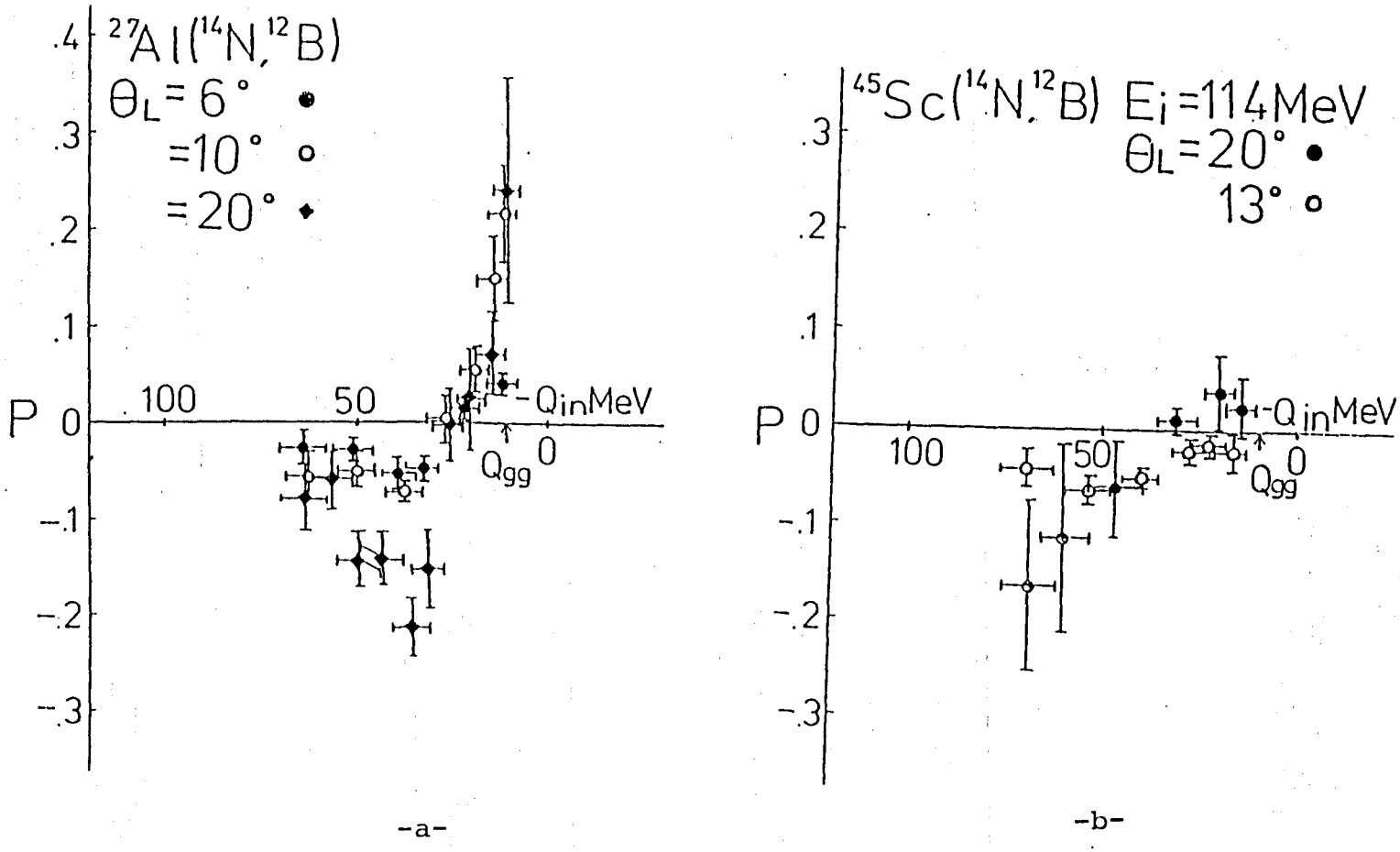

Fig.41 (a – d) The experimental polarization at various scattering angles. The vertical bars are the statistical uncertainties and the horizontal bars show the kinetic energy (Q-value) windows deduced from the range-energy relation. Effects of the possible depolarization (See 3-5) are not corrected.

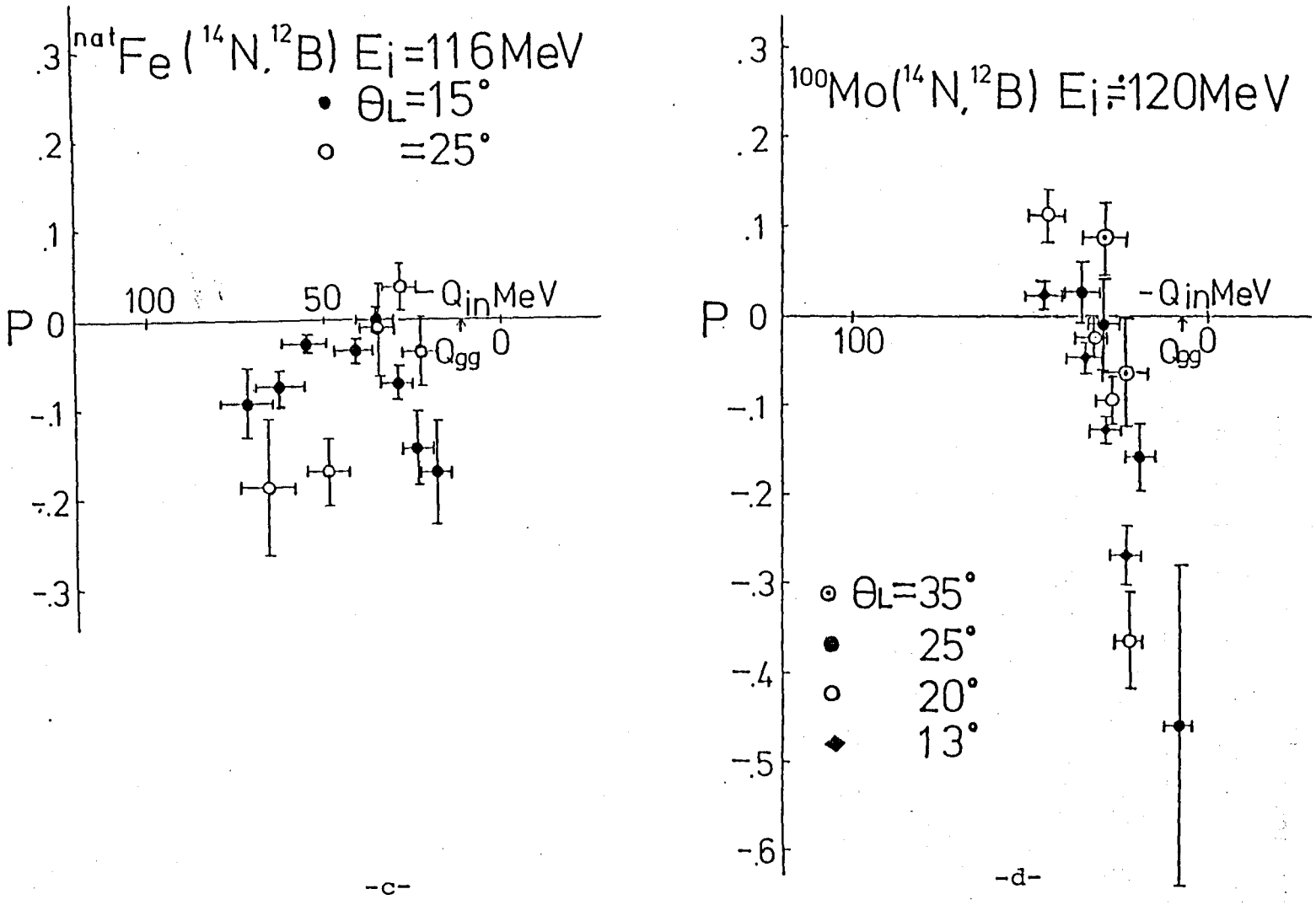

Fig.41 (a – d) The experimental polarization at various scattering angles. The vertical bars are the statistical uncertainties and the horizontal bars show the kinetic energy (Q-value) windows deduced from the range-energy relation. Effects of the possible depolarization (See 3-5) are not corrected.

4-1-c Incident energy dependence

The polarization of ^{12}B at an incident energy of 200 MeV was measured for ^{232}Th, ^{100}Mo and ^{27}Al. The scattering angles were slightly backward of the grazing angle or at the grazing angle. A similar polarization was observed at an incident energy of 120 MeV as shown in Fig. 42. In the region of small energy loss, a negative polarization was observed for ^{100}Mo and ^{232}Th. However, it was positive for ^{27}Al. The second zero crossing shifted towards small energy loss as the target mass became smaller. The reaction Q-value of the second zero crossing was about -40 MeV for ^{27}Al, about -70 MeV for ^{100}Mo and about -150 MeV for ^{232}Th.

The experimental results for these three targets are summarized in Fig. 43.

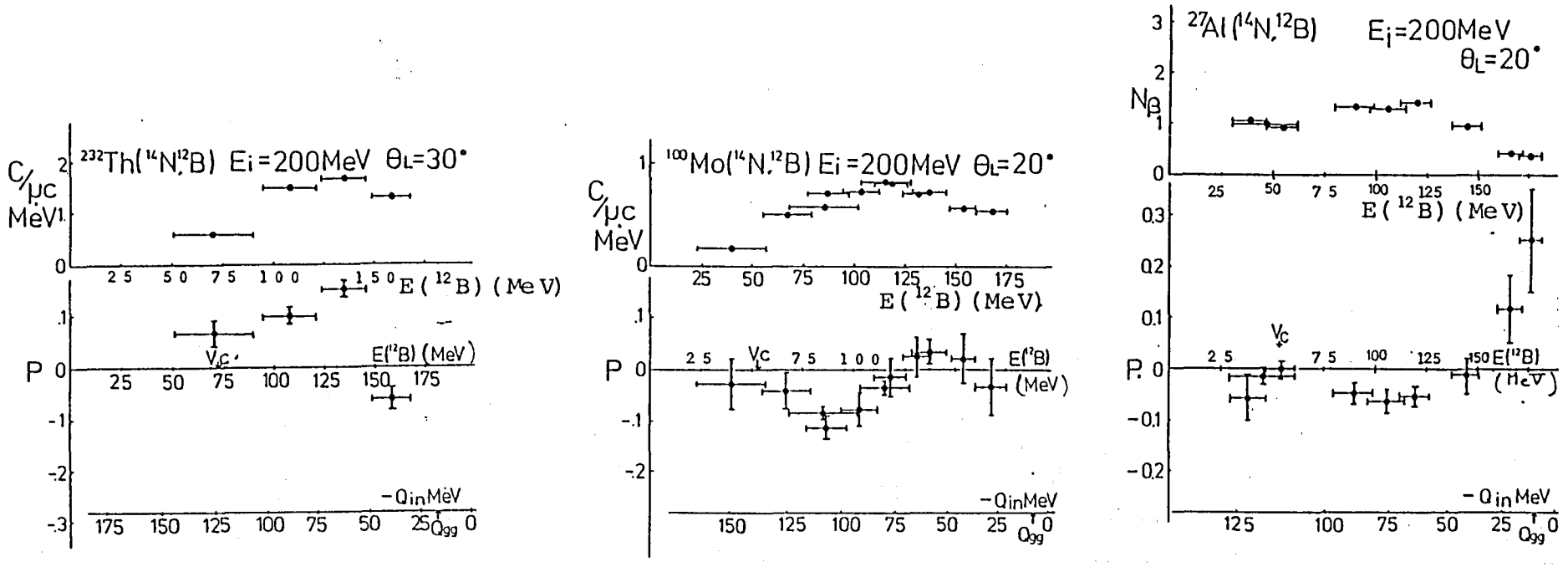

-a- -b- -c-

Fig.42 (a – c) Experimental results of ^{12}B polarization and energy spectrum measured at an incident energy of 200 MeV. The vertical bars are the statistical uncertainties and the horizontal bars show the kinetic energy (Q-value) windows deduced from the range-energy relation. Effects of the possible depolarization (See 3-5) are not corrected.

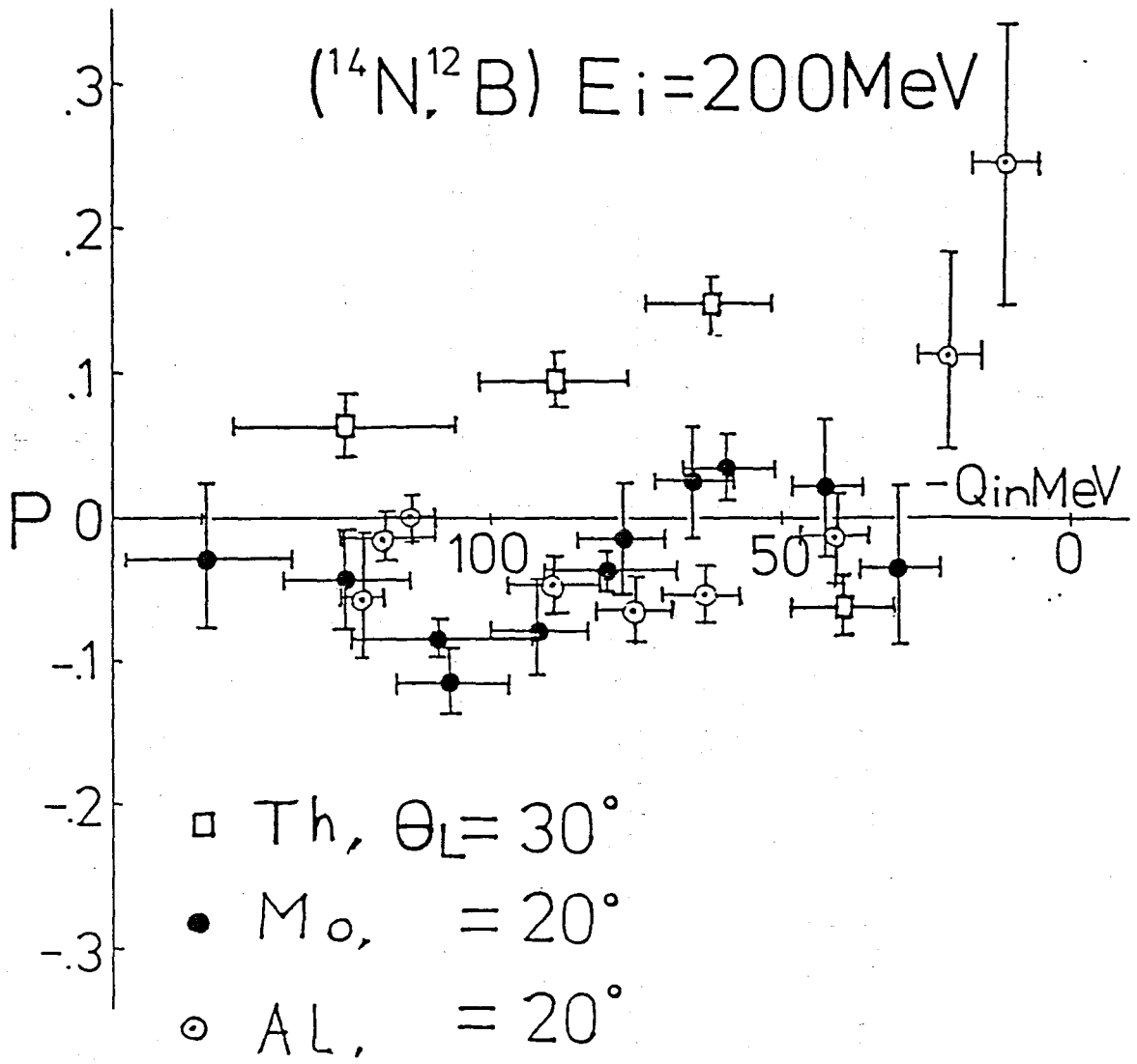

Fig.43 The experimental polarization for various targets at an incident energy of 200MeV. The vertical bars are the statistical uncertainties and the horizontal bars show the kinetic energy (Q-value) windows deduced from the range-energy relation. Effects of the possible depolarization (See 3-5) are not corrected.

4-1-d Summary of the experimental results

The polarization of ^{12}B observed in the present study are summarized as follows:

(1)-1 The first zero crossing appears at the same energy loss almost independent of A when scattering angle is near grazing angle and target is from ^{nat}Fe to ^{232}Th.

(1)-2 The first zero crossing disappears for light targets such as ^{27}Al.

(1)-3 The first zero crossing shifts toward smaller energy loss than that at grazing angle when scattering angle is backward from grazing angle and target is from ^{nat}Fe to ^{232}Th.

(2) The second zero crossing shifts toward small energy loss with decreasing A.

(3) The relative value of the polarization at the fixed energy loss becomes larger with increase of the scattering angle.

The experimental values of the first and the second zero crossings are summarized in Table 5.

The tendency (1)-1 is due to the effect of direct two proton transfer from the projectile to the target. This mechanism is described in Chap. 2 from Brink's matching condition. The polarization which is induced by the direct two proton transfer is large and negative for the least energy loss and becomes positive with an increase in the kinetic energy loss. The zero crossing at this polarization is described by the matching Q-value defined in Eq. (2-21), where the relative velocity v is expressed by

$$v^2 = 2(E_{cm}-V_{ci})/\mu \qquad (4-1)$$

where μ is the reduced mass.

For two proton transfer from the projectile to the target the matching

Target	Incident Energy (MeV)	Scattering Angle (Deg.)	-Q for first zero crossing (MeV)	-Q for second zero crossing (MeV)
^{27}Al	115	6	////	25 ± 5
		10	////	27 ± 5
	120	20	////	25 ± 5
	200	20	////	38 ± 6
^{45}Sc	114	13	////	24 ± 5
		20	////	34 ± 5
^{nat}Fe	116	15	35 ± 5	35 ± 5
	112	25	25 ± 5	35 ± 5
^{nat}Cu	120	20	35 ± 5	35 ± 5
^{100}Mo	122	13	42 ± 6	53 ± 6
		20	35 ± 5	51 ± 6
	120	25	31 ± 5	49 ± 7
		35	25 ± 7	37 ± 7
	200	20	37 ± 7	73 ± 8
^{232}Th	129	30	38 ± 5	90 ± 7
	200	30	45 ± 11	////

Table. 5 Q-values for the first and the second zero crossings

Q-value is given by

$$Q_{match} = \frac{2e^2(Z_1 - Z_2 + 2)}{r_0(A_1^{1/3} + A_2^{1/3})} - 2\frac{A_1 + A_2}{A_1 A_2}\left(E_L \frac{A_2}{A_1 + A_2} - \frac{e^2 Z_1 Z_2}{r_0(A_1^{1/3} + A_2^{1/3})}\right) \quad (4\text{-}2)$$

where E_L is the incident energy in the laboratory frame, A_i and Z_i are the mass and the atomic numbers of interacting nuclei, r_0 is the radial parameter and the radius R of nucleus is given by $R_i = r_0 \cdot A^{1/3}$ (fm). e is the unit of electric charge. The subscripts i = 1 and i = 2 stand for the projectile and the target nuclei, respectively.

The value of r_0 used in the present calculation is 1.2 fm and the calculated matching Q-values for various targets studied here are listed in Table 6. The values are distributing around $2 \cdot E_i/A_1$.

The tendency (2) can be qualitatively understood within the framework of the classical frictional model as follows: The projectile-like-fragment produced in the frictional process is expected to be polarized with the same sign of deflection angle. A negative polarization thus indicates a negative deflection angle. The moment of inertia of the di-nuclear system formed in the frictional process is small while its rotating velocity is large for light target. As a result, the interaction time in which the projectile nucleus is deflected to a negative angle becomes short. If the energy dissipation rate by frictional forces is not drastically changed during the interaction, the fragment is emitted into a negative angle with small kinetic energy loss for a light target.

The mechanism (3) can also be understood in terms of the classical frictional model. In this model the definition of the polarization is

Target	Incident Energy (MeV)	Q matching (MeV)
^{27}Al	115	-14
	120	-15
	200	-26
^{45}Sc	114	-16
^{nat}Fe	116	-17
	112	-16
^{nat}Cu	120	-18
^{100}Mo	120	-20
	122	-21
	200	-32
^{232}Th	129	-28
	200	-38

Table. 6

Calculated matching Q-values of direct two-proton transfer.

$$P = (\sigma_+ - \sigma_-)/ (\sigma_+ + \sigma_-). \qquad (4-3)$$

Both partial cross sections σ_+ and σ_- from the positive and the negative angle deflection processes contribute destructively to the polarization. Here complete polarization for both orbits is assumed.

At a backward angle the contribution from a positive angle deflection process becomes small and the magnitude of the negative polarization becomes large.

The tendencies (1)-2 and (1)-3 can be understood as results of the coexistence of two different reaction mechanisms in the region of small energy loss. One reaction mechanism produces a negative polarization and the other produces a positive polarization. The former is from direct two proton transfer process whereas latter is due presumably to the frictional process with a positive deflection angle. At an angle backward from grazing angle, the ratio of the frictional process to the direct process becomes relatively larger than at a forward angle. Consequently, the polarization at a backward angle moves positive and the first zero crossing shifts toward a small energy loss.

The ratio of different processes changes as a function of A. For ^{100}Mo, the main reaction process which produces ^{12}B in the region of small energy loss is the direct two proton transfer process. However, a small contribution from a frictional process exists with it and the positive polarization from the frictional process although not visible may be superimposed on the polarization from the direct process. For ^{27}Al the frictional process is the dominant reaction mechanism in the region of small energy loss and for ^{45}Sc the polarization from the frictional process about

equal to the polarization from the direct two proton transfer process. This A dependence is attributed to the change of interaction time of the frictional process as a function of A. Reaction products from the frictional process appears with small energy loss at a scattering angle for light nuclei and mixes with the direct process in the region of small energy loss. For ^{27}Al, the dominant reaction process at this energy loss region is frictional and the polarization from the direct process is masked by the polarization from the frictional process.

4-2 Discussion

4-2-a Analysis by use of classical friction model

In this section, the friction model is applied to (^{14}N,^{12}B) reactions. The model reproduces the systematic variation of the ^{12}B polarization qualitatively (Ta 83). The gross properties of ^{12}B polarization is explained in the framework of the classical friction model except in the region of small energy loss with heavy targets where the direct two proton transfer process plays an important role.

Attention is given to the changes of the second zero crossing as a function of A, the mass number of the target (Mi 83). The reaction Q-values of the second zero crossing are shown in Fig.44 as a function of A. The data are obtained from results measured near grazing angle. The error bar corresponds to the energy range for ^{12}B deduced from the range-energy relation near the second zero crossing. The reaction Q-values of the second zero crossings are fitted with a straight line. This relation can be reproduced by the friction model. The second zero crossing is expected to be a good reference to the kinetic energy loss of projectile-like-fragments which come from the negative angle deflection. If the energy loss of reaction products from this process is large, the second zero crossing appears at the region with large energy loss and if small, the second zero crossing shifts toward the region with small energy loss.

The kinetic energy loss as a function of A, the mass number of the target, of projectile-like-fragments which come from the far side of the target nucleus is formulated as a first step of the analysis. And this formula well reproduces the experimental value of the energy loss of the

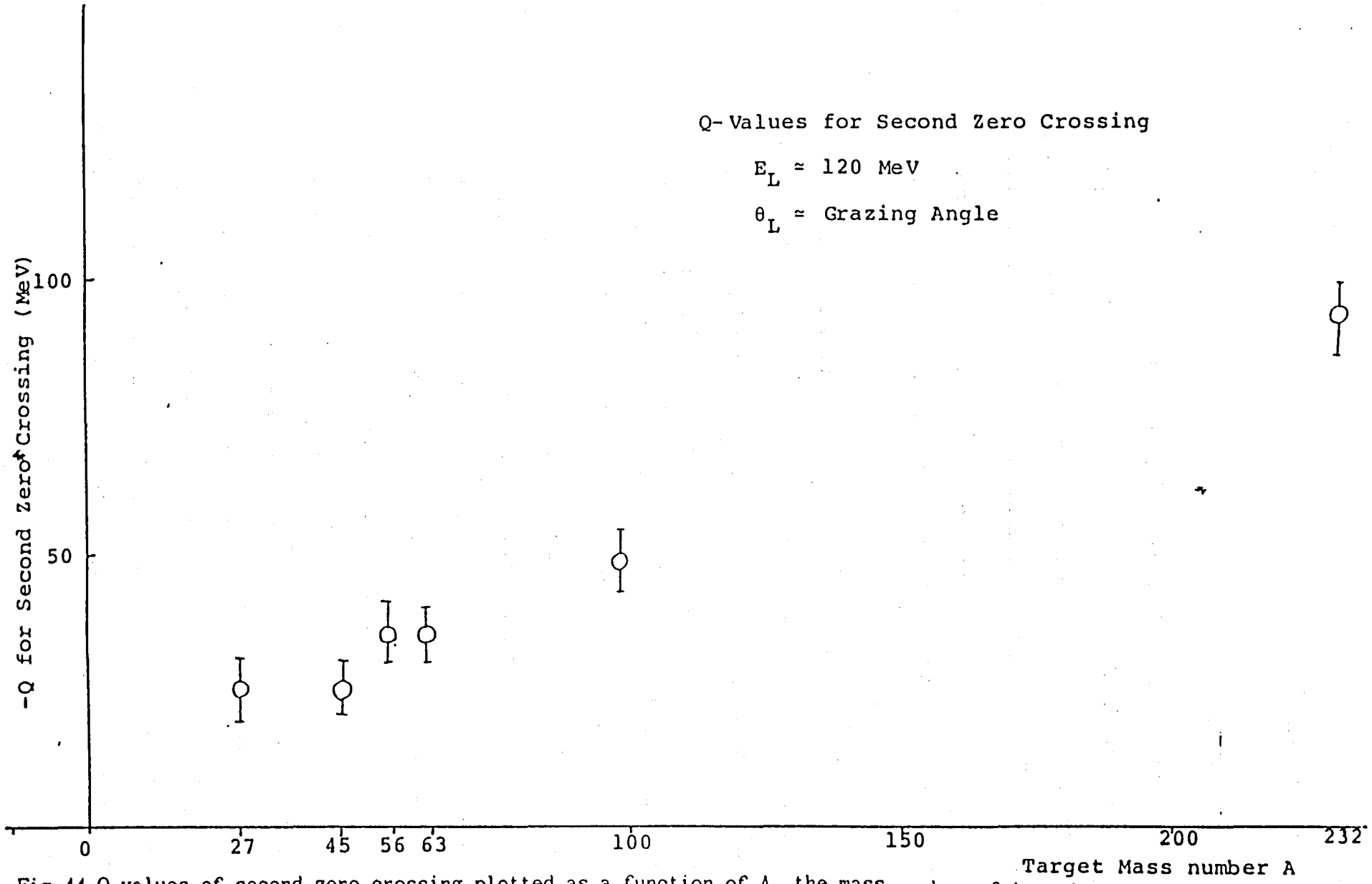

Fig.44 Q-values of second zero crossing plotted as a function of A, the mass number of target. The vertical bars show the kinetic energy (Q-value) windows deduced from the range-energy relation near the second zero crossing.

second zero crossing as a function of A. At the next step, we consider how the energy loss at the second zero crossing is related to the energy loss of the projectile-like-fragment. Models of heavy-ion reactions with negative angle deflection process are proposed and the averaged friction constant is extracted from the present experimental data in the framework of the collision models. At the last stage, a microscopic treatment of heavy-ion reaction, the Quasi Linear Response Theory (QLRT), is applied to (^{14}N,^{12}B) reactions and compared with the experimental data.

The frictional force is assumed to be proportional to the relative velocity v between the colliding nuclei. As described in Chap. 2, the kinetic energy loss from this frictional force is written as a function of the interaction time τ as

$$E_{loss} = E_i(1 - \exp(2k\tau/\mu)). \qquad (4-4)$$

The interaction time τ is determined from the angular velocity of the DNS and the rotation angle. The angular velocity is the ratio of the moment of inertia of the DNS and total angular momentum of the system. The moment of inertia I of the DNS is written as

$$I = \mu R^2 , \qquad (4-5)$$

where R is the distance between the centers of the interacting projectile and target nuclei and determined from a proximity potential (Bl 77) as

$$R = 1.15(A_1^{1/3} + A_2^{1/3}) - 1.37, \qquad (4-6)$$

where A_1 and A_2 are the mass numbers of the projectile and the target and 1.37 is the universal penetration depth determined from the proximity potential.

The orbital angular momentum J carried into the DNS is

$$J = R\sqrt{2(E_{cm}-V_{ci})\mu}, \qquad (4-7)$$

where V_{ci} is Coulomb energy of an incoming channel.

The rotation angular velocity ω of the DNS is the ratio of I and J as

$$\omega = J/I = \sqrt{2(E_{cm} - V_{ci})/\mu}\ /R. \qquad (4-8)$$

The rotation angle θ is taken as twice the grazing angle, θ_{gr} because the measurement were carried out near the grazing angle as seen in Fig. 45 and written as

$$\theta = 2\times\theta_{gr} = 4sin^{-1}\frac{D}{2R-D}. \qquad (4-9)$$

where D is defined as $D = Z_1 \times Z_2/E_{cm} = V_c \times R/E_{cm}$. The quantity θ can be rewritten by expanding the function $\sin^{-1}$ and by taking the leading term because E_{cm} is much higher than V_{ci}. The expression is

$$\theta = \frac{4D}{2R-D}. \qquad (4-10)$$

Then the interaction time τ is defined as $\tau = \theta/\omega$ and written as

$$\tau = \theta/\omega = \sqrt{2\mu/E_{cm}}\ (V_{ci}R/(E_{cm} - V_{ci})). \qquad (4-11)$$

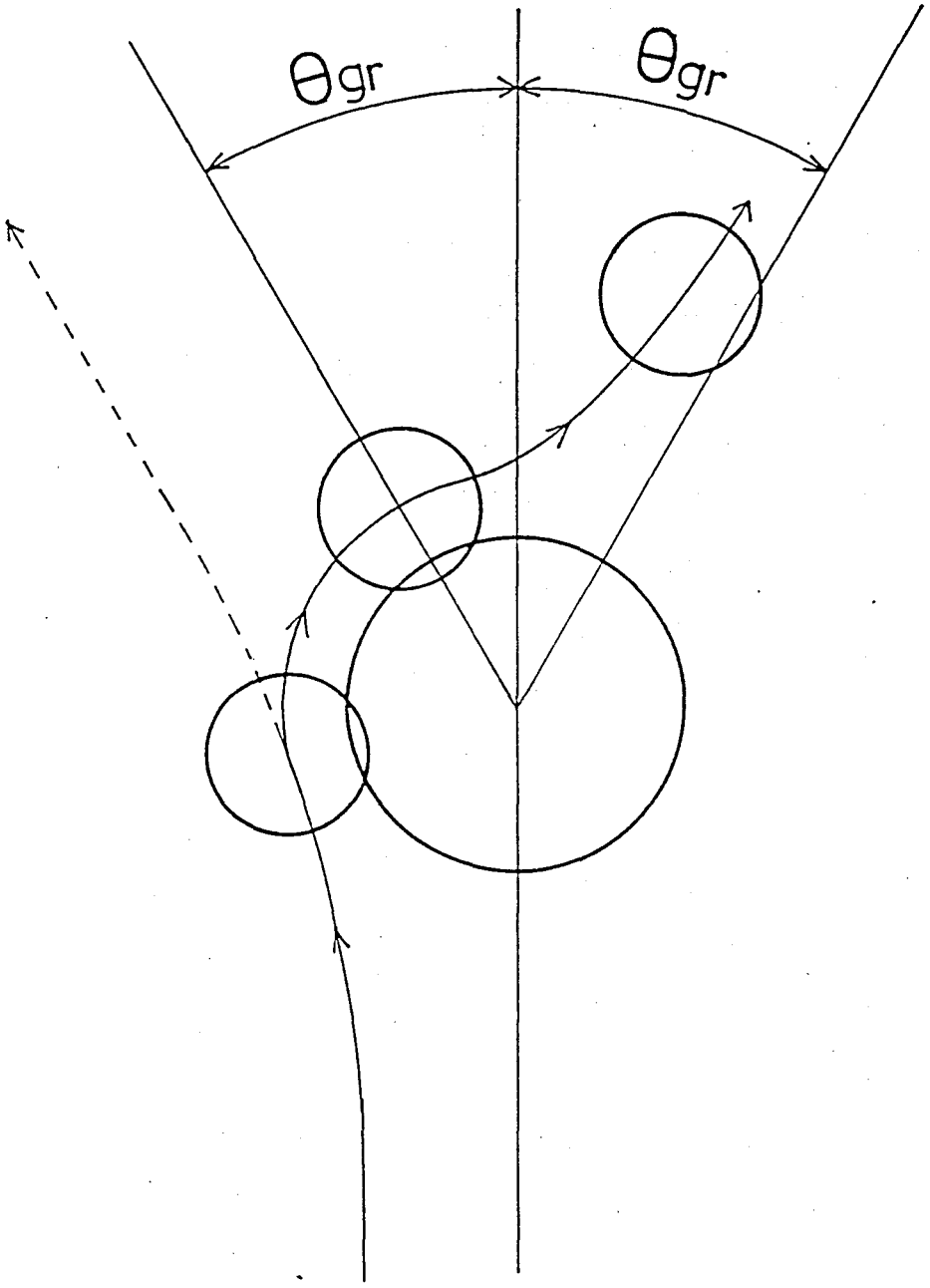

Fig.45 Schematic illustration of a frictional scattering process used to reproduce the change of the second zero crossing with A.

The energy loss by the nuclear frictional forces is obtained by using Eq. (4-4) and τ. Expanding Eq. (4-4) and taking the leading term, the energy loss is expressed by

$$E_{loss} = 2k\tau(E_{cm} - V_{ci})/\mu \qquad (4-12)$$

$$= (A_1 + A_2)k \; A_1/2E_L \qquad (4-13)$$

$$= 6.9 \times 10^{21} k(A_1 + A_2) \; A_1/2E_1 \text{ (MeV)}, \qquad (4-14)$$

where the approximation $Z_i = A_i/2$ is used in Eq. (4-12) to get Eq. (4-13). In Eq. (4-14), E_L and A_1 are the constants when reactions have the same incident energy and the same projectile. The energy loss is expressed linear to A_2. The solid line drawn in the Fig. 46 has been calculated from Eq. (4-14) for a friction constant 2.5 x 10^{-22} MeV s/fm^2. The calculationwell reproduces the systematic dependence of the second zero crossing as a function of A, the mass number of the target.

As a next step, we try to extract the averaged friction constant k which is expected to be independent of target mass A, scattering angle and incident energy. However the formalism used in the discussion above has to be refined in order to include the information of scattering angle, because the measurements were carried out with various scattering angles forward and backward of the grazing angle.

The constant k was calculated in following expression by solving Eq. (4-4) with respect to k.

$$k = -\frac{\mu}{2\tau} \log\left(\frac{E_{cm} - V_{cf} - E_{loss}}{E_{cm} - V_{ci}}\right) \qquad (4-15)$$

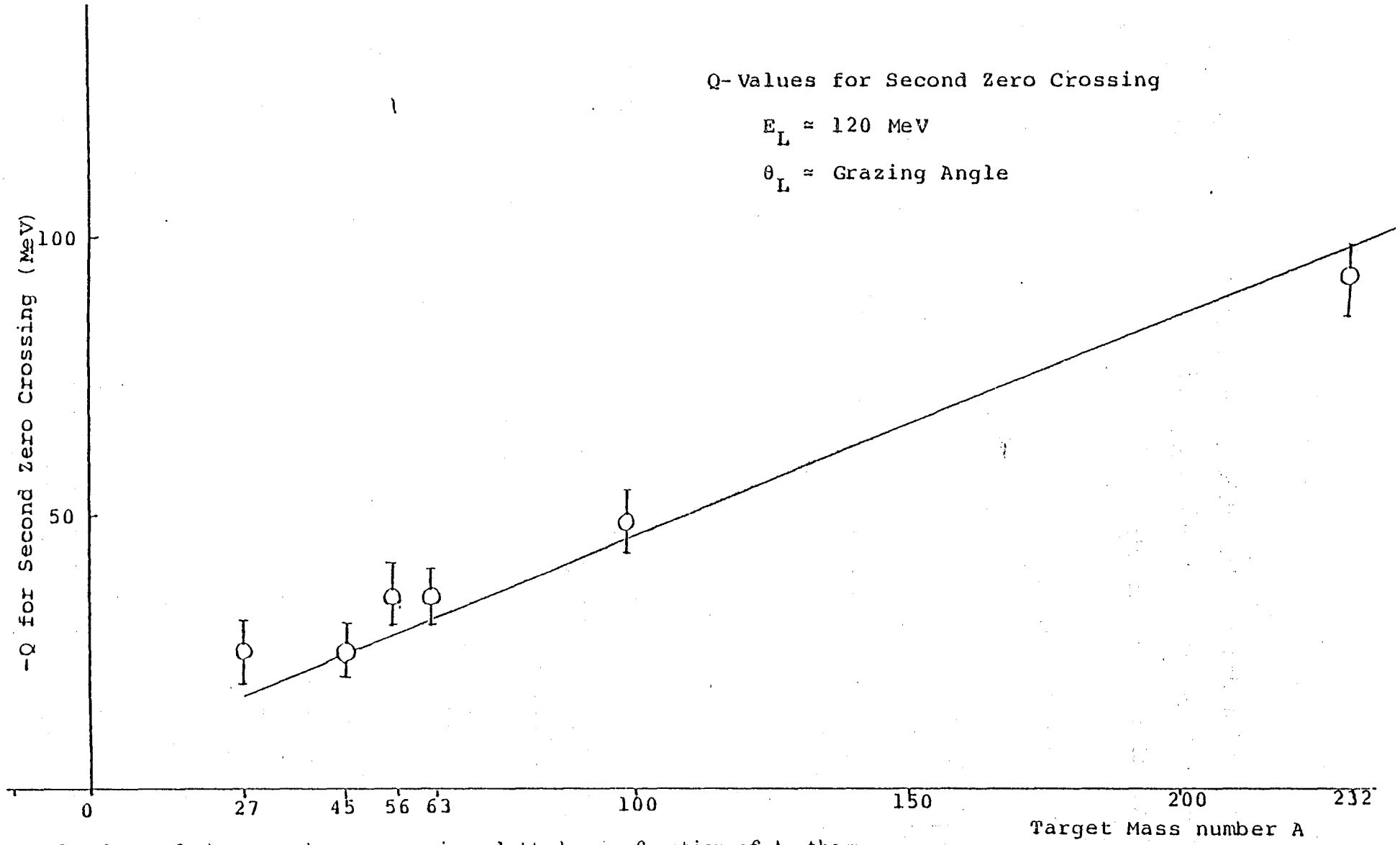

Fig.46 Q-values of the second zero crossing plotted as a function of A, the mass number of target. The vertical bars show the kinetic energy (Q-value) windows deduced from the range-energy relation near the second zero crossing. Solid line is calculated by a friction model of heavy-ion reaction with a friction constant 2.5×10^{-22} Mev·s/fm^2,

The interaction time τ is determined in essentially the same way as above. However the rotating angle θ is expressed in more detail in order to include information of the scattering angle as

$$\theta = (\theta_{gri}/2) + (\theta_{grf}/2) + \theta_{cm} , \qquad (4-16)$$

where θ_{cm} is the scattering angle in center of mass frame, θ_{gri} and θ_{grf} are grazing angles of the incoming and the outgoing channels as illustrated in Fig. 47. The θ_{cm} is determined from the scattering angle in laboratory frame θ_L by using the following

$$\theta_{cm} = \sin^{-1}(\delta \sin\theta_L) + \theta_L ,$$

where δ is a conversion coefficient defined as

$$\delta = \sqrt{\frac{A_1 A_1' (A_1' + A_2')}{A_2 A_2' (A_1 + A_2)} \cdot \frac{E_{cm}}{E_{cm} - E_{loss}}} . \qquad (4-17)$$

The quantities with prime refer to those of the reaction products. Applying the equation to process of two-proton transfer from the projectile to the target nuclei, δ is reduced to

$$\delta = \sqrt{\frac{168\, E_{cm}}{A_2 (A_2 + 2)(E_{cm} - E_{loss})}} . \qquad (4-18)$$

The θ_{gri} is the same as θ_{gr} in Eq. (4-8). The θ_{grf} is determined as

$$\theta_{grf} = 2\sin^{-1}\left(\frac{V_{cf}}{2(E_{cm} - E_{loss}) - V_{cf}}\right) . \qquad (4-19)$$

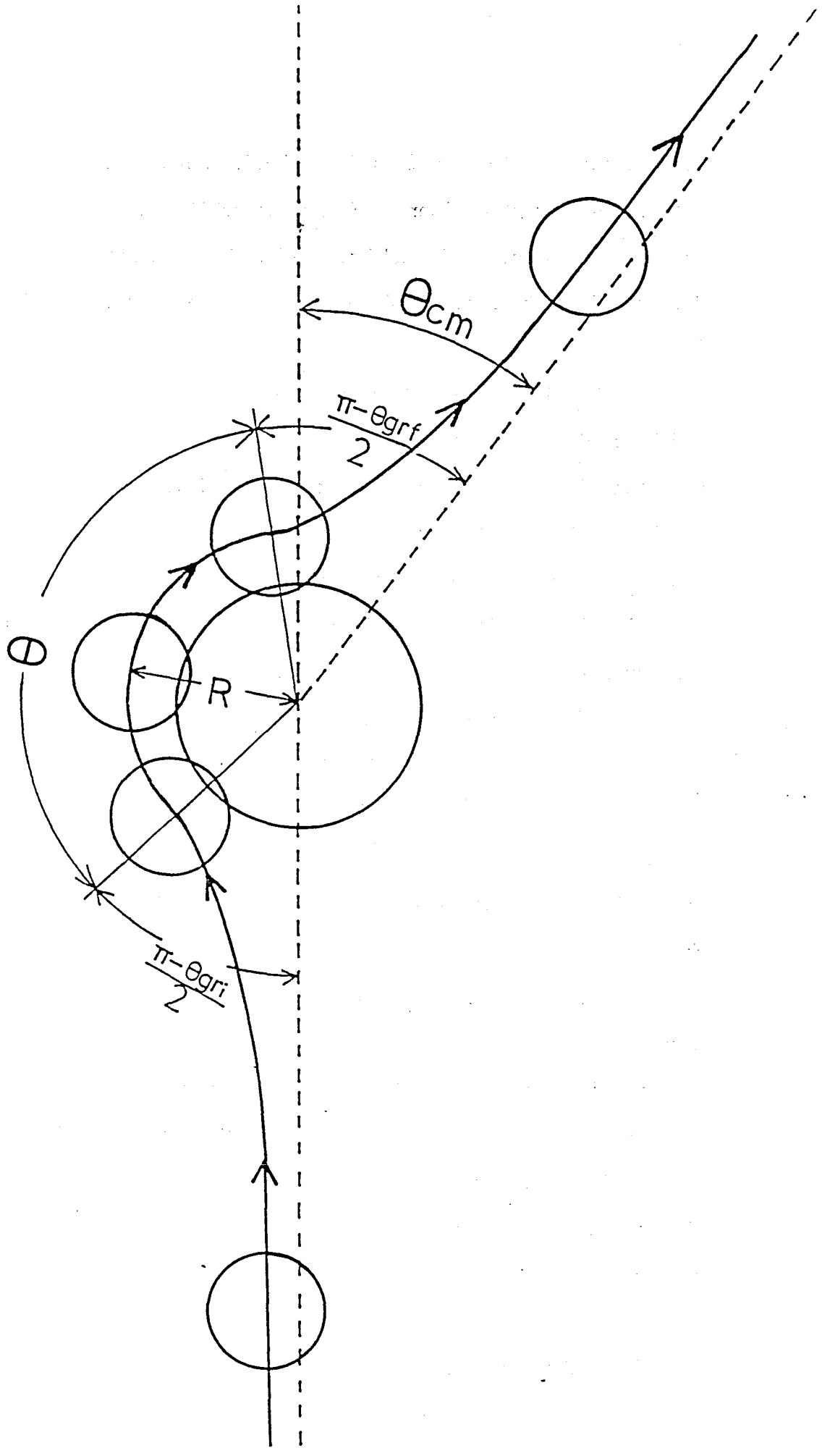

Fig.47 Schematic illustration of a frictional scattering process used for the calculation of the friction constant.

The rotating angle θ is thus determined. Note that θ is a function of E_{loss}. The moment of inertia I and the orbital angular momentum J are taken as the same as Eq. (4-5) and Eq. (4-7). The interaction time τ is then determined as the ratio of J to $\theta \cdot I$. The quantity τ is a function of E_{loss}.

In the calculation of the friction constant k, we have to use collision model for deducing the values of E_{loss} from the Q-values for the second zero crossing, Q(szc). As the first case (Case-1), the *l*-window model is used. In the model the contributions from the far side and from the near side of the target nucleus are with specific *l*-value. The fluctuation around the mean classical orbit causes the wide spread of energy spectrum. The second zero crossing is assumed as the point where the contributions from the far side and from the near side are of the same strength. E_{loss} is then expected to lie between -Q(szc) and -Q(Vcf) which refers to the Coulomb energy of two spherical nuclei in the final state of collision. The dependence on A of -Q(szc) and -Q(Vcf) is illustrated in Fig. 48. Q(Vcf) is at the largest energy loss of reaction product observed except for Th target. The values of E_{loss} are chosen at the mean values of -Q(szc) and -Q(Vcf) as a first approximation. Error of E_{loss} is assumed to be that of -Q(szc). For Th target, the energy spectrum of reaction product is not only down to V_{cf} for two spherical nuclei but also to lower energy beyond it. This fact suggests the large nuclear deformation at the final state of nuclear reaction and the deformation degree of freedom have to be included in the reaction model. Thus in the Th case, we used the modified final distance between the centers of nuclei as

$$R = Def \times (r_o \cdot (A_1^{1/3} + A_2^{1/3})) \qquad (4-20)$$

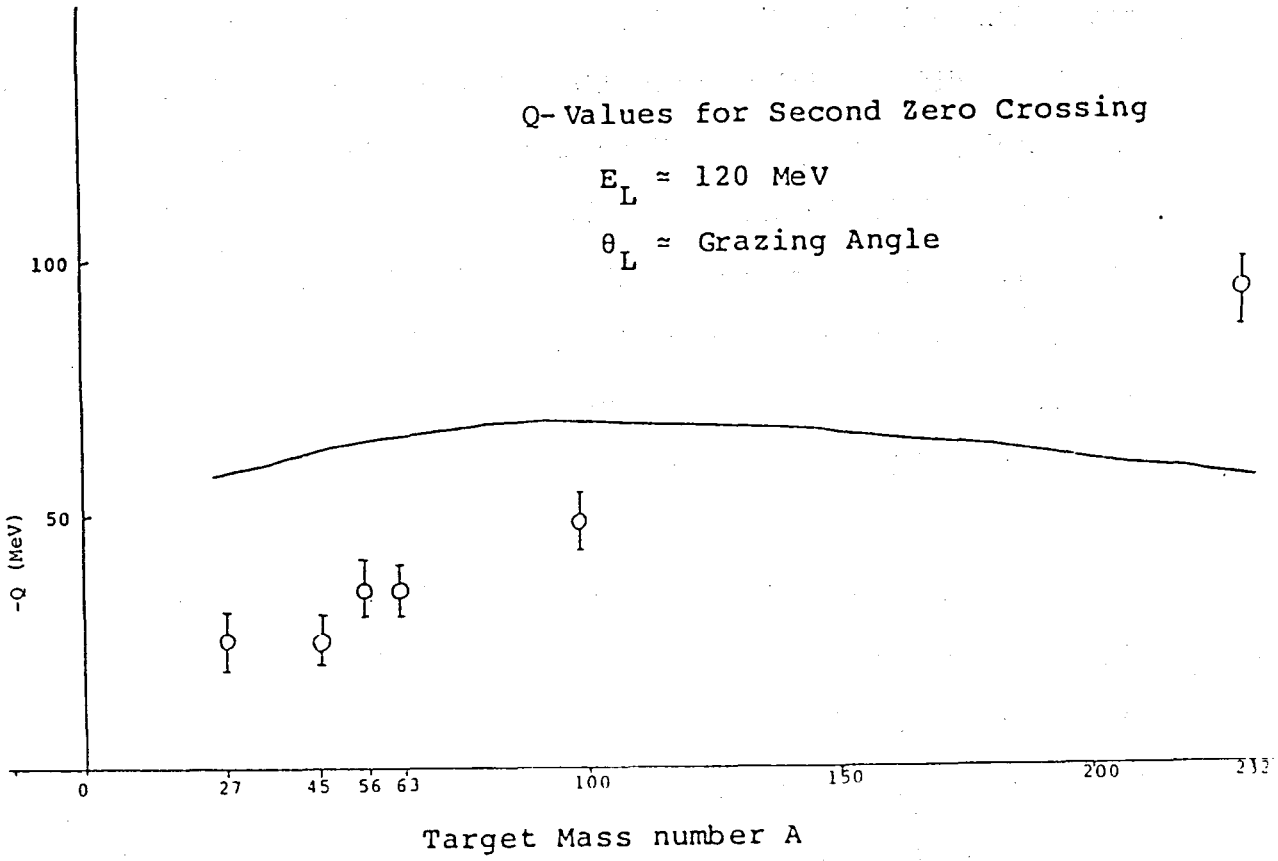

Fig.48 Q-values of the second zero crossing and for Coulomb energy at the final state of the collision (Solid line) under the assumption of spherical shape. These are plotted as a function of A, the mass number of target. The vertical bars show the kinetic energy (Q-value) windows deduced from the range-energy relation near the second zero crossing.

Here the deformation parameter Def is 1.8 and is reduced from deformation coefficient α in ref (Si 76) where the coefficient was used in reproducing the double differential cross section (Wilczynski plot) of Th + Ar reaction. The radial parameter r_o is 1.45 which includes the initial deformation of colliding nuclei. In calculating I, the moment of inertia of the DNS, Def is set to 1.4 as the mean value of the initial and the final deformation. The friction constant is thus determined. The calculation results in almost the same friction constant as shown in Fig. 49-(a). The weighted mean value of the averaged friction constant is $(2.4 \pm 0.5) \times 10^{-22}$ MeV·s/fm^2.

As the second case (Case-2), we use the *l*-independent collision model. In the model, the contributions from the far side and from the near side of the target nucleus do not overlap each other and Q(szc) directly indicates the minimum energy loss component of the projectile-like-fragment come from the far side. This assumption is consistent with the grazing condition of the incoming orbit of the collision. Thus we used the -Q-values of the second zero crossing as the values of E_{loss}. Error of E_{loss} is assumed to be that of -Q(szc) deduced from the range-energy relation. The results are summarized in Fig. 49-(b) and weighted mean value is $(1.2 \pm 0.4) \times 10^{-22}$ MeV·s/fm^2.

The other trial to determine the friction constant k is done as Case-3. We used the -Q-values of the largest polarization with negative value as the values of E_{loss}. The results are shown in Fig. 49-(c). The friction constant k deduced in Case-2 is half of the value of Case-1 and k deduced in Case-3 is nearly equal to the k-value of Case-1. Huizenga et al. have reported the friction constant in Xe+Bi reaction as 3×10^{-22} MeV·s/fm^2 (Sc 78) by applying a transport model to the atomic number distribution of

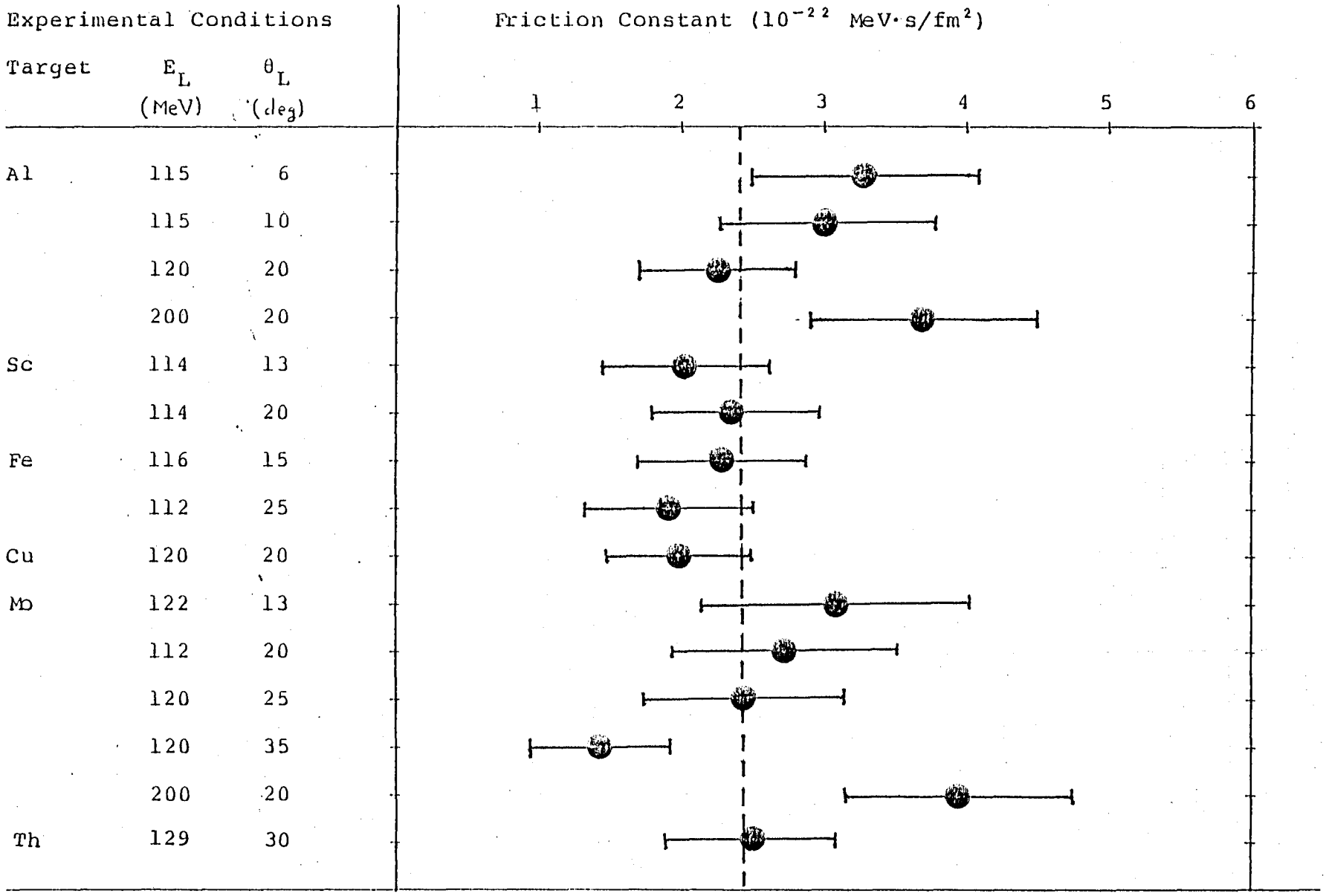

Fig.49-a Experimental results of the friction constant. The values used for E_{loss} are $-(Q(vcf)+Q(szc))/2$. Error bars indicate the kinetic energy windows deduced from the range-energy relation near the second zero crossing. Dashed line indicates the weighted mean value.

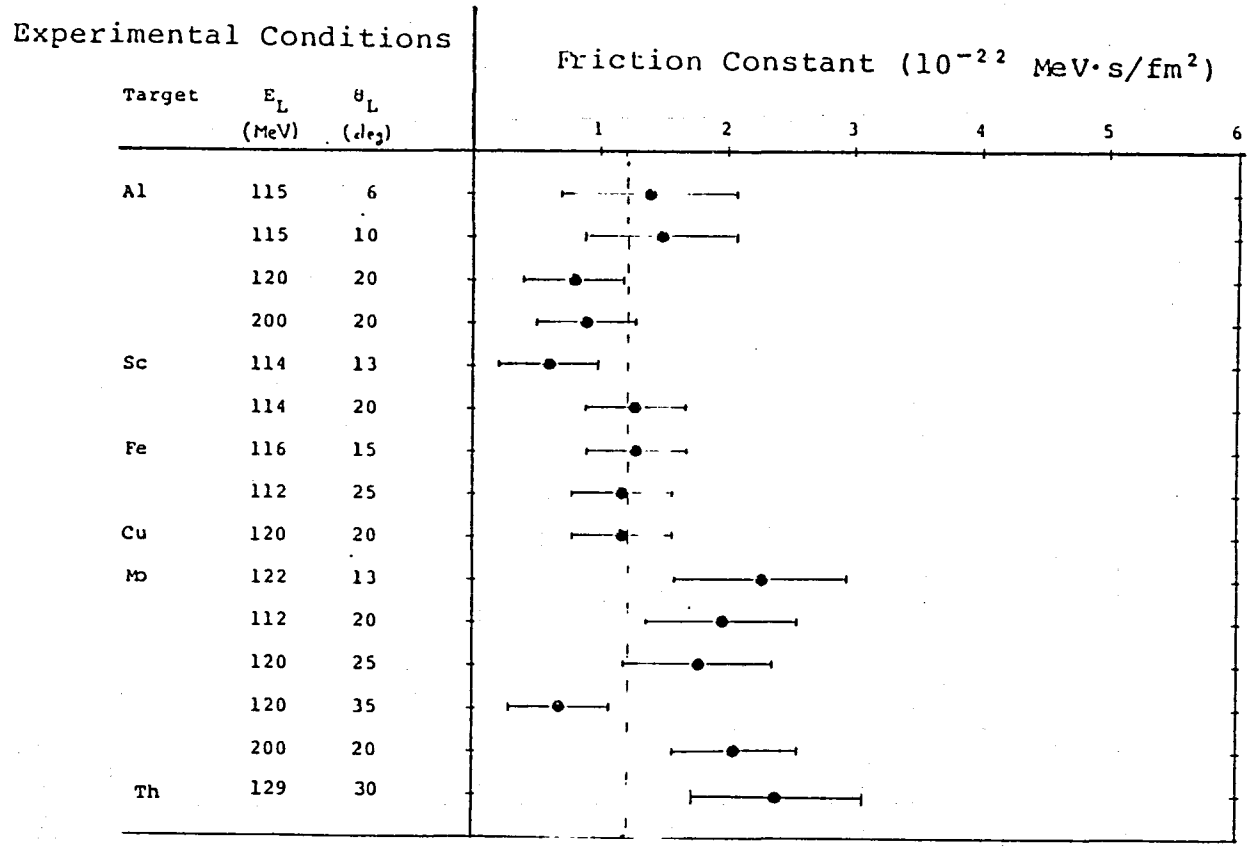

Fig.49-b Experimental results of the friction constant. The values used for E_{loss} are -Q(szc). Error bars indicate the kinetic energy windows deduced from the range-energy relation near the second zero crossing. Dashed line indicates the weighted mean value.

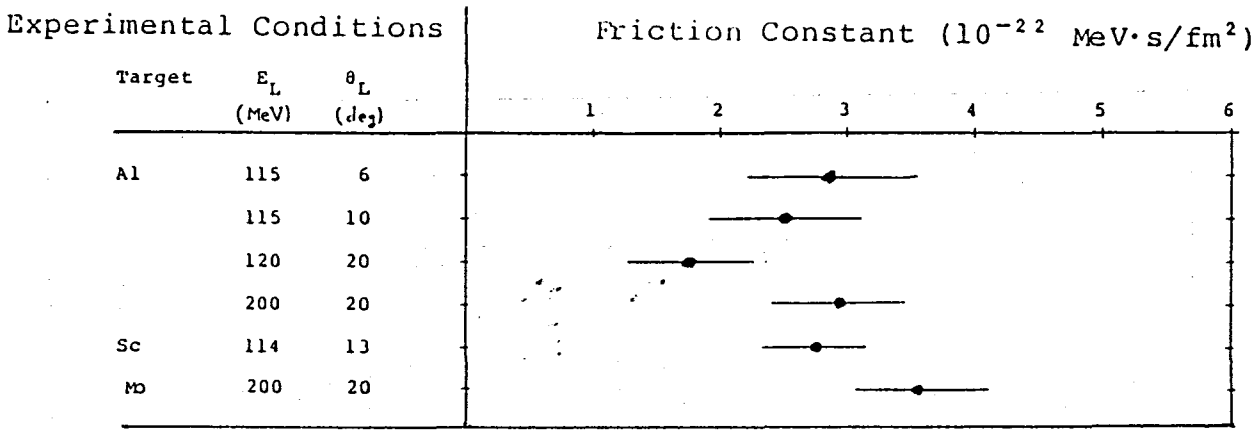

Fig.49-c Experimental results of the friction constant. The values used for E_{loss} are -Q for the largeat negative polarization for Al target at incident energies of 120 and 200 MeV , for Sc target at an incident energy of 120 MeV and for Mo target at an incident energy of 200 MeV. Error bars indicate the kinetic energy windows deduced from the range-energy relation near the largest negative polarization.

projectile-like-fragment. Our value in any case is in a good agreement in the order of magnitude with their value. However our value is somewhat smaller than their value. This difference probably comes from the difference of the overlapping area of DNS formed in the reaction process. The area for the Xe induced reaction is estimated to be 2.3 times larger than for the N induced reaction under the assumption of a proximity potential (Bl 77) as shown in Fig. 50. In the proximity model of nuclear friction, the frictional force is proportional to the area. The friction constant normalized by the overlapping area is about 1.2×10^{-23} MeV·s/fm^4 for Xe + Bi reaction and almost the same value is obtained for ^{14}N induced reactions if we use the friction constant obtained in Case-2.

In the discussion above E_{loss}, the most probable energy loss of projectile-like-fragment from the far side of the target nucleus, is assumed to lie between -Q(szc) and -Q(Vcf) or assumed to be -Q(szc). The calculation started from these assumptions produces the reasonable friction constant which agrees with the results of the other experiments such as Xe + Bi. However, the fluctuation around the mean classical orbit has to be explicitely included in the collision model when we assume that the second zero crossing is a point where the contributions of the projectile-like-fragment from the far side and the near side of the target nucleus are of the same strength.

Recently, Takigawa and co-workers have developed a new time dependent theory of heavy ion collisions called the Quasi-Linear Response Theory, QLRT (Tk 81, Ni 83). They have taken all the higher order terms in the linear response theory for the coupling between the relative motion and the internal excitation of nuclei. The model can treat a fluctuation around the mean

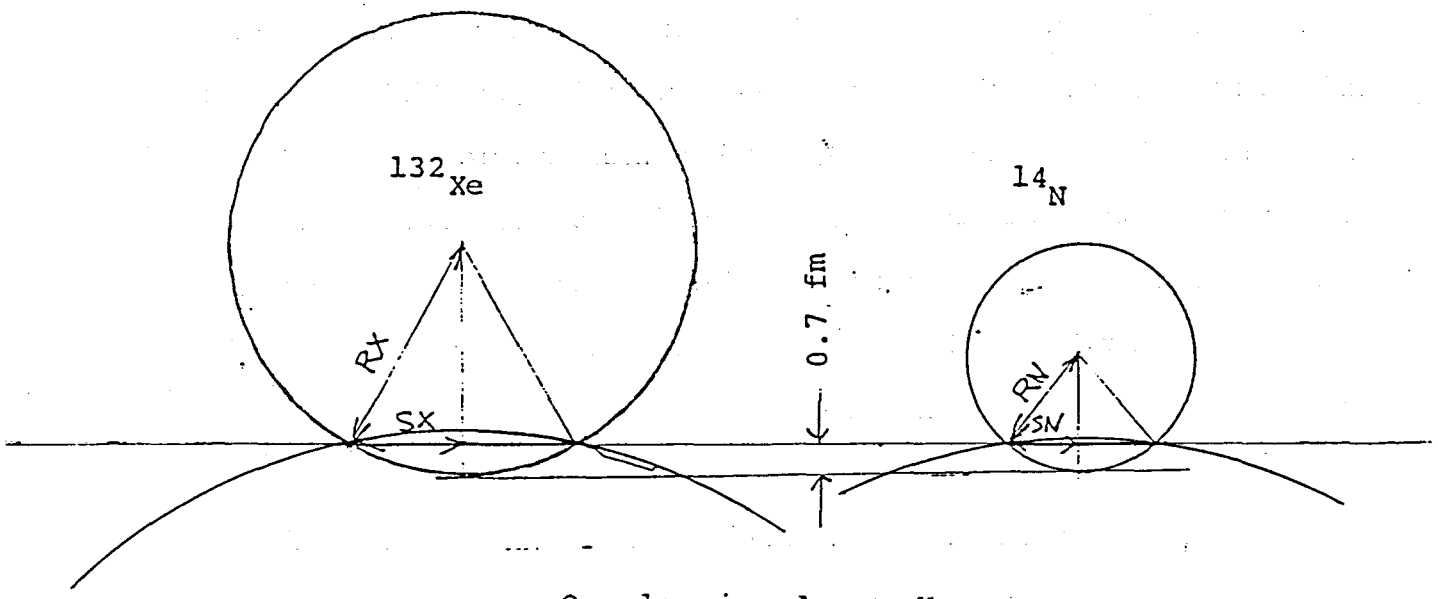

Overlapping Area: Xe

$$\pi(SX)^2 = \pi((RX)^2 - (RX-0.7)^2)$$
$$= \pi(1.4RX - 0.5)$$
$$= \pi(1.4\ (1.15\ (132)^{1/3}) - 0.5)$$
$$= 7.7\pi fm^2$$

Overlapping Area: N

$$\pi(SN)^2 = \pi((RN)^2 - (RN-0.7)^2)$$
$$= \pi(1.4RN - 0.5)$$
$$= \pi(1.4\ (1.15\ (14)^{1/3}) - 0.5)$$
$$= 3.4\pi fm^2$$

Ratio of area; $\dfrac{\pi(SN)^2}{\pi(SX)^2} = 0.44$

Fig.50 A comparison of an ^{14}N induced reaction to a ^{132}Xe induced reaction with respect to the overlapping area of the di-nuclear system.

trajectory and has successfully reproduces double differential cross sections for heavy ion reactions (Wilczynski plot) for various combination of projectile and target.

The model was applied to the ^{14}N induced reactions. Parameters used in the calculation is almost the same as those used in the heavy-ion reactions with heavy projectiles such as Ar, Xe and Pb (Ni 83)(See Appendix). A comparison of the QLRT calculation with the experimental results of ^{14}N induced reactions are shown in Fig. 51. The experimental data were taken from ref.(Fu 81). The results from the QLRT calculation were in a good agreement with the experimental data except in the region of small energy loss where the direct reaction process is dominant.

By modifying the QLRT, the ^{12}B polarization was calculated. The definition of the polarization is given in Eq. (4-3). The σ_+ and the σ_- were calculated by use of QLRT and P and σ were obtained from the subtruction and the summation of the σ_+ and the σ_-. The results of the QLRT calculation are shown in Fig.52. The calculated second zero crossing as a function of A, the mass number of the target, is shown in Fig.52-a. Typical calculated values of ^{12}B polarization as functions of the reaction Q-value and reaction angle are shown in Fig.52-(b-p).

The shift of the second zero crossing as a function of A was well reproduced by QLRT and signs of the polarization as a function of reaction Q-value are also in a good agreement with the measured polarization except in the region of small energy loss with heavy targets. The polarization in the region of small energy loss with heavy targets reflects direct processes. These facts mean that the main properties of the ^{12}B polarization surely reflects frictional processes of heavy ion reactions and the assumption about the second zero crossing is also well verified. However the value of the

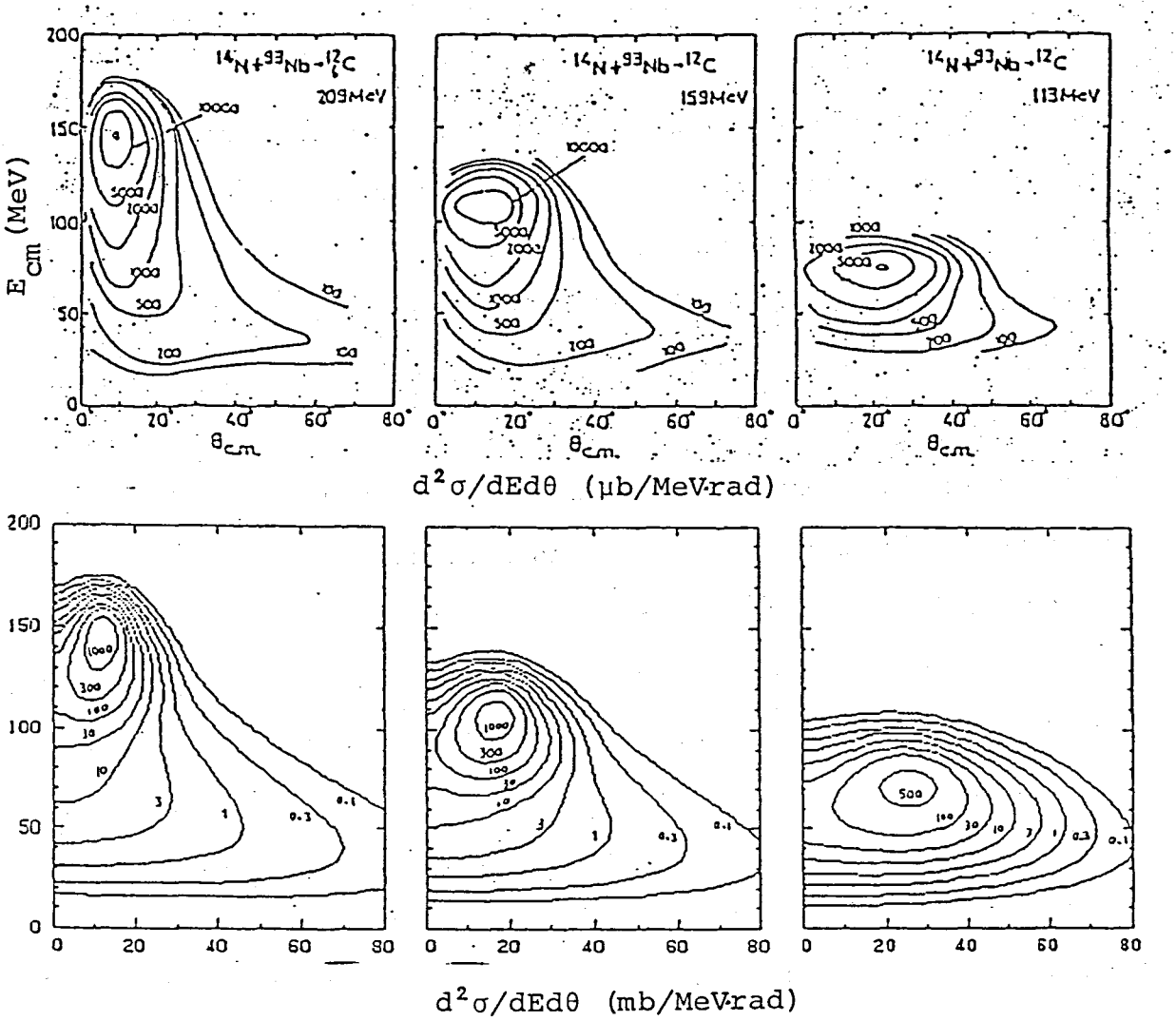

Fig.51 Comparison of experimental results with the QLRT calculation. The experimental results of the double differential cross sections of a ^{14}N induced reaction are taken from ref. (Fu 81).

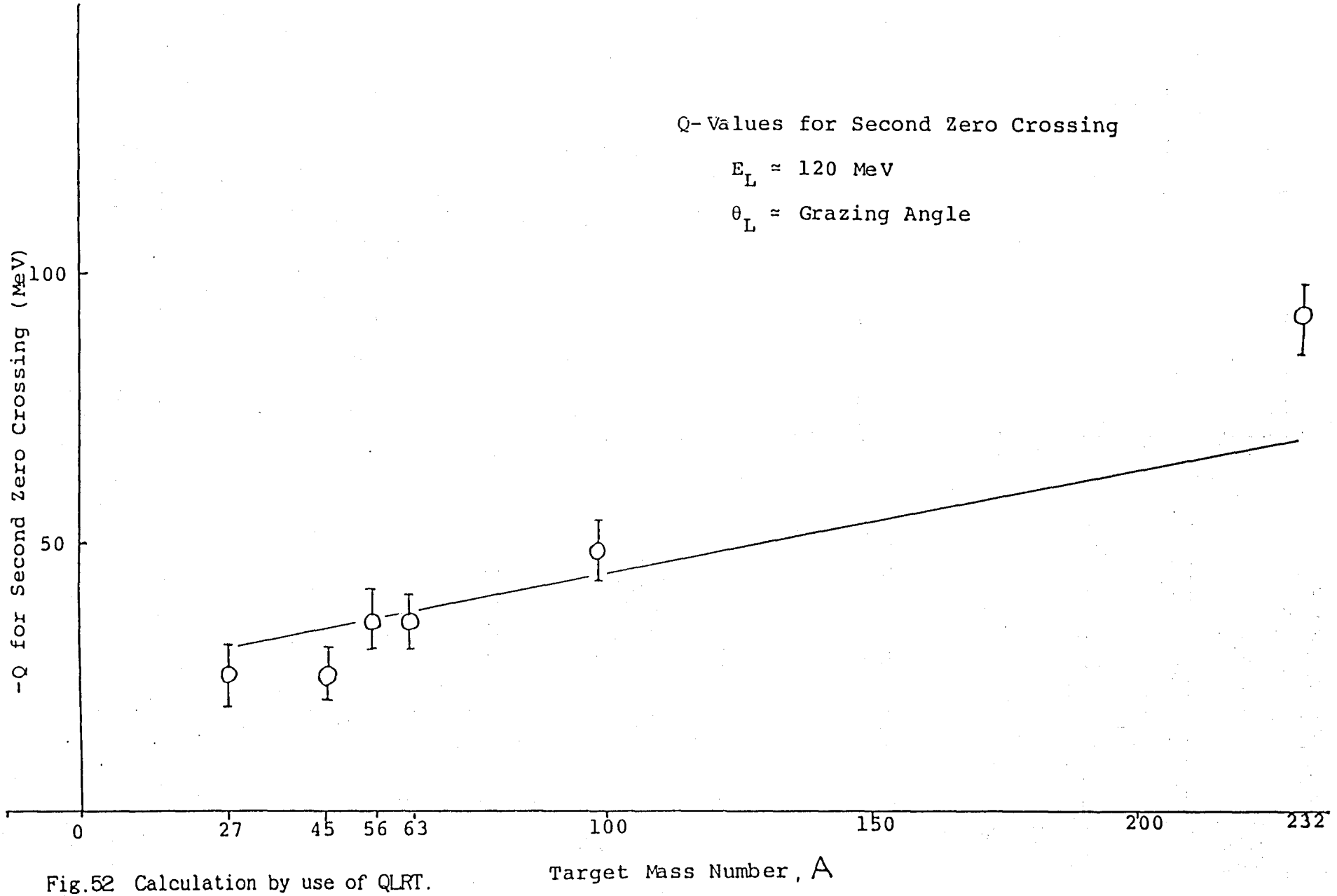

Fig.52 Calculation by use of QLRT.

-a The second zero crossing as a function of A (Solid line). The experimental values of the second zero crossing are also indicated in the figure.

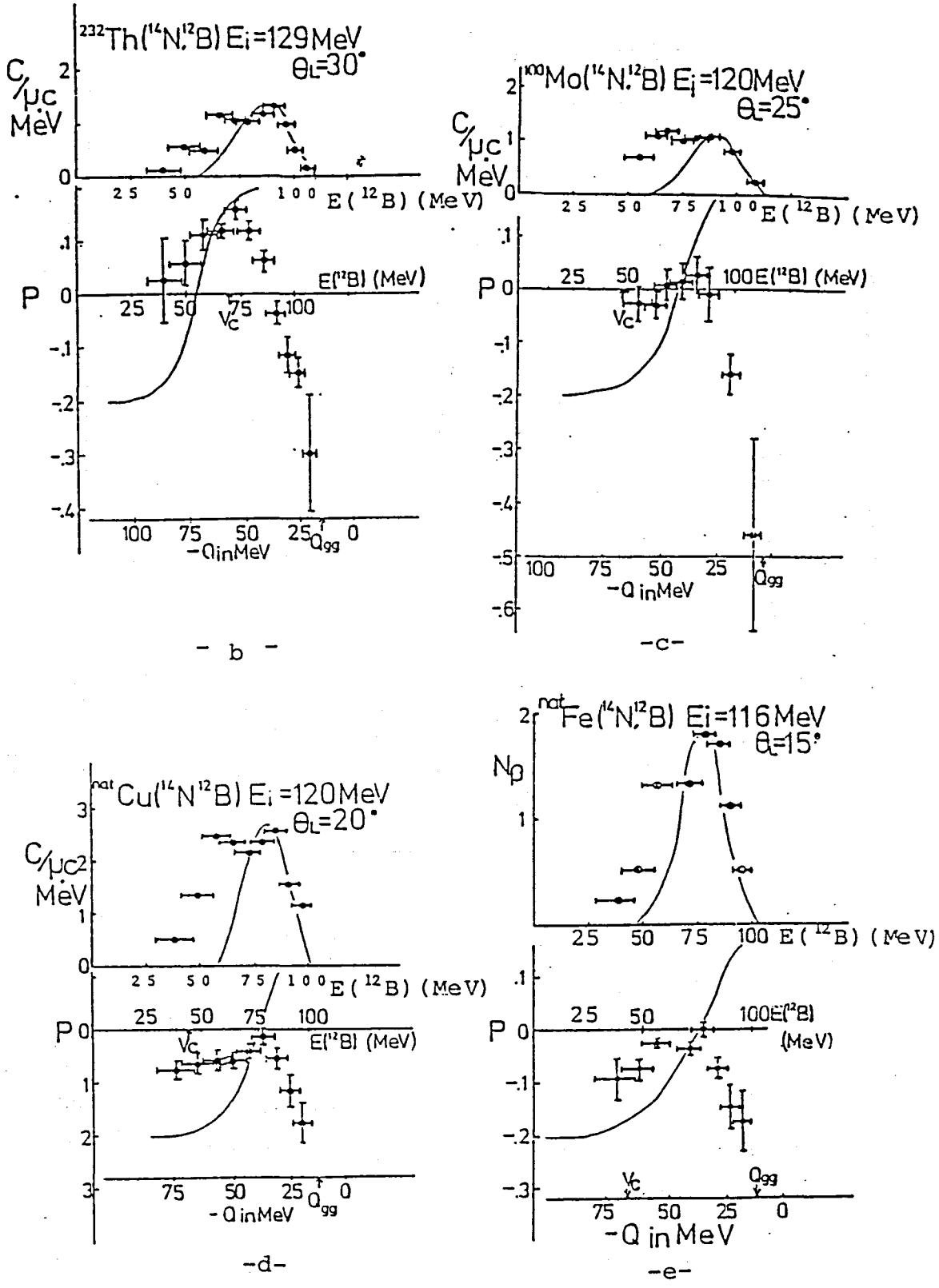

Fig.52 (b-p) Calculation by use of QLRT. The spin polarization and the energy spectrum of ^{12}B as a function of the reaction Q-value. A factor 0.2 is multiplied on the theoretical value of the polarization.

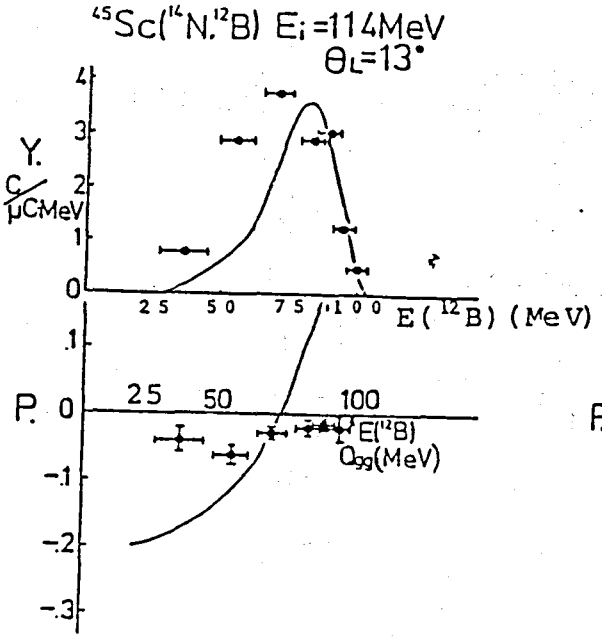

-f-

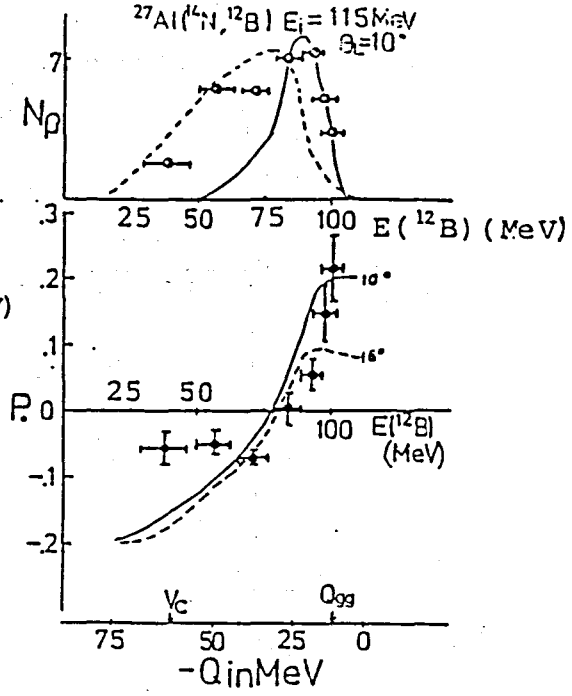

-g-

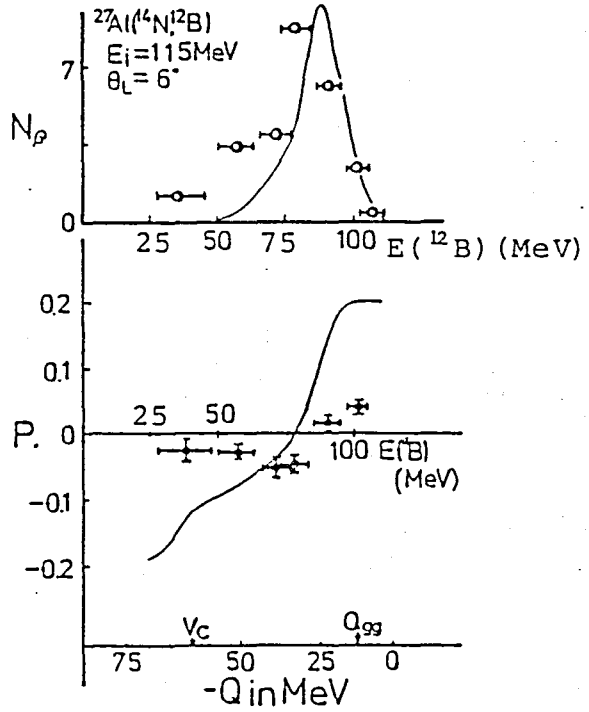

-h-

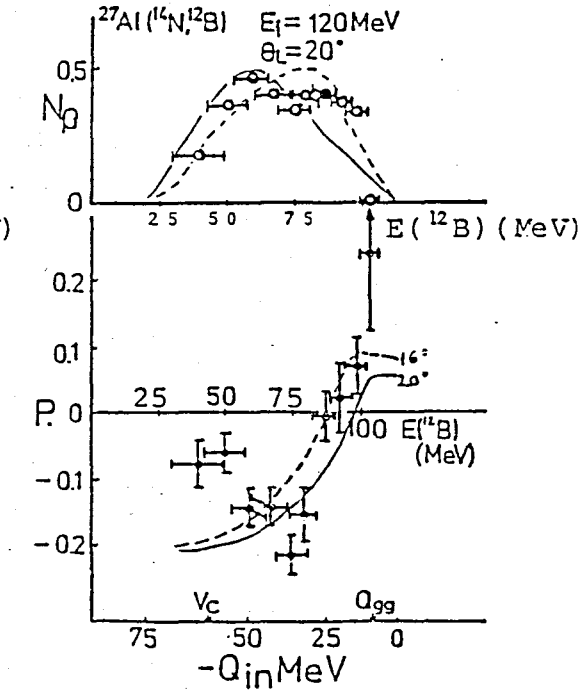

-i-

Fig.52 (b-p) Calculation by use of QLRT. The spin polarization and the energy spectrum of ^{12}B as a function of the reaction Q-value. A factor 0.2 is multiplied on the theoretical value of the polarization.

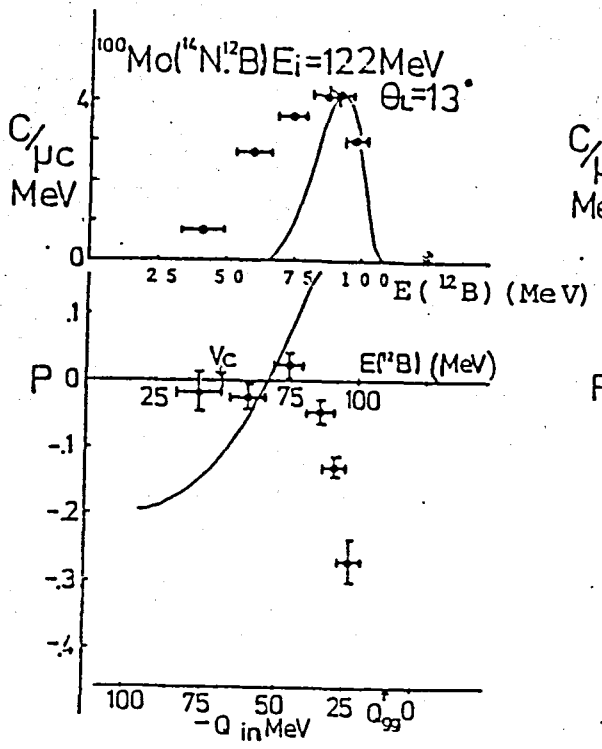

-j-

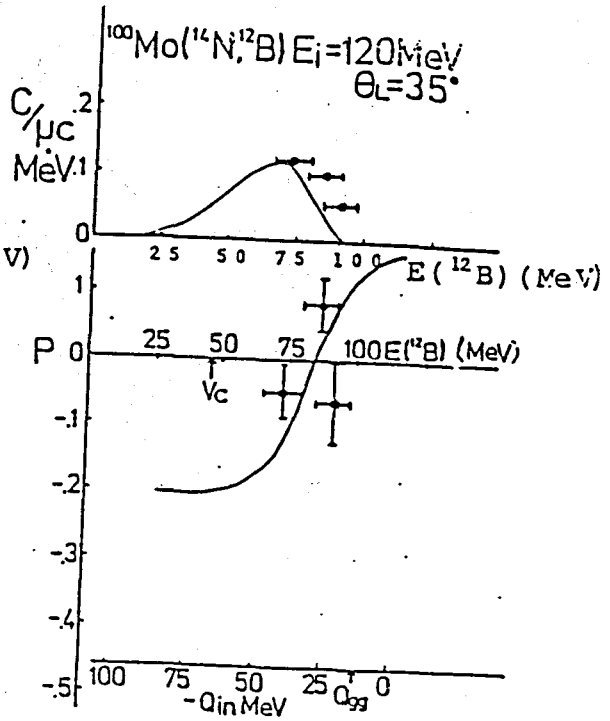

-k-

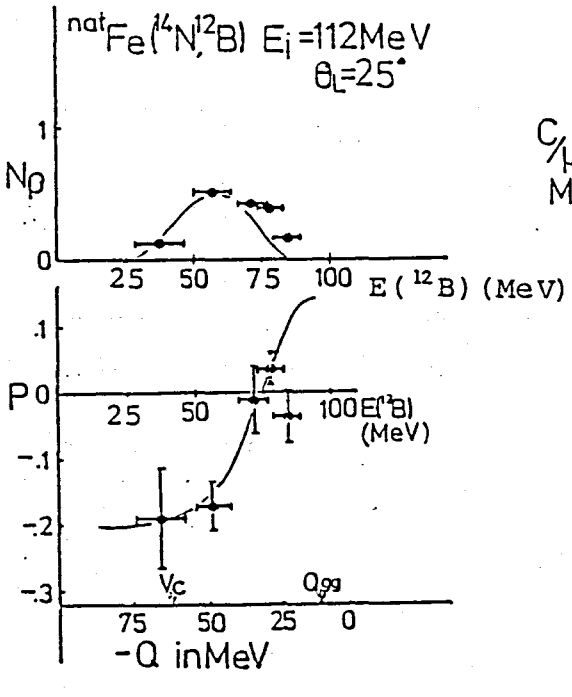

-l-

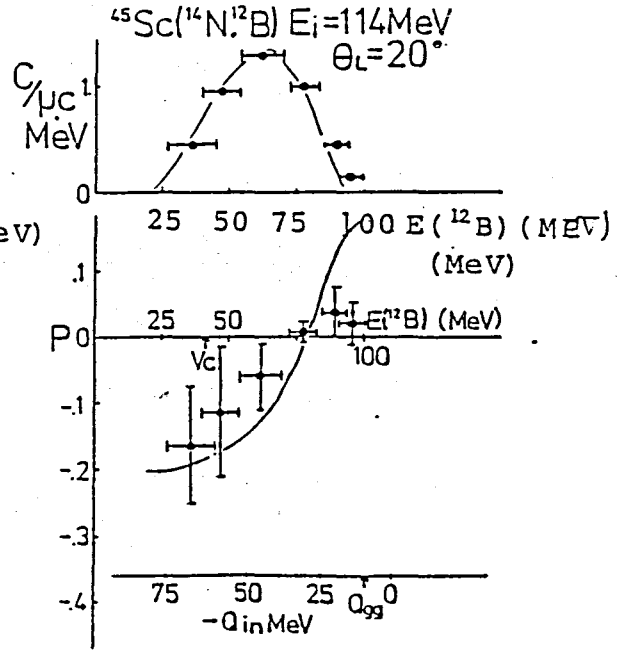

-m-

Fig.52 (b-p) Calculation by use of QLRT. The spin polarization and the energy spectrum of ^{12}B as a function of the reaction Q-value. A factor 0.2 is multiplied on the theoretical value of the polarization.

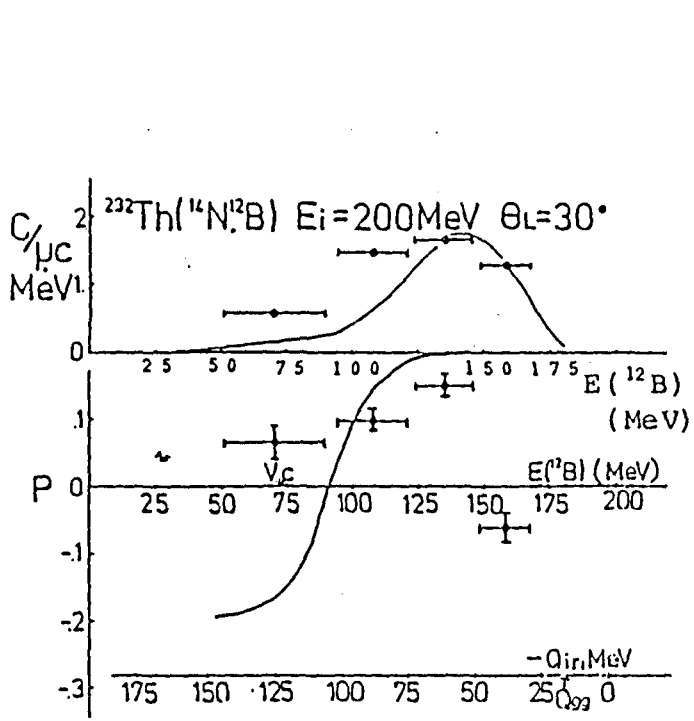

-n-

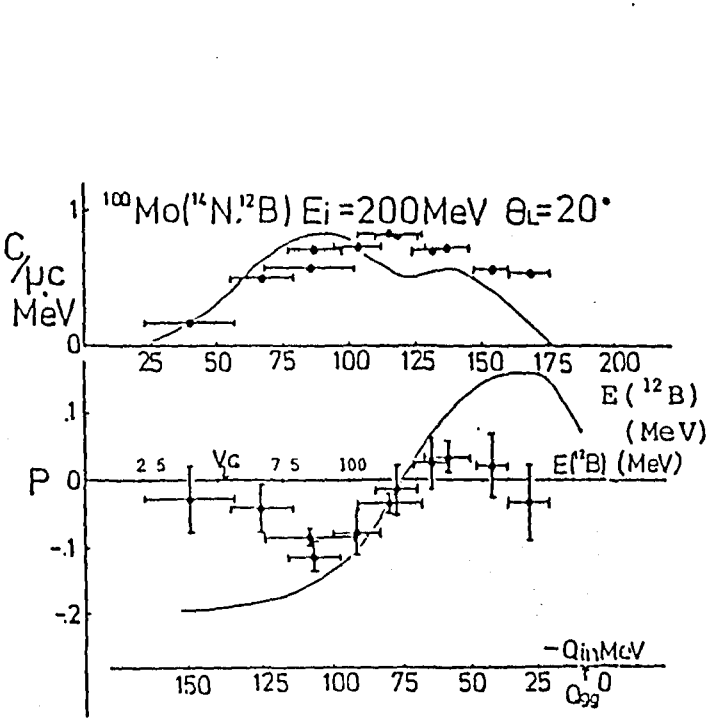

-o-

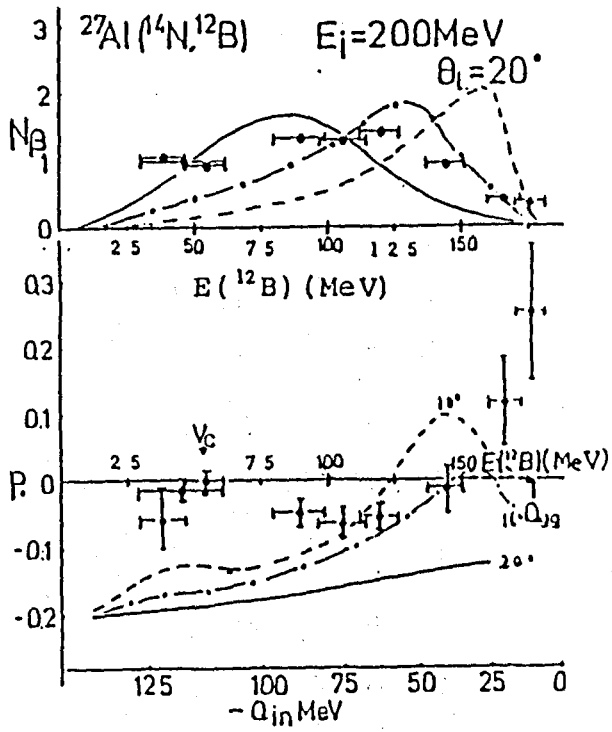

-p-

Fig.52 (b-p) Calculation by use of QLRT. The spin polarization and the energy spectrum of ^{12}B as a function of the reaction Q-value. A factor 0.2 is multiplied on the theoretical value of the polarization.

measured polarization is about one half the calculated value even if the possible depolarization parameter, R_{dep}, introduced in Chap. 3, is multiplied on the calculated value. This fact suggests that some depolarization mechanism exists in the heavy-ion collision process.

In the framework of QLRT, the microscopic description of the nuclear friction force is explicitly given. The friction force indicates the strength of the coupling interaction between the relative motion and the internal degree of freedom and depends on the level density of interacting nuclei.

Note that R.Reif and co-workers also applied a friction model including statistical fluctuations (Sc 81, Re 82) to the ^{14}N induced reactions and suceeded to reproduce the present experimental results of polarization.

4-2-b Coexistence of the different reaction mechanisms

As mentioned in section 4-1, the variation of ^{12}B polarization at the region of small energy loss suggests the coexistence of two different reaction mechanisms. One is a frictional process with positive polarization and the other is a direct two proton transfer process with negative polarization.

Contribution of the frictional process becomes large at backwards angles and for light nuclei since the characteristic negative polarization due to the direct two proton transfer shifts to the positive direction or completely disappears. The change of the contribution of a frictional process and a direct process as a function of scattering angle means that the angular distributions of these two processes are different. Both the direct two proton transfer process and the frictional process occur along a grazing trajectory in the region of small energy loss. However the direct process distributes at a more forward scattering angle than that of the frictional process. Then the contribution from a direct process becomes relatively small at the backward angle and the polarization is shifted to a positive value due to the relatively large contribution of the frictional process with its positive polarization.

When the target is as light as ^{27}Al, the polarization due to the direct process is not observed even in the forward angle such as 6 deg. in lab.system. The grazing angle is small for light target and the contribution from the negative-angle deflection process becomes large. The polarization obtained at the forward angle is strongly attenuated by the contribution from the opposite side of the target nucleus. The direct process is distributed at a more forward scattering angle than that of the frictional process, the polarization from the direct process is strongly attenuated by that from the

frictional process. Then the polarization due to the frictional process becomes dominant even for the least energy loss in light target.

The ratio of the contributions from both collision processes can be estimated from the experimental results. By assuming a constant positive polarization P in the frictional process and a polarization rising linearly with Q, the slope of which is $\zeta = \Delta P/\Delta Q = 0.02$, in the direct process, the Q-value of the first zero crossing Q_1 is

$$Q_1 = Q_0 + \frac{a}{b\zeta} P, \qquad (4\text{-}21)$$

where Q_0 is the Q-value of the first zero crossing of a pure direct process, 'a' and 'b' are the ratios of the contributions from the frictional process and the direct process and normalized as a+b=1. The value of P is chosen as 0.15 because this value of polarization was observed in the region of small energy loss for ^{27}Al near the grazing angle.

The ratio 'a' is determined by fitting the equation above to the experimental results from the shift of the first zero crossing as a function of scattering angle for ^{100}Mo target as shown in Fig. 53. The contribution from the frictional process is found to be about 70 % at the scattering angle of 35 deg. to explain the shift of the first zero crossing.

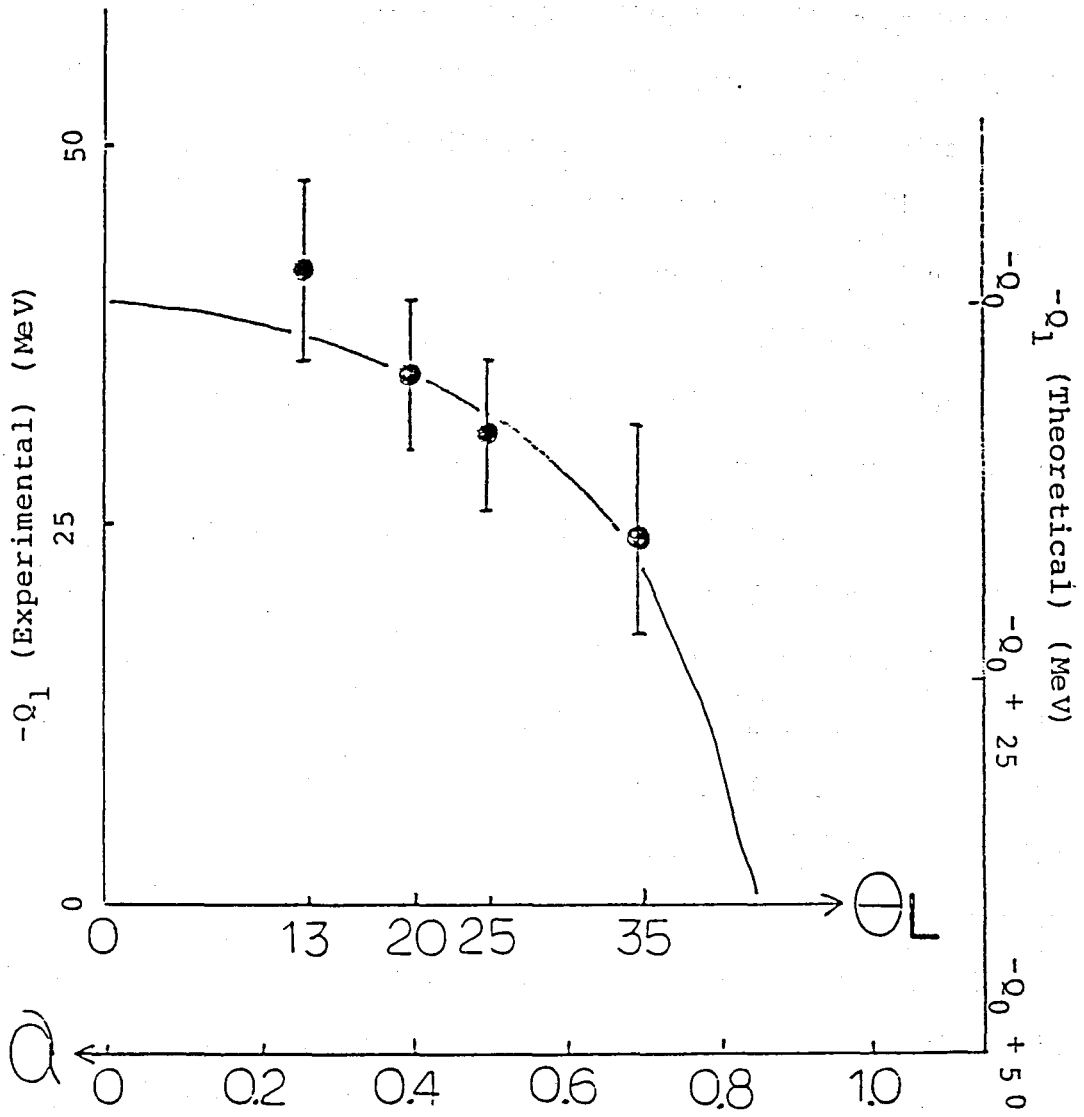

Fig.53 Experimental Q-values of the first zero crossing as a function of the scattering angle for ^{100}Mo. The curve is calculated under the assumption of coexistence of frictional and direct processes.

4-2-c Comparison with the other experiments

The γ ray circular polarization method was also used in measuring the polarization of the projectile-like-fragment. Trautmann et al. have observed the circular polarization of γ rays emitted from projectile-like-fragments. The reactions which they studied were Ni(^{16}O,O) and Ni(^{16}O,C). The incident energy of ^{16}O was about 100 MeV(Tr 80).

By using a particle-γ coincidence technique, the γ rays from 2^+ to 0^+ states in ^{12}C and from 3^- to 0^+ states in ^{16}O were separated from continuous γ ray background. The circular polarization of the γ rays from these transitions was measured and the spin polarization of ^{12}C and ^{16}O was determined. The circular polarization of continuous γ rays was also measured and the observed polarization was from target-like-fragments.

Their results are shown in Fig. 54. When comparing with our results, a similar polarization of the projectile-like-fragments is seen in the alpha transfer channel. In the region of small energy loss, the sign of the polarization is negative, which corresponds to the direct cluster transfer process. The sign of the polarization becomes positive with an increase in kinetic energy loss and returns to a negative value for large energy loss. A similarity to our results becomes more clear by comparison with our result for ^{nat}Cu. However, in the inelastic channel, the polarization is somewhat different from that of the transfer channel. The polarization is very similar to our results for ^{27}Al. The polarization is positive in the region of small energy loss and becomes negative with the increase of the kinetic energy loss. In the inelastic channel, the polarization which corresponds to the direct cluster transfer was completely suppressed and the trend of the polarization can be explained solely by a frictional process. The polarization of target-like-fragments is independent of the reaction channel

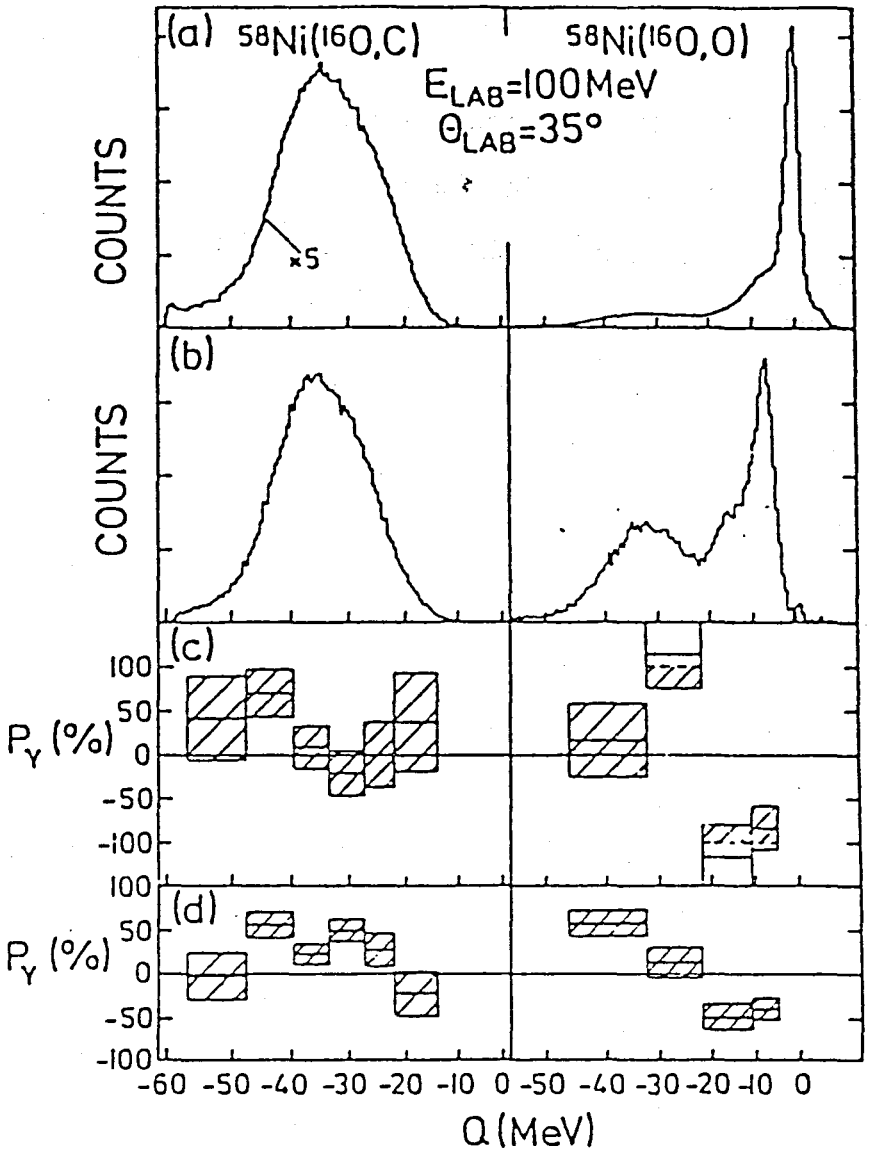

(a) Free particle spectra,
(b) spectra of particles coincident with γ-rays of E_γ>2 MeV,
(c) circular polarization of the 4.44 MeV (^{12}C,2+0) and 6.13 MeV (^{16}O,3+0) transition on the left and right, respectively,
(d) polarization of the continuum with E_γ>3 MeV

Fig.54 Experimental results of circular-polarization of γ rays emitted from the projectile-like and the target-like fragments in heavy-ion reaction (Tr 80). Their sign of polarization is inverse against our convention.

and fully explained by the frictional process.

The polarization measured by the γ ray method also indicates the frictional reaction process and the direct transfer process, which agrees with our measurements by use of β-ray asymmetry.

CHAPTER 5

Conclusion

Nuclear spin polarization of ^{12}B produced in (^{14}N, ^{12}B) reactions was measured for various targets at various scattering angle and with various incident energies. The systematic behaviour of the polarization was observed and can be understood within the framework of the classical frictional model for heavy-ion reaction: The sign of the polarization depends mainly on the sign of the deflection angle and a classical trajectory can be established from a frictional reaction mechanism.

A microscopic model of heavy-ion reaction, QLRT, well reproduced the experimental results of the polarization. This success suggests that the phenomeological nuclear friction force will be described by combining the microscopic nucleon-nucleon interaction and the statistical dynamics.

A polarization which was yielded from the direct two proton transfer process was also observed in the region of small energy loss for heavy targets. However this was strongly suppressed in light nuclei; here the main variation of the polarization was explained exclusively by frictional model. This change in polarization means coexistence of a frictional and a direct processes in the region of small energy loss. The polarization from the frictional process appeared in the region of small energy loss where the polarization from the direct process existed, because the interaction time and the energy loss in the frictional process were smaller for light target

than that for heavy targets. The sign of the polarization at the region of small energy loss is determined by a balance between contributions from the direct process and the frictional process.

CHAPTER 6

Proposals for continuing research

There are many directions in which a continuation and extension of this work can be fruitfully pursued; some of these are stated below.

One approach is to study the other reaction channels. For example, the reaction channel ($^{12}C,^{12}B$) is interesting. The direct two proton transfer process is suppressed except for a charge exchange process. Although the exchange process presumably contributes to a small degree to the total reaction cross section as seen from the cross section data(Yo 75), a frictional process will be more clearly seen, if the exchange channel is examined at higher energies.

Another approach is to measure at higher incident energies. For example, in the reaction induced by an incident ion with energies of few hundred MeV/u, the reaction mechanism evolves from the frictional process at low energies to the projectile fragmentation process (He 72). One can estimate the angular momentum transfer, ΔL, in the heavy ion collision with higher incident energies by use of the following equation.

$$\Delta L = R \int F(t)dt = RF(t)\Delta t, \qquad (6\text{-}1)$$

where R is an impact parameter, F(t) is the force acting along the tangential direction of nuclei and Δt is the interaction time.

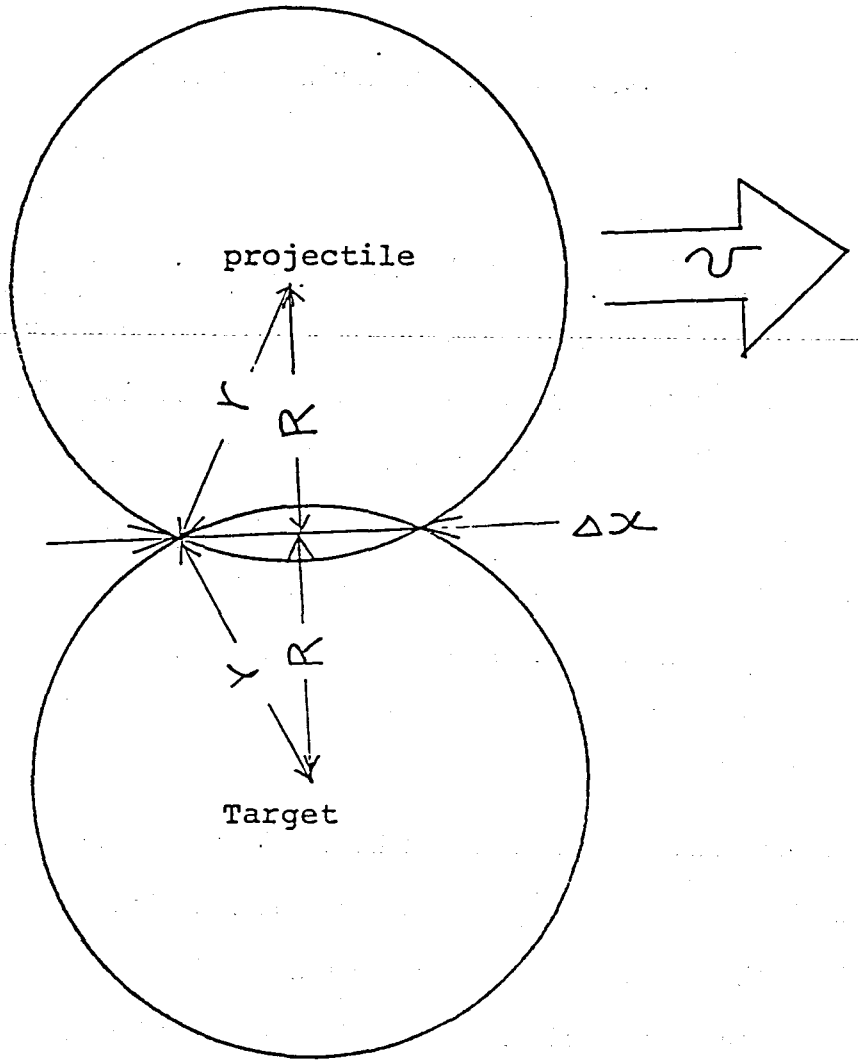

Fig.55 Schematic illustration of heavy-ion collision at relativistic energy.

The interaction time can be estimated from the ratio of interaction size Δx and relative velocity v_{rel} as

$$\Delta t \doteqdot \Delta x / v_{rel}. \qquad (6-2)$$

For the simplification, the radii of the projectile and the target are assumed to be equal value, r. The interaction size is estimated from the overlapped area of each nucleus written as (See Fig.45)

$$\Delta x = 2\sqrt{r^2 - R^2}. \qquad (6-3)$$

If the interaction is explained in terms of a nuclear friction force and the area of the region is proportional to the cross section of the overlapped area of each nucleus, the force can be written by using the friction coefficient determined at low energy as

$$F = \pi(\Delta x)^2 k v_{rel}/(4\Delta S), \qquad (6-4)$$

where ΔS is the cross section of the overlapped area of the di-nuclear system at low energy determined from a proximity potential (Bl 77) as

$$\Delta S = \pi(r^2 - (r - 1.37/2)^2)$$
$$= \pi(1.4r + 0.5). \qquad (6-5)$$

Then the angular momentum transfer is

$$\Delta L(\hbar) = 3.4A^{4/3}C(1 - C^2)^{3/2}/(A^{1/3} + 0.3), \qquad (6-6)$$

where $r=1.15 \times A^{1/3}$ (fm) has been employed, A is the mass number of the nucleus and C is defined as R/r.

Some typical results from the numerical calculation follow:

Nuclear Reaction	Transferred Angular Momentum ΔL ($\hbar$)	
	R = 0.5r	R = 0.9r
U + U	251	58
Xe + Xe	138	32
Ar + Ar	41	9
C + C	12	3

Large angular momentum transfer is not expected in light-heavy ion projectile such as ^{12}C. T.Shibata et al. observed a small angular momentum transfer, less than 5 $\hbar$, in relativistic heavy-ion reactions with ^{12}C projectile (Sb 78). This value agrees with the present estimation for R = 0.9r. It will probably be difficult to polarize nuclei at high energies with light-heavy ions like ^{12}C. Heavy projectiles such as uranium have to be used for studying angular momentum transfer in heavy ion collisions with relativistic energy.

Acknowledgement

I would like to express my thanks to Prof. N.Takahashi, Prof. T.Minamisono, Prof. K.Sugimoto, Dr. Y.Nojiri and Dr. K.Asahi for their collaboration, discussion and encouragement throughout the present study.

All the experiments described here were carried out at the Research Center for Nuclear Physics (RCNP), Osaka University, under the program number, 4A-15, 5A-17, 6A-18, 7A-19, 8A-22, 9A-17, 10A-02, 11A-20, 12A-20, 13A-12 and 14A-19. Staff and cyclotron crew of RCNP are highly appreciated for their hospitality and cooperation.

Dr. N.Takigawa and Mr. K.Niita kindly permitted me to use their computer program Quasi-Linear Response Theory (QLRT) for the analysis of the experimental results. A workshop "Analysis of heavy-ion reaction mechanism with Quasi-Linear Response Theory (QLRT)" was held on November 8-10, 1982 under the financial support of RCNP and discussions were held on the theoretical aspects of the reaction mechanism revealed from these experiments.

Prof. H.Ejiri, Prof. H.Ikegami, Prof. K.Katori and Prof. M.Morita read this thesis and gave me invaluable suggestions.

Prof. B.I.Deutch kindly read this thesis and pointed out a lot of incorrect expressions.

Mr. Y. Takahashi and Mr. M. Sakamoto provided technical support.

Dr. Y.Miake helped me in the early stage of the present study.

Discussions with Dr. T.Fukuda, Dr. T.Motobayashi, Dr. T.Shimoda, Dr. M.Noumachi and Dr. H.Ohsumi of the present study were precious.

I thank those who helped me in the various phase of the present study.

The present study was partly supported by the Grant in Aid of Scientific Research, Ministry of Education and by Toray Science and technology Grants.

Appendix

Quasi Linear Response Theory
and
Its Application to Light Heavy-Ion Reactions

A-1 Introduction to Quasi Linear Response Theory (QLRT)

A-2 Modification of QLRT for heavy-ion reactions with light projectiles

A-1 Introduction to Quasi Linear Response Theory (QLRT)

Nuclei in the collision process are under the influence of strong inter-nuclear forces and are largely excited. The nuclear excitation phenomena depends on the energy level density of colliding nuclei and a lot of number of excitation levels concern. Statistical treatments can be applied to describe such collision process (Ho 76, Ho 77). Quasi Linear Response Theory (QLRT) was developed by N. Takigawa and co-workers as a time dependent theory of nuclear interactions in Tohoku University. The basis of the theory was published in ref.(Tk 81) and the application to the experimental data appeared in ref (Ni 83).

In this theory, the excitation process is described as an energy transport from a relative motion to the intrinsic degree of freedom of nuclei by use of a Fokker-Planck equation. The fluctuation of the transport process is involved in it to the higher order terms, instead the conventional linear response theories involve only the first order of the fluctuation.

The fluctuation around the mean classical trajectory is reproduced by the QLRT and the contour plot of the double differential cross section in the E-θ plane (Wilczynski plot) is well reproduced for the reactions Ar + Th, Xe + Bi and Pb + Pb (Ni 83). The spin polarization of projectile-like product is defined as the the difference between the contributions from the near side and the far side of target nucleus and compared with the present experimental data. The basis of QLRT is summarized in the following subsection. Formulae are taken from ref.(Ni 83).

The basic elements of QLRT are excitation-energy dependent friction

force and the higher order effects in the fluctuation process around the mean trajectory. The equations for the mean trajectory of relative motion is given by

$$\frac{d}{dt} P_\alpha(t) = - U^{(\alpha)}(\underset{\sim}{q}(t)) + \mathcal{F}_\alpha(t) \quad , \qquad (A-1)$$

$$\frac{d}{dt} \underset{\sim}{q}(t) = \frac{1}{\mu} \underset{\sim}{P}(t) \quad , \qquad (A-2)$$

with

$$\mathcal{F}_\alpha(t) = \mathcal{F}_\alpha^{(c)}(t) - \gamma_{\alpha\beta}(t)\, \dot{q}_\beta(t) \qquad (A-3)$$

where $\mathcal{F}_\alpha^{(c)}(t)$ is the part of conservative force and $\gamma_{\alpha\beta}$ is the friction tensor that represents the energy dissipation force which is proportional to $q_\beta(t)$. By employing the Weidenmuller's form factor (Ag 77) in the coupling Hamiltonian between the relative and the internal motion, $\gamma_{\alpha\beta}$ is explicitly described as

$$\gamma_{\alpha\beta}(t) = \frac{2}{\hbar} W_0 \left\{ \frac{1}{4} f_0^{(\alpha\beta)}(t) + \delta_{\alpha\beta} \frac{1}{\sigma^2} f_0(t) \right\} \int_{t_0}^{t} d\tau\, (t-\tau)\, \phi^{(1)}(t; t-\tau)$$
$$\times \int_0^\infty dE \int_0^\infty dE' \left(\frac{\sigma(E)}{\sigma(E')} \right)^{1/2} e^{-\frac{1}{2\Delta^2}(E-E')^2} \sin\left\{ (E-E')(t-\tau)/\hbar \right\} P_{E'}(t) \quad , \qquad (A-4)$$

where W_0 and σ are the parameters for the strength and the correlation length, respectively and determined from the one body dissipation theorem as

W_0 = 10 MeV and

σ = 3.5 fm .

The correlation length Δ is estimated by Weidenmuller et al. (Ko 76, Ag 77) as

$$\Delta = 5.6\ a^{-1} + 4.75\ (E/a)^{1/2} \qquad (A-5)$$

where a is the level density parameter. A typical value of Δ is about 12 MeV. f_0 is the form factor normalized equal to the unity at a half density radii where the projectile and the target nuclei coincide. $\sigma(E)$ is the level

density, which is approximately given by

$$\sigma(E) \propto \exp(2aE)^{1/2}. \qquad (A-6)$$

ϕ^1 is the Green function which involves all the higher order terms of the effects from the coupling Hamiltonian. The occupation probability $P_E(t)$ is the solution of

$$\frac{\partial}{\partial t} P_E(t) = \int_{t_0}^{\tau} d\tau \int_0^{\infty} dE' K^{(1)}_{EE'}(t,\tau) \left\{ \sigma(E) P_{E'}(\tau) - \sigma(E') P_E(\tau) \right\}, \qquad (A-7)$$

where $W_{EE'}$ is the transition probability, which is determined from the master equation of energy transport. However the numerical calculation for $P_E(t)$ shows that $P_E(t)$ is well approximated by a Gaussian form with the variance $\sigma_E(t)$ except for the very early stage of the collision.

$\sigma_E(t)$ is

$$\sigma_E(t) = 2^{1/2} a^{-1/4} E^{-3/4} \qquad (A-8)$$

This relation means the canonical distribution with mean excitation energy E.

The fluctuation around the mean trajectory is obtained by using a Fokker- Planck equation for the density operator D_{AW} for the relative motion as

$$\frac{\partial}{\partial t} D_{AW}(\underline{p},\underline{q},t) = \left(-\frac{1}{\mu} p_\alpha \frac{\partial}{\partial q_\alpha} - M^{(0)}_{\alpha\beta} q_\beta \frac{\partial}{\partial p_\alpha} + \frac{1}{\mu} M^{(1)}_{\alpha\beta} \frac{\partial}{\partial p_\alpha} p_\beta \right) D_{AW}(\underline{p},\underline{q},t)$$

$$+ \left(\frac{1}{\mu} N^{(1)}_{\alpha\beta} \frac{\partial^2}{\partial p_\alpha \partial q_\beta} + N^{(0)}_{\alpha\beta} \frac{\partial^2}{\partial p_\alpha \partial p_\beta} \right) D_{AW}(\underline{p},\underline{q},t). \qquad (A-9)$$

where $M^{(n)}$ and $N^{(n)}$ are the n-th order moments of the response and the correlation functions. The zero-th order moment $N^{(0)}$ is determined by a similar equation to Eq. (A-4) as

$$N^{(0)}_{\alpha\beta}(t) = W_0 \left\{ \frac{1}{4} f_0^{(\alpha\beta)}(t) + \delta_{\alpha\beta} \frac{1}{6^2} f_0(t) \right\} \int_{t_0}^{t} d\tau \, \phi^{(1)}(t; t-\tau)$$

$$\times \int_0^{\infty} dE \int_0^{\infty} dE' \left(\frac{6(E)}{6(E')} \right)^{1/2} e^{-\frac{1}{2\Delta^2}(E-E')^2} \cos\left\{ (E-E')(t-\tau)/\hbar \right\} P_{E'}(t), \qquad (A-10)$$

The conventional linear response theory reads

$$N^{(0)}{}_{\alpha\beta}(t) = T(t)\ \gamma_{\alpha\beta}(t) \qquad (A-11)$$

where $T(t)$ is a parameter and means a temperature of the internal excitation.

The mean trajectory and its fluctuation are thus expressed in the θ–r plane as

$$\left.\begin{aligned} \frac{d}{dt}P_r &= -\frac{d}{dr}U(r) + \frac{P_\theta^2}{\mu r^3} + \mathcal{F}_r(t)\ , \\ \frac{d}{dt}P_\theta &= \mathcal{F}_\theta(t)\ , \\ \frac{dr}{dt} &= \frac{P_r}{\mu}\ , \\ \frac{d\theta}{dt} &= \frac{P_\theta}{\mu r^2}\ . \end{aligned}\right\} \qquad (A-12)$$

and

$$\frac{d}{dt}\sigma_{P_rP_r} = N_{rr}^{(0)} - \frac{2}{\mu}\sigma_{P_rP_r}M_{rr}^{(1)} + \frac{4}{\mu r^3}P_\theta\sigma_{P_rP_\theta} - \frac{6}{\mu r^4}P_\theta^2\sigma_{\{P_r r\}}\ ,$$

$$\frac{d}{dt}\sigma_{P_rP_\theta} = -\frac{1}{\mu r^2}\sigma_{P_rP_\theta}M_{\theta\theta}^{(1)} - \frac{1}{\mu}\sigma_{P_\theta P_r}M_{rr}^{(1)} + \frac{2}{\mu r^2}P_\theta\sigma_{P_\theta P_\theta} - \frac{3}{\mu r^4}P_\theta^2\sigma_{\{P_\theta r\}} + \frac{2}{\mu r^3}P_\theta\sigma_{\{P_r r\}}M_{\theta\theta}^{(1)}\ ,$$

$$
\begin{aligned}
\frac{d}{dt}\sigma_{P_\theta P_\theta} &= N_{\theta\theta}^{(0)} - \frac{2}{\mu r^2}\sigma_{P_\theta P_\theta} M_{\theta\theta}^{(1)} + \frac{4}{\mu r^3} P_\theta \sigma_{\{P_\theta r\}} M_{\theta\theta}^{(1)}, \\
\frac{d}{dt}\sigma_{\{P_r r\}} &= \frac{1}{\mu}\sigma_{P_r P_r} - \frac{1}{\mu}\sigma_{\{P_r r\}} M_{rr}^{(1)} + \frac{2}{\mu r^2} P_\theta \sigma_{\{P_\theta r\}} - \frac{3}{\mu r^4} P_\theta^2 \sigma_{rr}, \\
\frac{d}{dt}\sigma_{\{P_r \theta\}} &= \frac{1}{\mu r^2}\sigma_{P_\theta P_r} - \frac{1}{\mu}\sigma_{\{P_r \theta\}} M_{rr}^{(1)} - \frac{2}{\mu r^3} P_\theta \sigma_{\{P_r r\}} + \frac{2}{\mu r^3} P_\theta \sigma_{\{P_\theta \theta\}} - \frac{3}{\mu r^4} P_\theta^2 \sigma_{r\theta}, \\
\frac{d}{dt}\sigma_{\{P_\theta r\}} &= \frac{1}{\mu}\sigma_{P_r P_\theta} - \frac{1}{\mu r^2}\sigma_{\{P_\theta r\}} M_{\theta\theta}^{(1)} + \frac{2}{\mu r^3} P_\theta \sigma_{rr} M_{\theta\theta}^{(1)}, \\
\frac{d}{dt}\sigma_{\{P_\theta \theta\}} &= \frac{1}{\mu r^2}\sigma_{P_\theta P_\theta} - \frac{1}{\mu r^2}\sigma_{\{P_\theta \theta\}} M_{\theta\theta}^{(1)} + \frac{2}{\mu r^3} P_\theta \sigma_{\theta r} M_{\theta\theta}^{(1)} - \frac{2}{\mu r^3} P_\theta \sigma_{\{P_\theta r\}}, \\
\frac{d}{dt}\sigma_{rr} &= \frac{2}{\mu}\sigma_{\{P_r r\}}, \\
\frac{d}{dt}\sigma_{r\theta} &= \frac{1}{\mu}\sigma_{\{P_r \theta\}} + \frac{1}{\mu r^2}\sigma_{\{P_\theta r\}} - \frac{2}{\mu r^3} P_\theta \sigma_{rr}, \\
\frac{d}{dt}\sigma_{\theta\theta} &= \frac{2}{\mu r^2}\sigma_{\{P_\theta \theta\}} - \frac{4}{\mu r^3} P_\theta \sigma_{r\theta}.
\end{aligned}
\qquad (A-13)
$$

where $\sigma_{\alpha\beta}$ are the half variances. The double differential cross section is thus described as

$$
\frac{d^2\sigma}{dE_f\, d\theta_f} = \sum_n \left\{ \left(\frac{d^2\sigma}{dE_f\, d\theta_f}\right)_{n+} + \left(\frac{d^2\sigma}{dE_f\, d\theta_f}\right)_{n-} \right\}, \qquad (A-14)
$$

where

$$
\begin{aligned}
\left(\frac{d^2\sigma}{dE_f\, d\theta_f}\right)_{n\mp} &= 2\pi v_f^{-1} \int_0^\infty b\,db\, \frac{1}{4\pi\sqrt{D}} \exp\left\{ -\frac{1}{4D}\left[(\theta_f \mp \theta(b) + 2n\pi)^2 \sigma_{P_r P_r}(b) \right.\right. \\
&\left.\left. \mp 2(\theta_f \mp \theta(b) + 2n\pi)(P_f - P(b))\sigma_{\{P_r \theta\}}(b) + (P_f - P(b))^2 \sigma_{\theta\theta}(b) \right] \right\},
\end{aligned}
\qquad (A-15)
$$

with $P_f/2\mu = E_f$ and $v_f = P_f/\mu$. $\theta(b)$, $p(b)$ and $\sigma(b)$ are the values of $\theta(t)$, $p(t)$ and $\theta(t)$ at $t = +\infty$ for a given impact parameter b. The sufixes + and − mean the contributions from the near side and from the far side of target nucleus, respectively, and D is defined as

$$D = \sigma_{p,p_r}(t)\,\sigma_{\theta\theta}(t) - \left(\sigma_{\{p,\theta\}}(t)\right)^2, \qquad (A-16)$$

The potential used in the QLRT is time depend potential developed by Norenberg et al. (No 79, No79a, Gn 81)as

$$U(r,t) = U_1(r)\chi + U_2(r)(1-\chi) \qquad (A-17)$$

with

$$\chi(t) = \exp(-t/\tau) \qquad (A-18)$$

τ is the parameter and is 5×10^{-22} sec and U_1 is (Ng 75)

$$U_1 = (A_1A_2)^{1/3}/(A_1^{1/3} + A_2^{1/3})\, V_N(s) \qquad (A-19)$$

$$V_n(s) = -V_o\exp(-0.27s^2) \qquad (s \geqq 0) \qquad (A-20)$$

$$-V_o + 6.3s^2 \qquad (s < 0)$$

where $s = r - r_o(A_1^{1/3} + A_2^{1/3})$ and $V_o = 30$ MeV, $r_o = 1$fm.

U_2 is (Si 78), $U_2 = -U_o/(1 + \exp((r-C_1-C_2)/a)$ (A-21)

where

$$U_o = 17(A_1^{2/3} + A_2^{2/3} - (A_1 + A_2)^{2/3}) \qquad (A-22)$$

$$a = (C_1 + C_2)U_o/16\pi\gamma C_1C_2$$

$$C_i = R_i - b^2/R_i \qquad (i = 1, 2)$$

$$R_i = (1.28A_i^{1/3} - 0.76 + 0.8A_i^{-1/3})\ \text{fm}$$

$$\gamma = 0.9517\,(1-1.7826(1-2(Z_1+Z_2)/(A_1 + A_2))^2\,)$$

$$b = 1\ \text{fm}$$

In the calculation, parameters used are:

(1) The initial half variance, $\sigma_{\alpha\beta}$

$\sigma_{\alpha\beta} = 7$ MeV for all σ.

(2) The initial excitation energy E_o

E_o = 10 MeV.

If an excitation energy is lower than 10 MeV, the values of $\gamma_{\alpha\beta}$ and $N^{(0)}{}_{\alpha\beta}$ used are these at $E = E_o$

(3) The level density parameter 'a' is

$a = (A_1 + A_2)/24$.

The value of 'a' is one third of the conventional value for reproducing the realistic energy transport.

(4) The initial time t = 0 is the point where $r = C_1 + C_2 + 5$ (fm).

A-2 Modification of QLRT for heavy-ion reactions with light projectiles

The QLRT well reproduced the double differential cross section for various collisions between heavy-ions as Xe + Bi, Ar + Th and Pb + Pb. However in heavy-ion reaction as N +Al, the theory had not been applied because the theory could not treat the mass transfer degree of freedom which played an kinematically important role in light heavy-ion reaction. K. Niita first tried to apply the theory to heavy-ion reactions with light projectile and showed that the theory was powerful enough to reproduce the experimental result with light heavy-ion projectiles but some modifications were added in the application. These are as follows.

1) In transfer reaction such as $(^{14}N, ^{12}B)$, the reaction product which had the same energy per nucleon was considered as a "projectile".

2) The kinetic energy of reaction product was cut at its Q_{gg}-value in order to reject the contribution from the elastically scattered "projectile".

3) The correlation length, σ was replaced by the mass dependent form as $\sigma = 0.65\ (A_1 + A_2)^{1/3}$ (fm) which was the constant 3.5 fm in ref. (Ni 83).

The other parameters and formalisms were not changed.

The computer program QLRT which involves the modifications described above is available at Tohoku Univ. and RCNP, Osaka Univ.

References

(Ag 77) D.Agassi, C.M.Ko and H.A.Weidenmüller, Ann. of Phys., 107(1977) 140

(Ar 71) A.G.Artukh, V.V.Avdeichikov, J.Ero, G.F.Gridnev, V.L.Mikheev, V.V.Volkov and J.Wilczynski, Nucl.Phys., A160(1971)511

(Ar 73) A.G.Artukh, G.F.Gridnev, V.L.Mikheev, V.V.Volkov and J.Wilczynski, Nucl.Phys., A215(1973)91

(Be 73) R.Beck and D.H.E.Gross, Phys.Lett., 47B(1973)143

(Bi 77) K.Van Bibber, R.Ledoux, S.G.Steadman, F.Videbaek, G.Young and, C.Flaum, Phys.Rev.Lett., 38(1977)334

(Bl 77) J.Blocki, J.Randrup, W.J.Swiatecki and C.F.Tsang, Ann. of Phys., 105(1977)427

(Br 72) D.M.Brink, Phys.Lett., 40B(1972)37

(Bo 74) J.P.Bondorf, M.I.Sobel and D.Sperber, Phys.Rep., 15(1974)83

(Ch 68) L.F.Chase, Jr, R.E.McDonald, W.W.True and E.K.Warburton, Phys.Rev., 166(1968)997

(Co 80) M.T.Collins, J.J.Griffin, Nucl.Phys., A348(1980)63

(Dy 77) P.Dyer, R.J.Puigh, R.Vandenbosch, T.D.Thomas and M.S.Zisman, Phys.Rev.Lett., 39(1977)392

(Fu 81) T.Fukuda, M.Tanaka, M.Ishihara, H.Ogata, I.Miura and H.Kamitubo, Phys.Lett., 99B(1981)317

(Ga 70) J.Galin, D.Guerreay, M.Lefort, J.Peter, T.Tarrago and R.Basile, Nucl.Phys., A159(1970)461

(Ge 77) C.K.Gelbke, C.Olmer, M.Buenerd, D.L.Hendrie, J.Mahoney, M.C.Mermaz and D.K.Scott, Phys.Report, 42(1978)311

(Gl 77) P.Glässel, R.S.Simon, R.M.Diamond, R.C.Jared, I.Y.Lee, L.G.Moretto,

J.O.Newton, R.Schmitt and F.S.Stephens, Phys.Rev.Lett., 38(1977)331

(Gr 70) G.F Gridnev, V.V.Volkov and J.Wilczynski, Nucl.Phys.A142(1970)385

(Gr 74) D.H.E.Gross and H.Kalinowski, Phys.Lett., 48B(1974)36

(Gr 78) D.H.E.Gross and H.Kalinowski, Phys.Rep., 45(1978)175

(He 72) H.H.Heckman, D.E.Greiner, P.J.Lindstrom and F.S.Bieser, Phys.Rev.Lett., 28(1972)926

(Ho 76) H.Hofmann and P.J.Siemens, Nucl.Phys.,A257(1976)130

(Ho 77) H.Hofmann and P.J.Siemens, Nucl.Phys.,A275(1977)464

(Hu 76) J.R.Huizenga, J.R.Birkelund, W.U.Schroeder, K.L.Wolf and V.E.Viola Jr., Phys.Rev.Lett., 37(1976)885

(Ic 83) S.Ichimura and M.Ichimura, private communication

(Is 76) M.Ishihara, T.Numao, T.Fukuda, K.Tanaka and T.Inamura, Proceedings of the Symposium on Macroscopic Feature of Heavy Ion Collisions, Argonne, Illinois 1976, Edited by D.G.Kovar, ANL Report No. ANL/PHY 76.2, p617

(Is 78) M.Ishihara, K.Tanaka, T.Kammuri, K.Matsuoka and M.Sano, Phys.Lett., 73B(1978)281

(Ka 61) R.Kaufmann and R.Wolfgang, Phys.Rev., 121(1961)192

(Ka 81) T.Kammuri and K.Matsuoka, Nucl.Phys., A366(1981)171

(Ko 50) J.Korringa, Physica, 16(1950)601

(Ko 76) C.M.Ko, H.J.Pirner and H.A.Weidenmuller, Phys.Lett.,62B(1976)248

(Le 78) Edited by C.M.Lederer and V.S.Shirley, Table of Isotopes, seventh edition, John Wiley & Sons, Inc.

(Le 83) H.Lenske, S.Landowne, H.H.Wolter, T.Tamura and T.Udagawa, Phys.Lett.,122B(1983)333

(Ma 68) J.B.Marion and F.C.Young, Nuclear Reaction Analysis, North-Holland

(Ma 82) K.Matsuoka and T.Kammuri, Nucl.Phys.,A376(1982)341

(Mi 71) T.Minamisono, K.Matuda, A.Mizobuchi and K.Sugimoto, J.Phys.Soc.Japan, 30(1971)311

(Mi 73) T.Minamisono, J.Phys.Soc.Japan, Suppl., 34(1973)324

(Mi 81) T.Minamisono, Y.Nojiri, K.H.Tanaka, Y.Miake, N.Takahashi and K.Sugimoto, Hyperfine Interactions, 9(1981)53

(Mi 83) Minamisono, K.H.Tanaka, Y.Nojiri, K.Asahi and N.Takahashi, Hyperfine Interactions, in press

(Mo 73) L.G.Moretto, D.Heunemann, R.C.Jared, R.C.Gatti and S.G.Thompson, Physics and chemistry of fission 1973 (Intern.Atomic Energy Agency, Vienna, 1974) Vol.2, p351.

(Mo 73) M.Morita, Beta Decay and Muon Capture, W.A.Benjamin,Inc.

(Mo 57) M.Morita and R.Saito.Morita, Phys.Rev.,107(1957)1316

(Ni 83) K.Niita and N.Takigawa, Nucl.Phys.,A397(1983)141

(No 70) L.C.Northcliffe and R.F.Schilling, Nucl.Data Table, A7(1970)233

(No 79) W.Nörenberg and C.Riedel, Z.Phys.,A290(1979)335

(No 79a) W.Nörenberg, Lecture Note in Physics, 117(1979)50

(Ng 75) C.Ngo, B.Tamain, M.Beiner, R.J.Lombard, D.Mas and H.H.Deubler, Nucl.Phys.,A252(1975)237

(Ol 68) J.W.Olness and E.K.Warburton, Phys.Rev., 166(1968)1004

(Os 76) R.Ost, N.E.Sanderson, S.Mordechai, J.B.A.England, B.R.Fulton, J.M.Nelson and G.C.Morrison, Nucl.Phys., A265(1976)142

(Re 82) R.Reif and G.Saupe, J.Phys., G8(1982)L21

(Sc 76) W.U.Schroeder, J.R.Birkelund, J.R.Huizenga, K.L.Wolf, J.P.Unik, and V.E.Viola Jr, Phys.Rev.Lett., 36(1976)514

(Sc 78) W.U.Schroeder, J.R.Birkelund, J.R.Huizenga, K.L.Wolf and V.E.Viola Jr., Phys.Rep., 45(1978)301

(Sb 78) T.Shibata, H.Ejiri, J.Chiba, S.Nagamiya, K.Nakai, R.Anholt,

H.Bowman, J.G.Inrerson, E.A.Rauscher and J.O.Rasmussen, Nucl.Phys., A308(1978)513

(Sc 81) R.Schmidt and R.Reif, J.Phys., G7(1981)775 and Preprint E4-81-26, JINR Dubna (1981)

(Si 76) K.Siwek-Wilczynska and J.Wilczynski, Nucl.Phys., A264(1976)115

(Si 78) K.Siwek-Wilczynska and J.Wilczynski, Phys.Lett.,74B(1978)313

(Su 68) K.Sugimoto, K.Nakai, K.Matuda and T.Minamisono, J.Phys.Soc.Japan, 25(1968)1258

(Su 77) K.Sugimoto, N.Takahashi, A.Mizobuchi, Y.Nojiri, T.Minamisono, M.Ishihara, K.Tanaka and H.Kamitsubo, Phys.Rev.Lett., 39(1977)329

(Ta 78) N.Takahashi, Y.Miake, Y.Nojiri, T.Minamisono, A.Mizobuchi, M.Ishihara and K.Sugimoto, Phys.Lett., 73B(1978)281

(Ta 78a) N.Takahashi, Y.Miake, K.H.Tanaka, Y.Nojiri, T.Minamisono and K.Sugimoto, Proc. 1978 INS Int. Symp. on Nucl. Direct Reaction Mechanism, (1978)635

(Ta 80) N.Takahashi, K.H.Tanaka, Y.Nojiri T.Minamisono and K.Sugimoto, Continuum spectra of heavy ion reactions, Harwood Acad.Pub., (1980)109

(Ta 81) N.Takahashi, K.H.Tanaka, Y.Nojiri, T.Minamisono and K.Sugimoto, Proc. Int. Symp. on Polarization Phenomena in Nuclear Physics, Santa Fe, 1980, AIP Conference Proceedings 69(1981)1114 and N.Takahashi, p1016 in the same proceedings.

(Ta 83) K.H.Tanaka, K.Asahi, Y.Nojiri, T.Minamisono and N.Takahashi, Proc. of 1983 Int. Symp. on Light Ion Reaction Mechanism, (1983)836

(Tk 81) N.Takigawa, K.Niita, Y.Okuhara and S.Yoshida, Nucl.Phys., A371(1981)130

(Tm 80) T.Tamura, Continuum spectra of heavy ion reactions, Harwood

Acad.Pub., (1980)155

(Tr 77) W.Trautmann, J.de Boer, W.Dünnweber, G.Graw, R.Kopp, C.Lauterbach, H.Puchta and U.Lynen, Phys.Rev.Lett., 39(1977)1062

(Tr 80) W.Trautmann, W.Dahme, W.Dünnweber, W.Hering, C.Lauterbach, H.Puchta, W.Kühn and J.P.Wurm, J.de Phys.Colloque, C10(1980)249

(Ud 78) T.Udagawa and T.Tamura, Phys.Rev.Lett., 41(1978)1770

(Va 79) R.Vandenbosch, Phys.Rev., 20C(1979)171

(Vo 78) V.V.Volkov, Phys.Rep., 44(1978)93

(We 68) J.C.Wells Jr, R.L.Williams Jr, L.Pfeiffer and L.Madansky, Phys.Lett., 27B(1968)448

(Wi 73) J.Wilczynski, Phys.Lett., 47B(1973)484

(Wi 82) J.Wilczynski, K.Siwek-Wilczynska, J.Van.Driel, S.Gonggrij, D.C.J.M.Hageman, R.V.F.Janssens, J.Lukasiak, R.H.Siemssen and S.Y.Van der Werf, Nucl.Phys., A373(1982)109

(Yo 75) M.Yoshie and I.Kohno, Scientific Papers of the IPCR, 69(1975)63